INSTITUTO
UNIVERSITÁRIO
DE LISBOA

Gaussian noise model for multiband optical networks over the C and L bands

Pedro Daniel Santo Venda

Master Degree in Telecommunications and Computer Engineering,

Supervisor:
PhD João Lopes Rebola, Associate Professor,
Iscte-IUL

Co-Supervisor:
PhD Luís Gonçalo Lecoq Vences e Costa Cancela, Assistant Professor,
Iscte-IUL

November, 2021

TECNOLOGIAS
E ARQUITETURA

Department of Information Science and Technology

Gaussian noise model for multiband optical networks over the C and L bands

Pedro Daniel Santo Venda

Master Degree in Telecommunications and Computer Engineering,

Supervisor:
PhD João Lopes Rebola, Associate Professor,
Iscte-IUL

Co-Supervisor:
PhD Luís Gonçalo Lecoq Vences e Costa Cancela, Assistant Professor,
Iscte-IUL

November, 2021

Acknowledgment

I want to thank to Iscte-IUL and my supervisors Professor João Rebola and Professor Luís Cancela for all their guidance and support during the course of this work. I would also like to acknowledge the Instituto de Telecomunicações, for providing me computer equipment to obtain many of the results present in this work.

Thank you to all my friends for their continuous encouragement and companionship during these years.

Last, but surely not least, I would like to express my deepest and most heartfelt gratitude to my family for their unconditional support and love.

Resumo

O modelo de ruído Gaussiano (GN-model, em inglês) foi desenvolvido para estimar a interferência não-linear (NLI, em inglês) e simplificar o projeto e análise dos sistemas com multiplexagem por divisão de comprimento de onda (WDM, em inglês) atuais. Recentemente, o modelo GN generalizado (GGN-model, em inglês) foi proposto para avaliar o desempenho em sistemas multibanda C+L, onde a interação entre difusão estimulada de Raman (SRS) e NLI deve ser corretamente caracterizada.

Nas redes óticas, os canais WDM são inseridos e extraídos, resultando numa variação dinâmica do tráfego ao longo das secções de fibra (referida aqui como utilização de rede) que influencia o impacto da SRS e NLI na relação sinal-ruído ótica (OSNR, em inglês). Neste trabalho, é realizado um estudo exaustivo do desempenho dos modelos GN e GGN considerando transmissão ponto-a-ponto e de rede em toda a banda C+L e diferentes utilizações de rede.

Para 0 dBm de potência por canal e variando a utilização de rede de 20% a 100%, a transferência de potência aumenta 5.3 dB devido à SRS. Na OSNR ótima, a transferência de potência máxima devido à SRS situa-se entre 4.4 dB e 6.4 dB e a variação máxima da OSNR ao longo da banda C+L é apenas 0.7 dB. Comparando as estimativas da OSNR dos modelos GGN e GN com formulação fechada (mais adequados para avaliar o desempenho em redes ópticas), demonstra-se que a diferença máxima entre os modelos é cerca de 0.7 dB na OSNR ótima e com ocupação total da banda C+L.

Palavras-chave: difusão estimulada de Raman, interferência não-linear, modelo de ruído Gaussiano, redes óticas, sinais multibanda.

Abstract

The Gaussian-noise (GN) model is an efficient tool to estimate the nonlinear interference (NLI), simplifying current wavelength-division multiplexing (WDM) systems design and analysis. Recently, the generalized Gaussian noise (GGN) model has been proposed for assessing the performance of multiband C+L transmission in WDM optical systems, where the interaction between NLI and stimulated Raman scattering (SRS) must be accurately characterized.

In a network scenario, the WDM channels are added and dropped, leading to dynamic traffic variations in the fiber spans (here referred as network utilization). For efficient network planning, the combined SRS and NLI impact on the optical signal-to-noise ratio (OSNR) must be properly evaluated for the whole C+L band and different network utilizations. In this work, an exhaustive study of the performance of the GN and GGN models for point-to-point and network transmission scenarios is performed.

For 0 dBm channel launch power and network utilizations from 20% to 100%, the power transfer between the outer channels increases about 5.3 dB due to SRS. At optimal OSNR, the maximum power transfer due to SRS lies between 4.4 dB and 6.4 dB and the maximum OSNR variation along the WDM channels bandwidth is only 0.7 dB. Comparing the OSNR predictions of GGN and GN models closed form approximations (which are more suitable for the performance assessment in network scenarios), it is demonstrated that the maximum difference between methods is below 0.7 dB at optimum OSNR and for maximum C+L band occupancy.

Keywords: Gaussian noise model, multiband transmission, nonlinear interference, optical networks, stimulated Raman scattering.

Contents

List of Figures

List of Tables

List of Acronyms

AGN	additive Gaussian noise
ASE	amplified spontaneous-emission
BER	bit error-rate
CUT	channel under test
CUTs	channels under test
DSP	digital signal processing
EDFA	erbium-doped fiber amplifier
EGN	enhanced Gaussian-noise
FWM	four-wave mixing
GGN	generalized Gaussian-noise
GN	Gaussian-noise
GNRF	GN-model reference formula
I	in-phase
IGN	incoherent Gaussian-noise
IGNRF	incoherent GN-model reference formula
ISRS	inter-channel stimulated Raman scattering
LWN	locally-white-noise
MCI	multi-channel interference
MSR	maximum system reach
NLI	non-linear interference
NZDSF	non-zero dispersion-shifted fiber
OSNR	optical signal-to-noise ratio

PDF	probability density function
PM	polarization-multiplexed
PSCF	pure silica-core fiber
PSD	power spectral density
Q	quadrature
QAM	quadrature amplitude modulation
QoT-E	quality of transmission estimator
QPSK	quadrature phase-shift keying
RC	raised cosine
ROADM	reconfigurable optical add/drop multiplexer
Rx	receiver
R&S	route and select
SCI	self-channel interference
SMF	single-mode fiber
SNR	signal-to-noise ratio
SPM	self phase modulation
SSFM	split-step Fourier method
SRS	stimulated Raman scattering
SRRC	square-root raised cosine
Tx	transmitter
UT	uncompensated transmission
WDM	wavelength-division multiplexing
XCI	cross-channel interference
XPM	cross-phase modulation
XPolM	cross-polarization modulation

List of Symbols

α	fiber loss coefficient
β	roll-off factor
β_2	group-velocity dispersion
β_3	group-velocity dispersion slope
γ	fiber Kerr nonlinearity coefficient
$\Delta\rho(L)$	power transfer between outer channels
$\Delta\rho(L)_{opt}$	power transfer between outer channels at optimum launch power
Δf	WDM channel spacing
ϵ	coherence factor
$\epsilon_{\text{network}}$	network utilization
$\epsilon_{\text{occupancy}}$	optical transmission bandwidth occupancy
$\epsilon_{req,j}$	required network utilization in the j-th span
$\epsilon_{\text{span},j}$	network utilization of j-th span
η_{NLI}^{link}	total normalized NLI power of a link
η_{NLI}	normalized NLI power
$\eta_{\text{SCI},j}$	SCI normalized NLI power of the j-th span
$\eta_{\text{XCI},j}$	XCI normalized NLI power of the j-th span
λ	operating wavelength
ν_c	nominal optical frequency of the center channel
ρ	normalized FWM efficiency
$\rho(z, f)$	signal power profile
$\sigma_{\eta_{\text{NLI}}}$	standard deviation of η_{NLI}
χ	phased array factor
A_{eff}	fiber effective area
B_m	bandwidth of the m-th WDM channel
$B_{\text{C-band}}$	C-band optical transmission bandwidth
$B_{\text{C+L-band}}$	C+L band optical transmission bandwidth
B_{WDM}	overall WDM signal bandwidth
c	speed of light
C_r	Raman gain slope
D	dispersion parameter
f	low-pass equivalent frequency
f_m	center frequency of the m-th WDM channel

f_n	noise figure
g_i	gain of the i-th optical amplifier
$G_{x,y}(f_m)$	Rectangular WDM channel PSD for one polarization
$G_{\text{NLI}}(f)$	NLI PSD at the end of a link
$G_{\text{NLI}}^{1span}(f_m)$	NLI PSD per polarization for channel m and one fiber span
$G_{\text{SCI}}^{1span}(f_m)$	SCI PSD per polarization for channel m and one fiber span
G_{SRS}	SRS gain
G_{WDM}	PSD of the WDM signal for two polarizations
$G_{\text{XCI}}^{1span}(f_m)$	XCI PSD per polarization for channel m and one fiber span
h	Planck constant
$H_{\text{RC}}(f)$	transfer function of the RC filter
$H_{\text{Rx}}(f)$	overall baseband transfer function of the receiver
$H_{\text{Tx}}(f)$	transmitter transfer function
j	imaginary unit
k_0	light wavenumber
L_{eff}	effective span length
$L_{\text{eff,a}}$	asymptotic effective length
$\text{Li}_2(f)$	dilog function
L_s	span length
M	digital modulation order
$\overline{n}_2$	nonlinear fiber index
$N_{\text{add/drop}}$	number of add/drop channels
N_{amp}	total number of optical amplifiers
N_{ch}	number of WDM channels
$N_{ch,j}$	number of WDM channels transmitted in the j-th span
N_{CUT}	number of channels under test
n_{freq}	array position of each frequency component of the integration domain
N_s	total number of spans in a link
OSNR_{opt}	OSNR at optimum launch power
$P(f)$	input pulse spectrum
$P_{\text{ASE},i}$	ASE noise power of the i-th optical amplifier
$P_{\text{ASE},tot}$	total ASE noise power in a lightpath
P_{CUT}	reference power of the CUT
P_m	power per channel for two polarizations
$P_{m,1}$	power of the m-th channel launched in the first span of a link
$P_{m,j}$	power of the m-th channel launched in the j-th span of a link
P_m^x	power per channel for polarization direction **x**

P_m^y	power per channel for polarization direction **y**
P_{NLI}	NLI noise power
$P_{\text{NLI},tot}$	total NLI noise power in a lightpath
P_{tot}	total optical launch power of the WDM signal
Q_1	integrand function of the first quadrant of the integration domain of the GGN-model in hyperbolic coordinates
Q_2	integrand function of the second quadrant of the integration domain of the GGN-model in hyperbolic coordinates
Q_3	integrand function of the third quadrant of the integration domain of the GGN-model in hyperbolic coordinates
Q_4	integrand function of the fourth quadrant of the integration domain of the GGN-model in hyperbolic coordinates
$R_{s,m}$	symbol rate of the m-th WDM channel
S_r	dispersion slope
T_s	symbol period
z	longitudinal spatial coordinate along the link

CHAPTER 1

Introduction

1.1. Motivation

The combination of digital signal processing (DSP), coherent detection and spectrally efficient modulation formats enabled the delivery of high bit-rate applications in optical transmission systems and has enjoyed widespread adoption over the last ten years [1].

Nowadays, metropolitan and core networks largely use digital coherent transponders and although some short-reach (around 100 km) data-center interconnect systems still consider solutions based on direct detection [2], [3], they are likely, in the future, to eventually deploy digital coherent technology as well [4]. The coherent receivers enable efficient polarization demultiplexing, higher-order modulation formats, increased sensitivity and the minimization of optical impairments, such as polarization mode dispersion (PMD) or chromatic dispersion effects [1], [5]. Furthermore, it allows removing optical dispersion compensation from the transmission link and thus achieve better performance than in the case of optically compensated transmission [6]. However, despite dispersion and PMD, which are linear transmission impairments, can be dealt with electronically, the nonlinear effects due to the Kerr non-linearity in the fiber remain a significant source of performance degradation [7].

In order to study the performance degradation due to these nonlinear impairments and design the optical coherent systems in presence of those effects, several approximated models to characterize the nonlinear signal propagation along the fiber have been proposed over the years. These models describe the interplay between the dispersion and the nonlinear Kerr related effects simply as Gaussian noise, named as nonlinear interference (NLI), and provide a reasonably accurate description of the optical network performance (see for example, [8]–[11]). This had a major impact on assessing network and system performances, since it is no longer necessary to resort to complex and computationally intensive split-step Fourier method (SSFM) simulations to estimate such performance [4].

The global traffic growth is about 45% per year [4]. In order to address such growth of data traffic in optical networks, several alternative solutions to C-band only transmission systems have been proposed, one of them being multiband transmission in the C+L band [4], [12]. Typically, optical networks work only in the C-band (1530 nm-1565 nm), with about 4.4 THz

bandwidth [4]. The multiband C+L transmission solution exploits the linear gain in capacity that can be obtained by scaling the bandwidth used for transmission to the L-band (1565nm - 1625 nm) [13]. However, in transmission systems beyond the C-band, the nonlinear Kerr effects are not the only relevant propagation impairment. The stimulated Raman scattering (SRS) must also be taken into account in multiband systems. Consequently, new models to evaluate the system performance in the C+L band have been proposed to take into account the interaction between NLI and SRS [14]–[16].

In this work, the following nonlinear models will be studied and implemented:

- Gaussian-noise model (GN-model) [7], [17];
- GN-model variant proposed in [10] (designated in this work as asymptotic GN-model);
- Generalized GN-model (GGN-model) or also called inter-channel SRS (ISRS) GN-model solved by numerical integration or using closed-form formulas [15], [16].

The main goal of this work is to assess the impact of the interaction of SRS and NLI on the performance of C+L multiband signal transmission in point-to-point links and network scenarios and evaluate the validation range and limitations of the GN, asymptotic GN and GGN models.

1.2. Objectives

The main objectives of this dissertation are:

- Study of the GN-model to estimate the NLI and its impact in coherent detection fiber transmission systems working only in the C-band;
- Software implementation of the GN-model in Matlab;
- Study of the interaction of SRS and NLI in multiband transmission systems;
- Software implementation of the GGN-model in Matlab;
- Assessment of the impact of the interaction of SRS and NLI on the performance of C+L multiband signal transmission in a network scenario and of the validation range and limitations of the asymptotic approach, GN-model and GGN-model.

1.3. Organization

This dissertation is organized as follows.

Chapter 2 introduces the theoretical concepts related with the non-linearity in transmission systems without optical dispersion compensation and with the GN-model and its variants. The GN-model and its evolution over the years are presented and their assumptions and limitations are explained.

Chapter 3 is focused on the study of the GN models suitable only for the C-band. The equations of the GN and asymptotic models are presented and their physical meaning is explained. Furthermore, the impact of varying several system parameters on the NLI estimation is quantified and the performance of the GN models is evaluated up to the C-band limit.

Chapter 4 is dedicated to the study of the GGN-model. The SRS effect is explained in the context of C+L band transmission systems and the correct implementation of the GGN-model is confirmed in a point-to-point transmission scenario using an analytical formula and a closed-form formula. The simulation of an optical network based on a real topology is performed and the consequences of varying several network parameters on the NLI and optical signal-to-noise ratio (OSNR) estimation are investigated. Lastly, the OSNR estimates of the asymptotic GN-model and closed-form GGN-model are compared in a C+L network scenario.

Finally, in chapter 5, the main conclusions of this work are presented and some suggestions for future work are provided.

1.4. Main contributions

This dissertation has the following main contributions:

- In-depth studies of the relation between the number of wavelength-division multiplexing (WDM) frequency components, the accuracy of the GN-model numerical integration and the corresponding computation time;
- Assessment of the maximum difference in the OSNR estimation between the GN and asymptotic models for a point-to-point transmission scenario up to the C-band limit and for different channel roll-offs;
- Derivation and presentation of a GGN-model formula in hyperbolic coordinates (original contribution);
- Exhaustive study of the GGN-model in a network scenario, by varying several WDM system parameters such as network utilization, number of channels under test, launch power and C+L band occupancy (original contribution);
- Assessment of the maximum difference in the OSNR estimation between the asymptotic GN-model and the GGN-model in a network transmission scenario up to the C+L band limit and for different network utilizations (original contribution).

CHAPTER 2

Literature review

2.1. Introduction

The exponential growth in the demand for data traffic and its delivery through information and communication technologies implies constant research and innovation in the area of optical transmission [4]. One of the most remarkable technological progresses was the arrival of the optical coherent detection systems supported by DSP [1]. This technology enabled electronic chromatic dispersion compensation at the digital signal processors [18] and led to optical transport links where optical dispersion compensation does not exist, called uncompensated transmission (UT) links [11], [17]. This shift to UT links brought several advantages concerning the modeling and assessment of the performance of these systems. In particular, it is possible to estimate system performance using relatively simple nonlinear propagation models. One of the most adopted models is the GN-model [11], [17].

The GN-model describes the fiber nonlinear effects due to the Kerr non-linearity as NLI in optical UT systems. In particular, it is possible to quantify the NLI impact and, hence, evaluate and improve the system performance for different network scenarios, simplifying the design and management of optical telecommunications systems and allowing simple and effective physical layer aware network optimization [11], [17].

Among the many models proposed in the literature to estimate NLI, the GN-model is the most adopted [11], [17]. The main reason for GN-model widespread adoption is because it guarantees the right balance between the two fundamental key requirements that make every model effective: acceptable computational complexity and sufficient NLI estimation accuracy [11]. Over the last years, the GN-model has been updated and improved to cover different NLI modeling requirements. In these different modeling solutions, there are trade-offs between NLI estimation accuracy, ease of use and computational complexity [11]. For example, if very accurate research-oriented investigations need to be carried out, then a more powerful GN-model must be adopted and, thus, high accuracy in NLI estimation can be achieved (see for example [9], [11]). However, the adoption of more sophisticated models typically implies greater computational complexity and cannot always fulfill the needs of the system and network designers.

For instance, if real-time physical layer awareness and preliminary performance assessment are the main priority, simpler models are the most indicated [11].

One of the focus areas of scientific research at the moment is on technologies that enable the increase of core network capacity [12], [13]. One of the proposed solutions consists of the enlargement of the optical transmission bandwidth beyond the C-band, using C+L bandwidth transmission systems. In multiband transmission systems (C and L bands), the inter-channel crosstalk due to SRS must be taken into account [14], [15], [19], [20]. Therefore, despite the GN-model being a widely adopted tool by the network and system designers, it is only valid for C-band transmission, since the SRS is not significant in this band and is not included in the earlier GN-model formulations [7], [15]. Due to this limitation, a new model, that includes the SRS effect on C+L band transmission systems, has been developed, which is designated in this work as GGN-model [15], [16], [19].

This work starts with the study of the model designated as asymptotic GN-model [10], followed by more complex models like the GN-model [8], [11] and GGN-model [15], [16]. The definition, assumptions and limitations of these models will be summarized in sections 2.2 and 2.3.

2.2. GN-model

The GN-model is a first-order regular-perturbation model based on the *Schrödinger* and *Manakov* equations [7], [21]. This model allows calculating the power spectral density (PSD) of the NLI based on several assumptions [7], [8], [17].

2.2.1. Modeling assumptions

The main GN-model assumption is that NLI can be treated as Gaussian noise after fiber propagation and after DSP [7], [8], [11], [17]. This major assumption can be explained based on UT signal propagation properties [7].

As already mentioned in section 2.1, along fiber propagation on UT links, fiber dispersion is not optically compensated and accumulates along the link. After sufficiently long distances, due to the large values of accumulated dispersion, the statistical distribution of the four signal electric field components (the quadrature Q and in-phase I components for each polarization direction, X or Y) of each transmitted WDM channel is found to be very close to a zero-mean Gaussian distribution, irrespective of the sampling instant (statistically independent) and with no correlation between signal components [7], [22]. This is called the Gaussianity assumption

[7], [11], [17] and it was extensively confirmed for PM-QPSK signals at the fiber output (before DSP) both in linear and nonlinear regimes [22].

In figure 2.1, it can be observed the histogram of the signal distribution of the four components of a PM-QPSK format after 500 km of WDM signal propagation in the nonlinear regime [22]. The Gaussianity assumption is proven by comparing the histograms with the Gaussian PDF (red lines) and has been further demonstrated for higher modulation formats in [7].

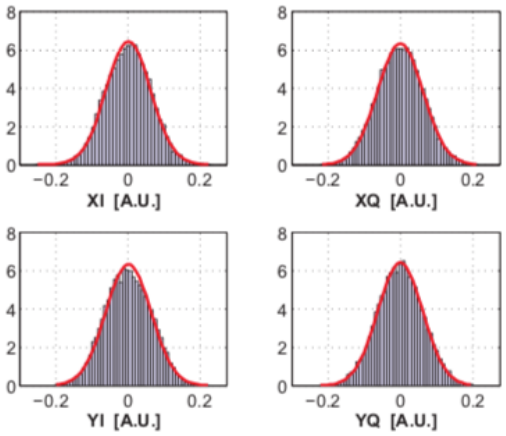

Figure 2.1. Histogram of the four signal components at the Rx input superimposed over a zero-mean Gaussian distribution with the same variance displayed in red. After 500 km of propagation in nonlinear WDM regime with a transmitted power of 0 dBm (taken from [22]).

The Gaussianity assumption, shown in figure 2.1, can be explained based on the argument that, at any point in time, the resulting field is a linear combination of statistically independent contributions coming from many different random data symbols. The sum of these random contributions makes the signal distribution Gaussian [7]. On the other hand, by performing a more rigorous analysis, it has been pointed out that the components of the signal samples are not statistically independent and the signal cannot be considered entirely as a Gaussian process, due to the absence of a Gaussian distribution between all field samples [23]. The GN-model neglects these factors and assumes that the signal statistically behaves as a stationary Gaussian noise [17]. In doing so, the model is simplified, since the PSD of the NLI is sufficient to characterize its effect on UT links [21].

The Gaussianity assumption has some disadvantages, leading to NLI overestimation in the first spans of transmission [11], [17]. Although the NLI power estimation error reduces along the link, it is still relevant at longer reaches, where a 1 to 2 dB NLI noise power overestimation is verified for typical systems [24]. Consequently, the NLI overestimation yields underestimated performance estimates. In [17], for PM-QPSK signals transmission over single-mode

fiber (SMF), the SSFM simulations revealed about 6 dB less NLI noise power over the first span than the GN-model estimates, and for PM-16QAM signals, the difference found was approximately 3.5 dB. The difference between the GN-model and simulation results happens because, in the first spans, the signal is not yet sufficiently dispersed, and therefore it does not achieves a Gaussian distribution [11], [17]. The discrepancy between results decreases with the increase of the number of spans. Interestingly, when pre-dispersed signals (application of dispersion to the signal before launching it into the fiber, 100 000 ps/nm) are considered, the GN-model and simulation results demonstrated an excellent agreement [17]. This is the main reason for the GN-model early versions (see for example [25], [26]) inefficiency with the dispersion-managed systems, which have optical dispersion compensation. The high signal dispersion is a prerequisite for the accuracy of the GN-model, hence its widespread adoption in UT systems with coherent detection [11].

The high dispersion requirement is not sufficient to ensure the signal Gaussianity approximation. The level of signal dispersion reached during propagation is directly related to the signal symbol rate, once signals with a lower symbol rate must propagate along much more spans than high symbol rate signals to achieve a similar accumulated dispersion that leads to the signal Gaussian constellation. Therefore, it can be stated that one of the GN-model weaknesses is also its poor performance at low symbol rates [8], [11].

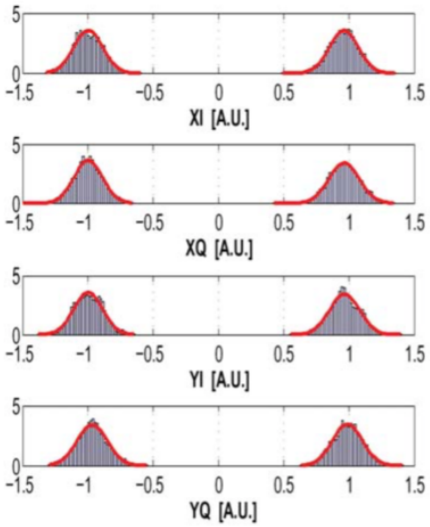

(a) Histogram of the four signal components at the Rx output. Signal propagation along 1000 km in nonlinear WDM regime.

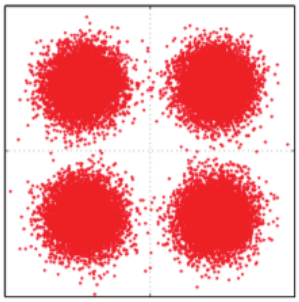

(b) Scattering diagram at the Rx output for one polarization and 3000 km of WDM transmission.

Figure 2.2. Diagrams obtained for PM-QPSK transmission at the Rx output after DSP (taken from [22]).

At the receiver (Rx) output, after chromatic dispersion has been compensated by DSP, the statistical distribution of the signal was found to be Gaussian as well, and once again, there was no correlation between the signal electric field components [22]. Furthermore, it was also shown that the variance of the Gaussian noise depends on the transmitted signal power and link distance, being the Gaussian noise variance higher as transmitted power increases [22]. In figure 2.2 a), the histogram of the four signal components at Rx output after DSP is displayed. In figure 2.2 b), the scattering diagram of each of the received constellation points for one polarization direction is depicted.

It is important to remark that the results shown in figure 2.2 a) and b) are proven independently of the amplified spontaneous-emission noise (ASE) presence in the link. Therefore, it can be stated that the Gaussian noise after DSP (where dispersion effect has been compensated from the signal) is induced by non-linearity alone [22], which permits to conclude that the effect of the NLI can be modeled as additive Gaussian noise (AGN) [7], [8]. Due to their independence, ASE noise and NLI can simply be summed in power and NLI impact on system performance can be assessed through a modified signal-to-noise-ratio [17], [27], [28]. This is designated as the AGN assumption [17] and only is valid at least for low-to-moderate non-linearity [7]. Furthermore, by optimizing the modified OSNR, it was demonstrated that the maximum reachable distance in nonlinear propagation is equivalent to two-thirds of the distance the system could reach in linear regime at the optimum launch power [27]. Additionally, it has also been shown that, under the optimum transmission regime, the NLI noise power is half of the ASE noise power [27]. Thus, it can be argued that NLI is not too large in typical optical communication transmission systems, and thereby, the AGN assumption is valid [7].

Hence, based on the low-to-moderate non-linearity assumption, the GN-model was derived using *perturbative* techniques [7], [8], [17]. The most known techniques are the four-wave mixing (FWM) and Volterra Series (VS) approaches. Using truncated VS, the VS technique involves finding an approximated solution to the nonlinear Schrödinger equation. The FWM approach consists of splitting the spectrum of the WDM signal into several components, with the nonlinear interaction between these components being formulated similarly to the FWM formulas developed for fiber signal propagation [8]. A perturbation technique belonging to these FWM *perturbative* approaches was exploited to obtain approximate analytical solutions of the nonlinear equations of Schrödinger and Manakov [7], that led to the derivation of the GN-model, introduced for the first time in [7]. When non-linearity levels are high, the perturbation assumption cannot be applied [17].

2.2.2. NLI contributions

For systems with sufficiently large accumulated dispersion and mild non-linearity, the joint effect of chromatic dispersion and NLI is similar to that of an additive Gaussian noise. For that reason, it is relevant to clarify the NLI contributions that add Gaussian noise to the signal. According to [8], the traditional taxonomy of fiber nonlinear effects in dispersion-managed systems, such as self-phase modulation (SPM), cross-phase modulation (XPM) and cross-polarization modulation (XPo1M), have each a very specific way of impacting the signal. Thus, they are incompatible with the NLI contributions in UT systems, since these have mainly only a qualitative effect: adding Gaussian noise to the signal.

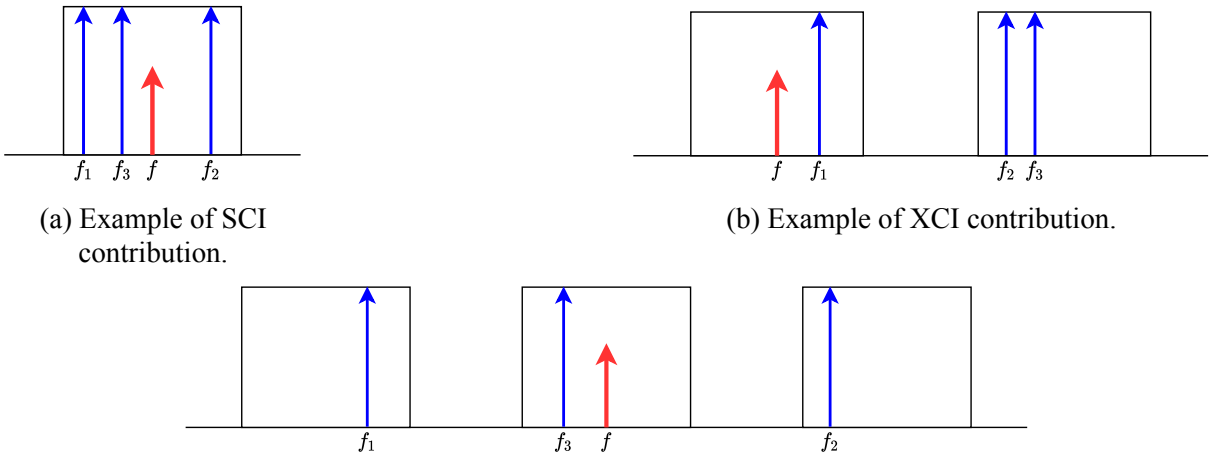

(a) Example of SCI contribution.

(b) Example of XCI contribution.

(c) Example of MCI contribution.

Figure 2.3. Classification of NLI contributions. The blue arrows are the generating frequency components and the red arrows are the generated NLI contributions [8].

The new taxonomy proposed for describing the fiber nonlinear effects in UT systems consists of three categories [8], [17]:

- Self-channel interference (SCI): the NLI perturbing a given channel, produced by that channel onto itself;
- Cross-channel interference (XCI): the NLI perturbing a given channel, generated by the nonlinear interaction of that channel with one other channel;
- Multiple-channel interference (MCI): the NLI perturbing a given channel, created by the nonlinear interaction of that channel with two other channels or by three channels other than the affected one.

After GN-model derivation, the nonlinear process can be seen as an FWM process [11]. In other words, the nonlinear interference created at a certain frequency "f" is a product of the

interaction of three frequencies (f_1, f_2, and f_3) [8], [11], [17]. The FWM process that generates NLI at frequency f is represented by the three NLI contributions: SCI, XCI, and MCI [8]. In figure 2.3 a), it is shown three signal frequency components of the same channel (f_1, f_2 and f_3) contributing to create NLI at frequency f in that same channel [8]. In figures 2.3 b) and 2.3 c), it is displayed the generation of NLI at frequency f of a given channel, generated by the nonlinear interaction of frequency components of that channel with frequency components of another channel (or other if it is MCI) [8].

As already mentioned, these three types of UT non-linearity have the same qualitative effect, which is adding Gaussian noise to the signal. On the other hand, they have different quantitative impacts on system performance. The SCI and XCI have relevant contributions to the NLI and depend on system parameters such as the number of channels, dispersion and the overall system optical bandwidth, while MCI contributions are practically negligible [8]. A more detailed explanation of the concepts of non-linearity in UT systems can be found in [8].

2.2.3. Incoherent GN-model

All NLI contributions along an optical link composed by several fiber spans add up until the receiver. This NLI sum along the signal propagation in several fiber spans can be dealt with in two ways: coherently or incoherently [8], [11], [17].

The first proposed GN-model uses the coherent solution. Specifically, it accounts for the coherent interference that occurs at the Rx input among the NLI contributions generated in each single span [17]. The other solution is considering that NLI accumulates incoherently along the fiber spans. In this way, a lower model complexity is achieved, once it is assumed that the accumulated NLI that arrives at the Rx input is just the sum of all independent NLI contributions generated in each fiber span. This alternative is known as the incoherent GN-model (IGN) [11], [17].

Interestingly, the IGN-model ensures a better NLI estimation, being typically closer to SSFM simulation results than the GN-model, especially on the maximum reach estimates [11], [17]. It was shown that the NLI power from XCI contribution asymptotically accumulates incoherently along the number of spans and, for that reason, the IGN-model provides better performance than the coherent GN-model [11]. It is important to refer that XCI tends to dominate over SCI as the number of channels increases, hence its greater impact on the NLI accumulation [11]. Additionally, it has also been shown that NLI accumulates almost incoherently for WDM signal bandwidths larger than 1 THz [8].

2.2.4. Main limitations

In [17], it was concluded that both *perturbative* and AGN assumptions are not very problematic, once it was noted that they did not create major inaccuracies on NLI estimation within the range of optimal system launch powers. Most of the accuracy limitations of GN-model arise from the signal Gaussianity assumption. To minimize this assumption impact on model accuracy, it is critical to know the system parameters for which GN-model can be applied. The GN-model produces reliable estimates for symbol rates higher than 25 GBaud, for channel spacings up to 100 GHz, for transmission systems that have at least 3 channels and over fibers with a dispersion parameter higher than 3.8 ps/nm/km and link distances equal or greater than 500 km (total accumulated dispersion of 1900 ps/nm) [8], [11]. Furthermore, the GN-model does not take into account the dependence of non-linearity generation on modulation format, long-correlated nonlinear phase and polarization noise [11]. To address some of these limitations, more complex models have been proposed, as for example, the EGN-model [9], [11], [23].

Despite the problems referred to in the last paragraph, the GN-model error on the estimation of key system performance indicators, such as maximum reach or optimum launch power, is small for realistic optical systems [11], [17], [24]. The error resulting from NLI overestimation is typically in the range of 0.2 to 0.6 dB on maximum system reach estimation, depending on fiber type and system setup [24]. Even so, the GN-model leads to pessimistic performance estimates and it does not account for all the requirements of system designers. In addition, this model is only valid for C-band transmission systems [14], [15], [19], [20]. In the following section, variants of the GN-model will be presented in more detail.

2.3. GN-model evolution

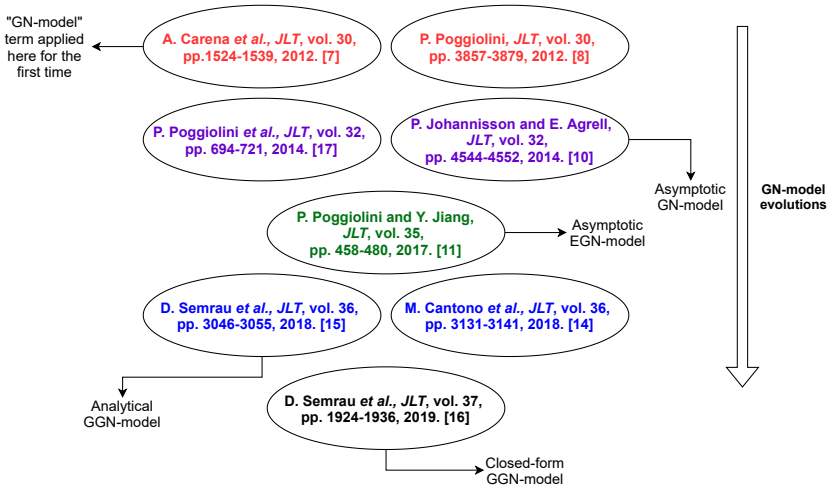

Figure 2.4. Some of the main works related to the GN-model, from the oldest at the top to most recent at the bottom.

In this section, the GN-model versions proposed over the years are presented, explained and their advantages and limitations are described. In figure 2.4, a diagram of some of the documents related to the GN-model is presented.

2.3.1. Asymptotic GN-model

The GN-model is a sufficient reliable tool to effectively estimate the non-linearity impact due to Kerr effect in an optical communication system ([7] and [17] in figure 2.4). On the other hand, for applications whose fundamental criteria are simplicity and ease of use, the GN-model may not be the most indicated. The model designated in this work as "asymptotic GN-model" has been proposed in [10] (see figure 2.4). Starting on the GN-model, the aim was to provide a fast and reliable non-linearity model applicable to optical networks for both real-time optimization (where traffic demands are added dynamically) and offline mode [10]. To obtain a simplified model, several assumptions and approximations have been made.

In a network, the NLI accumulation is not fully coherent or fully incoherent [10]. However, such as in the IGN-model, it is assumed that NLI accumulates incoherently [10]. Consequently, to obtain the total amount of NLI generated in the link, it is only needed to sum the NLI contributions produced in each fiber span separately along the entire optical path [10]. Another assumption is related to the PSD of each WDM channel, which is one of the parameters required to calculate the NLI PSD. In the asymptotic GN-model, a rectangular spectrum for each WDM channel is assumed. In this way, less complexity is ensured, once there is no need to simulate the WDM transmitted signal. This shape leads to improved spectral efficiency and also creates minimal inter-channel crosstalk; however, it is important to mention that is an unrealistic approximation [10]. Also in [10], the separation of SCI and XCI in the NLI equation formulation is considered. Thus, it is possible to obtain the total NLI PSD by summing these two contributions. Furthermore, due to the difficulty of accounting for the variation of NLI within a channel, it is assumed that the NLI variance can be based on the NLI PSD value at the center frequency of each channel. This approximation typically leads to NLI power overestimation [10].

This model relies on the GN-model and therefore inherit its assumptions and limitations. Moreover, it is only accurate for a fiber loss above 7 dB (more or less 35 km considering an attenuation coefficient of 0.2 dB/km). The most relevant assumption made to make the model formula simpler and intuitive is the application of the asymptotic expansion of the dilog function. This approximation is not accurate for channels with a bandwidth below 28 GHz [10]. However, when it was considered the asymptotic expansion model formula and the equation proposed in [10] without this approximation, it was shown that the asymptotic alternative provides better

performance (within the bandwidth limitation). Although both versions overestimate the NLI, the model resulting from the asymptotic approximation formula was consistently closer to numerical integration results [10].

Despite the referred limitations, this model constitutes an alternative simpler choice for a network optimization scenario, combining low complexity and reasonable accuracy [10].

2.3.2. Asymptotic EGN-model

As previously stated, most of GN-model limitations rely on the Gaussianity assumption. The EGN-model aim is to eliminate these restrictions by removing this assumption from the GN-model formulation. This is achieved by considering a correction term that typically decreases the PSD of the NLI estimated by the GN-model [11].

The NLI PSD estimation obtained using the EGN-model is excellent, being very similar to simulation results, even when it was considered low symbol rates (lower than 25 GBaud) [11]. On the other hand, the general EGN-model formula is rather complex [9] and this high accuracy in NLI estimation is paid in terms of computational complexity. In [11], it was proposed a simple closed-formula based on an asymptotic approximation to the correction term. Despite this approximation slightly overestimates the NLI power in the first spans (approximately up to five spans), the overall estimation results demonstrated a very good agreement with the simulation results, leading to an accuracy improvement compared to GN-model [11]. When symbol rates lower than 32 GBaud are considered, it was found that the asymptotic EGN approximation loses accuracy gradually; however, it still provides better NLI power estimation than the GN-model and can be considered sufficient accurate down to 5 GBaud [11].

In summary, the asymptotic EGN-model greatly reduces the EGN-model complexity and it also takes into consideration the modulation format [11]. Therefore, it is a very noteworthy alternative to GN-model for assessing system and network performance. However, despite the remarkable results accomplished by the EGN-model and its asymptotic approximation, the EGN-model by itself and simpler GN models are not appropriate for modeling NLI in multiband systems [15].

2.3.3. SRS definition and generalized GN-Model

The GN models described in the previous sections assume that every signal frequency component experiences the same power evolution during fiber propagation. Although this assumption is valid when transmitting in the C-band, in C+L band transmission systems and beyond,

the WDM signal frequency components undergo a different power evolution along fiber propagation [15]. This happens due to a frequency-dependent attenuation coefficient and to the presence of inter-channel crosstalk due to the SRS effect, which is negligible in the C-band, but must be taken into consideration in multiband systems [14], [15], [19].

The inter-channel crosstalk due to SRS is a nonlinear process that consists of amplifying low frequency components at the expense of high frequency components depletion within the same WDM signal [15]. In other words, this effect leads to a power transfer from higher to lower frequency components, which may create inaccurate performance estimations when using the GN models described in previous sections [14]. Therefore, it was necessary to include both the SRS effect and NLI generation in the GN-model formulation, leading to the creation of the GGN-model [14], [15].

The power transfer between different signal frequency components that occurs during propagation in the fiber can be described by a set of coupled differential equations (see for example, [29] or [30]). These equations must be solved numerically to obtain the signal power profile, which describes the gain or loss that each frequency component experiences during fiber transmission due to the SRS effect [14], [15]. Consequently, the signal power profile allows to obtain a semi-analytical GGN-model that takes into account the SRS effect and the frequency dependent fiber attenuation [14], [15]. However, a simpler and analytical GGN-model has been proposed in [15]. This is achieved considering negligible variation in fiber attenuation coefficient across the C+L band and thus assuming that the main contribution that causes the power transfer is the SRS effect. Additionally, it has been also assumed that the Raman gain spectrum is linear up to approximately 15 THz, which permits to obtain the signal power profile analytically, instead of numerically [16], [31]. Figure 2.5 illustrates a linear (or also called triangular) approximation of the Raman gain spectrum to around 15 THz.

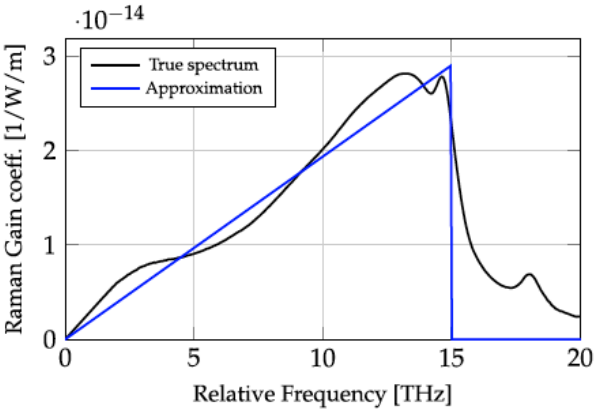

Figure 2.5. Linear approximation of the Raman gain spectrum (taken from [32]).

In [15], the accuracy of the analytical GGN-model was measured and the results were notable, obtaining a estimation of the NLI power with a maximum deviation of 0.1 dB when comparing to SSFM simulations. Furthermore, for the studied C+L band system, it was concluded that SRS modifies the NLI power by up to 2 dB after ten spans between the higher and lower frequencies of the WDM signal [15]. Besides that, it has also been proved that the impact of SRS on the NLI coefficient is higher for an increasing number of spans [15]. The analytical GGN-model is only valid where the Raman gain spectrum is assumed to be linear, that is, for bandwidths up to approximately 15 THz. To address this limitation, the semi-analytical GGN-model must be used [15], [16].

Additionally, the GGN-model was validated experimentally as an estimator to assess transmission quality (QoT-E), using the SNR as a performance metric. This was accomplished by comparing model estimates to measurements based on a system with commercial equipment (100 Gbit/s transponders on the testbed at the Orange laboratories). The results were noteworthy, proving a QoT-E reliability with a mere deviation of 0.5 dB when comparing to measurements results [14]. The GGN-model has also been successfully validated through experimental results in [33].

Although the remarkable results reached by the GGN-model, it is relevant to mention that this model is based on the GN-model and hence inherits its assumptions and limitations. For example, in order to perform the GGN-model numerical validation, the transmitted signals were drawn from a Gaussian distribution to emulate the signal Gaussianity assumption of the GN-model [15]. In [14], a constant 0.2 dB difference was obtained between the SNR results and simulation results due to the Gaussianity assumption. Nevertheless, it is clear that the GGN-model constitutes a powerful NLI estimation tool that operates over the entire C+L band [14], [15].

In this work, it will be considered the analytical GGN-model introduced in [15] for estimating the NLI PSD in point-to-point transmission systems. The reason behind this is because the analytical GGN-model is simpler and, according to [15], provides better results than some different GGN-models proposed in the literature (like, for example, the GGN-model presented in [19]).

2.3.4. Closed-form generalized GN-model

The satisfactory accuracy reached by the GGN-model requires solving a triple numerical integration, which increases substantially the overall computation time considering multiband transmission systems. For some applications (e.g., optical networks), it should be possible to estimate

the system performance in just microseconds [16]. For optical network analysis, the closed-form approximations represent a very useful tool, since they enable physical layer aware optimization and preliminary performance assessment within these time frames. For C-band transmission, various closed-form approximations of the GN-model have been proposed over the years [8], [10], [11], [24], [34], [35]. Recently, closed-form approximations have been derived for transmission systems operating beyond the C-band [16], [31], [36]. The GGN-model closed formula was introduced in [16], being valid for both point-to-point and network transmission scenarios. A GGN-model suitable for network analysis has already been proposed in [37]. However, this formula is even more complex than the GGN-model expression in its integral form indicated for point-to-point transmission, which makes it impractical for fast network performance estimations.

In order to derive the closed-form GGN-model, several approximations have been made. As in the asymptotic GN-model, the MCI contribution is neglected in this GGN-model approximation and only the XCI and SCI contributions are considered [16]. It is assumed that the XCI and SCI contributions accumulate incoherently and coherently, respectively [16]. The coherent accumulation of the SCI contribution is achieved using the coherence factor, which is redefined over the channel bandwidth rather than for the entire WDM signal. Furthermore, it is assumed that the SRS does not modify the coherence factor, which is not entirely accurate [16].

Besides those approximations, there are three more assumptions that are fundamental to simplify the derivation of the GGN-model closed formula. The first is that the channel spacing between the interference channel and the channel under test is much larger than half of the interference channel bandwidth for XCI contribution. The second assumption is known as weak SRS assumption, since it is assumed that SRS has a small impact on the signal power profile, and therefore, this profile can be approximated using a Taylor series of first order. The inaccuracy resulting from this approximation can be neglected when the intensity of SRS is considered small (see equation (13) of [16]). Lastly, the third key assumption is that the signal power profile does not depend on the signal launch power distribution. When the same power is considered for all WDM channels, this assumption has no effect on the model accuracy. For mesh optical networks with variably loaded spans, i.e., when WDM channels can be added or dropped in each node of the network, the effect of the third assumption seems to be negligible [16]. A more detailed explanation of the GGN-model closed form assumptions and derivation can be found in [16].

The closed-form GGN-model accuracy is slightly reduced due to these approximations performed in the derivation process. However, as for the others GN models, the most significant

loss of accuracy results from the Gaussianity assumption. For six SMF spans, 64-QAM modulation and transmission scenarios with and without SRS, the average difference between the estimates of the coherent closed-form GGN-model and the SSFM is about 1.6 dB [16]. In a mesh optical network scenario, this difference decreases to 1 dB, since the average accumulated dispersion becomes higher due to added and dropped channels, which can have different launch powers [16].

2.4. Conclusion

In this chapter, the original GN-model and its variants have been described and its advantages and limitations have been discussed. Table 2.1 presents a summary of the minimum system parameters (symbol rate and dispersion) and transmission bandwidth for which each GN-model is reliable.

GN models	**Symbol rate**	**Total dispersion**	**Bandwidth**
GN-model	25 GBaud	1900 ps/nm	C band
Asymptotic GN-model	28 GBaud	1900 ps/nm	C band
Asymptotic EGN-model	5 GBaud	Nearly zero-dispersion regimes	C band
GGN-model	25 GBaud	1900 ps/nm	C, C+L band

Table 2.1. Summary of the GN models limitations.

CHAPTER 3

Gaussian noise model

3.1. Introduction

In this chapter, the GN-model and its evolutions up to the C-band are presented in more detail. In particular, the GN-model formulas are described and explained as well as their physical meaning. The correct implementation of the models is confirmed by comparing the obtained results with the results provided in the literature. Finally, the impact of the variation of the system parameters on the NLI generation is analyzed. First, in section 3.2, the asymptotic GN-model is addressed, following by the GN and IGN models in section 3.3. Some of the equations parameters presented in the following sections, as well as some definitions, are listed here for convenience:

- z: longitudinal spatial coordinate, along the link (km).
- α: fiber *power* loss coefficient ($\text{Np} \cdot \text{km}^{-1}$). In this work, α is defined as in [10], [30], i.e., in power and not in amplitude. Therefore, in linear units, the signal power is attenuated as $\exp(-\alpha z)$.
- β_2: group-velocity dispersion (GVD) ($\text{ps}^2 \cdot \text{km}^{-1}$), defined as $\beta_2 = -\frac{D\lambda^2}{2\pi c}$ where D is the dispersion parameter measured at the operating wavelength λ and c is the speed of light.
- γ: fiber Kerr non-linearity coefficient ($\text{W}^{-1}\text{km}^{-1}$). In this work, it is employed the definition of γ as in [8], [11], [30], which assumes that the factor $\frac{8}{9}$ is not included in the definition of γ, but is rather included in the Manakov equation used to derive the GN-model. Therefore, $\gamma = \frac{k_0 \overline{n}_2}{A_{eff}}$, where $k_0 = \frac{2\pi}{\lambda}$ is the light wavenumber, $\overline{n}_2$ is the nonlinear fiber index and A_{eff} is the fiber effective area.
- L_s: span length.
- L_{eff}: span effective length, characterized as $L_{eff} = \frac{1-\exp^{-\alpha z}}{\alpha}$.
- N_s: total number of spans in a link.
- N_{ch}: number of WDM channels.
- P_m: power per channel for two polarizations, such that $P_m = P_m^x + P_m^y$.
- $R_{s,m}$: symbol rate of the m-th WDM channel.
- B_m: full bandwidth of the m-th WDM channel. If the channel has a Nyquist spectrum, then $B_m = R_{s,m}$.

- Δf: WDM channel spacing. If the channel is Nyquist WDM, then $\Delta f = B_m$.
- f_m: center frequency of the m-th WDM channel.
- *homogeneous link*: transmission link in which all fiber spans are similar, i.e., all have the same amplification configuration, span length and fiber type [11].
- *uniform WDM signal*: all WDM channels, in each given transmission system configuration, have the same bandwidth, symbol rate, modulation format and launch power [11].

3.2. Asymptotic GN-model

The asymptotic GN-model is the simplest model studied in this work and has been developed with the goal to be a fast and reliable non-linearity model applicable to physical layer aware optical networks [10]. In this section, the main features of this model are described, starting with the model equations in subsection 3.2.1, following by the verification of the correct model implementation in subsection 3.2.2 and finishing with the analysis of the impact of the variation of some system parameters on the model results in subsection 3.2.3. Furthermore, the asymptotic GN-model is also compared with the model without the asymptotic expansion. The model considered in this section has been proposed and is described in [10] in more detail.

3.2.1. Equations and physical meaning

The asymptotic GN-model allows to include separately the effects of SCI and XCI on the PSD of the NLI. In addition, this model assumes that the PSD is equal in both polarizations and thus, the NLI PSD per polarization for channel m and for one single fiber span can simply be written as:

$$G_{NLI}^{1span}(f_m) = G_{SCI}^{1span}(f_m) + \sum_{\substack{m'=1 \\ m' \neq m}}^{N_{ch}} G_{XCI}^{1span}(f_m) \tag{3.1}$$

where $G_{SCI}^{1span}(f_m)$ is the PSD of SCI and represents the contribution of the interference caused by channel m on itself, and $G_{XCI}^{1span}(f_m)$ is the PSD of XCI and constitutes the interference caused by other channels (m') on the channel m (such that $m' \neq m$). Notice that the asymptotic GN-model only allows to determine the PSD of the NLI on the center frequency f_m of the WDM channel. This approximation together with the assumptions described in the previous chapter (section 2.3.1) and considering that the loss of each fiber span is exactly compensated by an optical amplifier, an approximated model has been proposed, defined by [10]:

$$G_{NLI}^{1span}(f_m) = \frac{3(\frac{8}{9}\gamma)^2}{\alpha^2} F_{mm}^2 G_{x,y}^3(f_m) + \sum_{\substack{m'=1 \\ m' \neq m}}^{N_{ch}} \frac{6(\frac{8}{9}\gamma)^2}{\alpha^2} F_{mm'}^2 G_{x,y}(f_m) G_{x,y}^2(f_{m'}) \tag{3.2}$$

where $G_{x,y}(f_m)$ is the transmitted PSD of the WDM channel per polarization at the center frequency f_m. Since this model assumes that the PSD of each WDM channel is rectangular, $G_{x,y}(f_m)$ can be determined by $G_{x,y}(f_m) = \frac{P_m^x}{B_m}$, where P_m^x is the power of channel m per polarization. The parameter $F_{mm'}^2$ must be expressed in terms of the dilog function, which is specified by [10]:

$$\mathrm{Li}_2(z) = \sum_{n=1}^{\infty} \frac{z^n}{n^2} \tag{3.3}$$

Using equation (3.3), it is possible to write $F_{mm'}^2$ as:

$$F_{mm'}^2 = \frac{2}{\xi} \{ \mathrm{Im}\left[\mathrm{Li}_2(jx_1)\right] + \mathrm{Im}\left[\mathrm{Li}_2(jx_2)\right] \} \tag{3.4}$$

where $\mathrm{Im}(\cdot)$ denotes the imaginary part of a complex number, j is the imaginary unit and x_1, x_2 and ξ are defined, respectively, by equations (3.5), (3.6) and (3.7),

$$x_1 = \frac{B_m}{2} \left(f_m - f_{m'} + \frac{B_{m'}}{2} \right) \xi \tag{3.5}$$

$$x_2 = \frac{B_m}{2} \left(f_{m'} - f_m + \frac{B_{m'}}{2} \right) \xi \tag{3.6}$$

$$\xi = \frac{4\pi^2 |\beta_2|}{\alpha} \tag{3.7}$$

where $B_{m'}$ is the bandwidth of the interfering channel m'.

Since this model has to be expressed in terms of the dilog function, a simpler and more intuitive model has been also proposed in [10], which was obtained using the asymptotic expansion of the dilog function (see [10], appendix). The asymptotic GN-model is given by:

$$G_{NLI}^{1span}(f_m) = \frac{3(\frac{8}{9}\gamma)^2 G_{x,y}(f_m)}{2\pi\alpha|\beta_2|} \left[G_{x,y}^2(f_m) \ln \left| \frac{\pi^2 \beta_2 (B_m)^2}{\alpha} \right| + \sum_{\substack{m'=1 \\ m' \neq m}}^{N_{ch}} G_{x,y}^2(f_{m'}) \ln \left(\frac{f_{mm'} + B_{m'}/2}{f_{mm'} - B_{m'}/2} \right) \right] \tag{3.8}$$

where $f_{mm'} \equiv |f_m - f_{m'}|$. Equation (3.8) can also be written in terms of the hyperbolic arcsin function, since $\text{asinh}(x) \approx \ln(2x)$, with a relative error of less than 1% for $x > 3.5$ [8]. In this way, the asymptotic GN-model may be rewritten as:

$$G_{NLI}^{1span}(f_m) = \frac{3(\frac{8}{9}\gamma)^2 G_{x,y}(f_m)}{2\pi\alpha|\beta_2|} \left[G_{x,y}^2(f_m) \,\text{asinh}\left| \frac{\pi^2 \beta_2 (B_m)^2}{2\alpha} \right| + \sum_{\substack{m'=1 \\ m' \neq m}}^{N_{ch}} G_{x,y}^2(f_{m'}) \ln\left(\frac{f_{mm'} + B_{m'}/2}{f_{mm'} - B_{m'}/2} \right) \right] \tag{3.9}$$

Notice that equations (3.2), (3.8) and (3.9) have the γ parameter multiplied by the factor $\frac{8}{9}$, which makes them slightly different in comparison with the equations presented in [10]. This is due to the fact that, in [10], the definition of γ has the factor $\frac{8}{9}$ included. Additionally, notice also that the equations presented in this section are only valid to calculate the NLI PSD for one span. In order to use this model to evaluate the total NLI PSD of a link, an incoherent accumulation of NLI along the link sections must be assumed [10]. In other words, this model assumes that the NLI that reaches the Rx input is just the sum of all the independent NLI contributions generated in each fiber span. Considering the n-th span of a link, the total incoherent NLI PSD is obtained by [8], [10], [17]:

$$G_{NLI}^{link}(f) = \sum_{n\text{-}span=1}^{N_s} G_{NLI}^{n\text{-}span}(f) \tag{3.10}$$

As already pointed out in chapter 2, this model must not be used in dispersion managed systems and it is only valid in UT links with sufficiently high dispersion and for channels with a bandwidth larger than 28 GHz, so that the signal Gaussianity assumption is accomplished. Furthermore, this model is independent of the transmission modulation format and also does not consider the span length influence on the NLI generation.

3.2.2. Implementation confirmation by comparison with literature results

In this subsection, the NLI PSD estimates obtained using the model formulas described in the last subsection are analyzed and compared with the results shown in [10] and with the approximated GN-model formula proposed in [8]. A WDM signal with 21 channels ($N_{ch} = 21$), placed symmetrically around the center frequency 193.1 THz is chosen to perform this study. The symbol rate of each channel is 28 GBaud and as a rectangular spectrum for each WDM channel has been considered, the optical signal bandwidth has been set equal to the symbol rate. Furthermore, it is assumed an uniform WDM signal, where all WDM channels are equal, meaning that all have the same bandwidth and the same power. Three different channel spacings are

considered: 28 GHz (for ideal Nyquist WDM transmission [10]), 50 GHz and 100 GHz. The link parameters considered are: a fiber loss coefficient $\alpha = 0.2\,\mathrm{dB/km}$, a dispersion parameter $D = 16\,\mathrm{ps/(nm \cdot km)}$ and a Kerr non-linearity coefficient $\gamma = 1.4625\,\mathrm{W^{-1}km^{-1}}$. Note that, in [10], $\gamma = 1.3\,\mathrm{W^{-1}km^{-1}}$ due to the different definition of the parameters. The power per channel and polarization is $P_m^x = 0\,\mathrm{dBm}$.

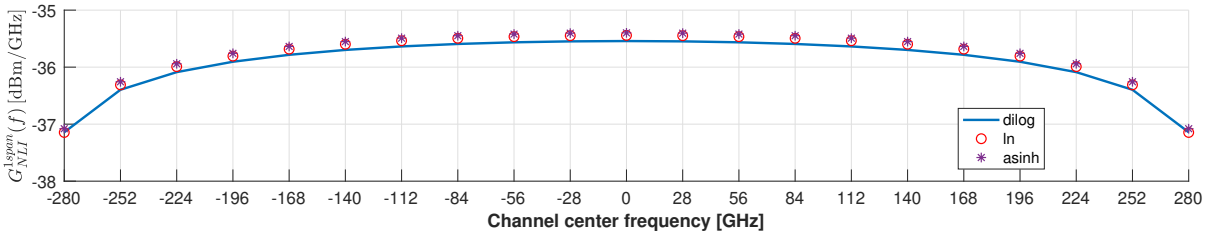

(a) 28 GHz channel spacing.

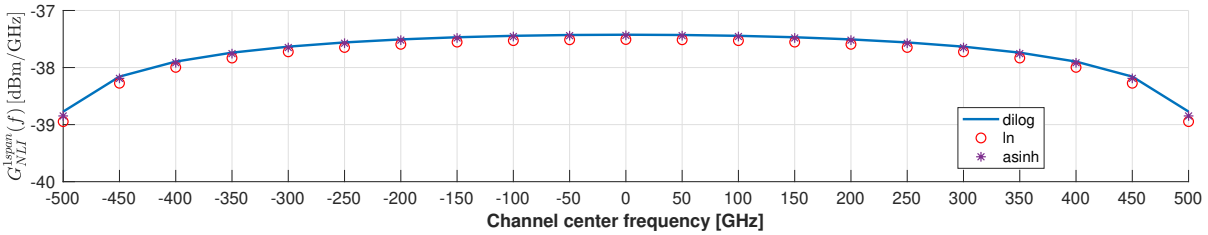

(b) 50 GHz channel spacing.

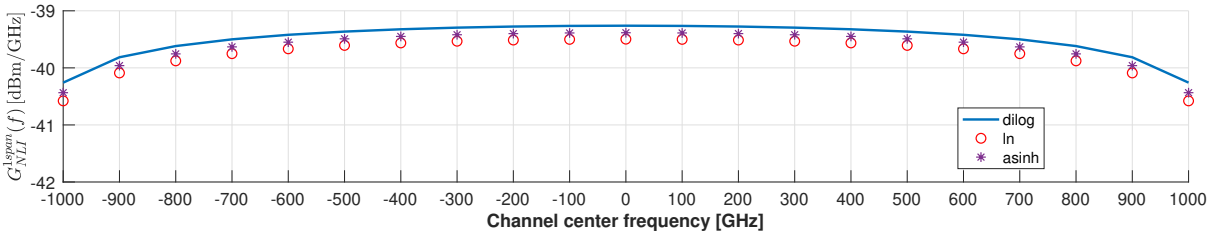

(c) 100 GHz channel spacing.

Figure 3.1. NLI PSD per polarization calculated at the channel center frequencies of a WDM signal with 21 channels. Blue solid line: Dilog results using equation (3.2). Red circles: ln results using equation (3.8). Purple asterisks: asinh results using equation (3.9).

Figure 3.1 depicts the PSD of NLI at the center frequency of each of the 21 channels of the WDM signal, considering a channel spacing of (a) 28 GHz, (b) 50 GHz and (c) 100 GHz. For practical purposes, the NLI PSD low-pass equivalent representation around $f = 0$ is displayed. As previously demonstrated in [8], [10], [17], the maximum value of the PSD of the NLI occurs at the center frequency $f = 0$ of the center channel of the WDM signal and the minimum NLI PSD values correspond to the channels at the edge of the WDM signal. As the SCI is the same for all channels, this can be explained by the stronger impact that XCI has on the center channel. In contrast, XCI has less impact on the channels at the edge of the WDM comb, leading to the lower NLI PSD values. Additionally, it can be seen that, as the channel spacing increases, the

NLI PSD decreases. The highest PSD values happen in the Nyquist WDM scenario (figure 3.1 (a)) and the lowest values occur in the 100 GHz channel spacing situation (figure 3.1 (c)), with the differences being between 3 dB to 4 dB in NLI PSD values between these two spacings. This can be explained by the decreasing impact of XCI as the spacing increases. Thus, at 28 GHz spacing is where there is a higher level of XCI, followed by the 50 GHz and 100 GHz spacings.

By observing figure 3.1, the performance of the different approximated models, described in the last subsection, can be analyzed and compared. For convenience, the results achieved using equation (3.2) are called ”dilog results” and the results obtained based on the equations (3.8) and (3.9) are designated as ”ln results” and ”asinh results”, respectively. For 28 GHz of channel spacing, in figure 3.1 a), the ln and asinh results show NLI PSD estimates slightly higher than the dilog results, with a maximum difference of approximately 0.1 dB. For the 50 GHz spacing, the dilog results are practically the same as the asinh results and are slighly higher than the ln results. In the 100 GHz scenario, the difference between the NLI PSD estimates is clearly higher, being the maximum difference approximately 0.3 dB. Regarding the differences between the ln and asinh results, it can be observed that the asinh results clearly show higher NLI PSD estimates compared to the ln results, regardless of the considered channel spacing.

Due to the agreement of the results shown in figure 3.1 with the results presented in [10], it can be considered that both ln results and dilog results are confirmed. In [10], it is proven that the dilog results overestimate the NLI PSD in comparison with the more accurate GN-model (equation (3) of [10]) and that the asymptotic GN-model given by equation (3.8) is the most accurate. The approximation with the asinh has not been considered in [10]. However, since the asinh approximation show NLI PSD values always higher than the ln approximation, it can be concluded that the ln approximation is the most suitable. Thus, throughout this work, the ln approximation will be the one mostly used and will be denoted as asymptotic GN-model.

To further validate the achieved results, a comparison with another approximated model proposed in the literature is performed. In [8], an analytical GN-model formula to evaluate the PSD of NLI at the center frequency of the WDM comb ($f = 0$) has been proposed. This formula is defined for two polarizations, and so to compare with the NLI PSD estimates for one polarization provided by the asymptotic GN-model, it must be converted to one polarization. The NLI PSD for one polarization can be defined as $G_{NLI}^{x,y}(0) = \frac{G_{NLI}(0)}{2}$, where $G_{NLI}(0)$ is given in equation (15) of [8]. The NLI PSD for one polarization is given by:

$$G_{NLI}^{x,y}(0) \approx \frac{8}{54} \frac{\gamma^2 G^3(0) L_{eff}^2}{\pi |\beta_2| L_{eff,a}} \operatorname{asinh}\left(\frac{\pi^2}{2} |\beta_2| L_{eff,a} B_m^2 [N_{ch}^2]^{\frac{B_m}{\Delta f}} \right) \tag{3.11}$$

where $L_{eff,a} = \frac{1}{\alpha}$ is the asymptotic effective length and $G(0) = \frac{P_m}{B_m}$ is the WDM center channel PSD assuming a rectangular spectrum. According to [8], [17], this equation is only reliable for spans losses $\geq 10\,\text{dB}$, $|\beta_2| \geq 4\,\text{ps}^2 \cdot \text{km}^{-1}$, $R_{s,m} \geq 28\,\text{GBaud}$ and $\frac{B_m}{\Delta f} \geq 0.25$. Only the NLI PSD estimates at the center frequency of the center channel are considered for the comparison between equation (3.8) and (3.11). The system parameters are the same as the ones used to obtain the NLI PSD values presented in figure 3.1. Note that P_m corresponds to the power for two polarizations, i.e., $P_m = 2P_m^x \approx 3.01\,\text{dBm}$, and that the only difference between equation (3.11) and equation (15) in [8] is the factor $\frac{8}{54}$, which accounts for only one polarization. The minimum span length considered is 50 km, to satisfy the reliability requirement of equation (3.11), i.e., that the span losses must be equal or greater than 10 dB.

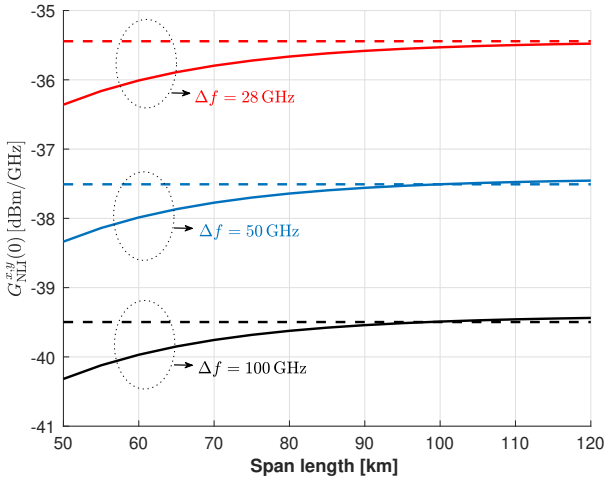

Figure 3.2. NLI PSD at $f = 0$ as a function of the span length and channel spacing. Dashed lines: asymptotic GN-model using equation (3.8). Solid lines: results using equation (3.11).

Figure 3.2 illustrates the NLI PSD for one polarization at $f = 0$ as a function of the span length and channel spacings of 28, 50 and 100 GHz. The dashed lines represent the NLI PSD results using the asymptotic GN-model and the solid lines using equation (3.11). As can be seen from figure 3.2, the NLI PSD estimates, using equation (3.8), remain constant with the variation of the span length, since this model does not depend on this parameter. In contrast, the NLI PSD estimates obtained by equation (3.11) depend on the span length and tend to the results of the asymptotic GN-model for span lengths above 80 km. For 50 GHz and 100 GHz spacings and 80 km of span length, the difference between the two methods is just approximately 0.1 dB. For approximately 100 km, the graph curves are completely overlapped. Above 100 km, the NLI PSD estimates by equation (3.11) surpass slightly the results of the asymptotic method for 50 GHz and 100 GHz spacings. For the 28 GHz spacing, the NLI PSD results show a small

difference of approximately 0.1 dB between the two methods for $L_s = 100$ km and the estimates using the equation (3.11) tend toward the asymptotic GN-model estimates as the length becomes greater than 100 km.

In conclusion, the asymptotic GN-model provides higher NLI PSD estimates up to about 90 km. In a link with a span length of 50 km, this model estimates the NLI PSD by more than 0.9 dB for 28 GHz spacing and by more than 0.8 dB for 50 and 100 GHz spacings. The NLI PSD estimates of both models show a good agreement, which indicates that the asymptotic GN-model is well implemented.

3.2.3. Study of the impact of the system parameters on the NLI generation

To carry out the study of the impact of the variation of the system parameters on the NLI estimated using the asymptotic model given by equation (3.8), several system parameters are varied, such as the number of WDM channels, the channel spacing and the fiber type. The parameters of the three fiber types considered in this study are shown in table 3.1: pure silica-core fiber (PSCF), SMF and non-zero dispersion-shifted fiber (NZDSF). Only one fiber span is considered. The symbol rate of each WDM channel is 32 GBaud and the channel bandwidth is equal to the symbol rate. The power per channel and polarization is $P_m^x = 0\,\text{dBm}$. It is important to remark that the goal of this study is not evaluate the accuracy of the asymptotic GN-model, but rather understand and study the impact of the variation of some of the system parameters on the NLI generation using the asymptotic GN-model.

Fiber	α [dB/km]	D [ps/(nm · km)]	γ [W^{-1} · km^{-1}]
PSCF	0.17	20.1	0.8
SMF	0.2 / 0.22	16.7	1.3
NZDSF	0.22	3.8	1.5

Table 3.1. Parameters of the three fiber types (taken from [38]).

First, the impact of the variation of the number of channels on the NLI PSD is analyzed and compared for all fiber types. The following number of channels are considered: 40, 70 and 100 channels. The asymptotic GN-model is only valid for C-band transmission systems. In this chapter, the C-band is assumed to occupy approximately 5 THz (40 nm) of the available optical spectrum [8], [38]–[40]. This choice is due to the fact that the bandwidth of erbium-doped fiber amplifiers (EDFAs) can be equalized to about 40 nm (approximately 5 THz) [40], [41]. For instance, in [40], a WDM signal bandwidth from 1527.8 nm to 1567.6 nm is used. Thus, for evaluating the performance of the different models up to the C-band limit, a WDM signal centered around 1547.5 nm (193.7 THz) is considered in this chapter. Due to that, the

only channel spacing considered in this study is 50 GHz, in order to examine the impact up to 100 channels on each fiber type, and thus not exceed the occupancy of the C-band. Figure 3.3 depicts the NLI PSD calculated as a function of the center frequency of each WDM channel and of the number of channels for (a) NZDSF, (b) SMF and (c) PSCF.

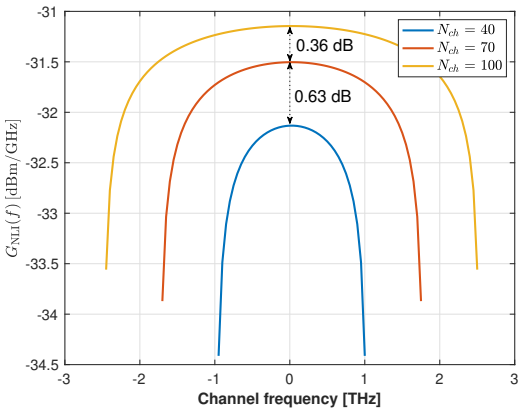

(a) NLI PSD for NZDSF.

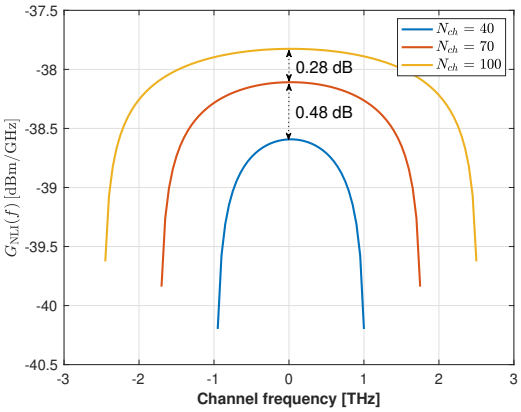

(b) NLI PSD for SMF.

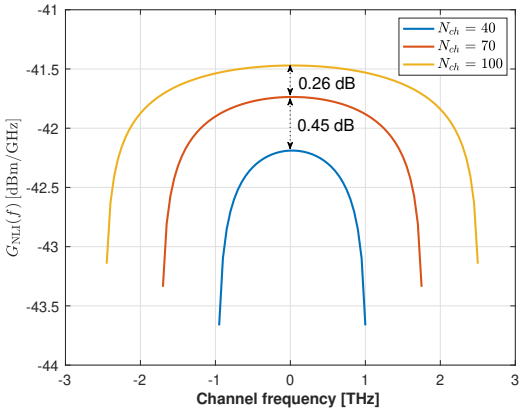

(c) NLI PSD for PSCF.

Figure 3.3. NLI PSD calculated at the channel center frequencies of a WDM signal with 40, 70 and 100 channels, for three fiber types and one span. The channel spacing is 50 GHz.

Figure 3.3 shows that the highest values for NLI PSD happen in the NZDSF, which has the highest non-linearity coefficient ($\gamma = 1.5\,\mathrm{W^{-1}km^{-1}}$), followed by the SMF ($\gamma = 1.3\,\mathrm{W^{-1}km^{-1}}$) and the PSCF, which has the lowest non-linearity coefficient ($\gamma = 0.8\,\mathrm{W^{-1}km^{-1}}$). This figure also allows conclusions to be drawn about the impact of varying the number of channels on NLI generation. For the case of the center frequency of the center channel and for the SMF and PSCF, it can be observed that NLI PSD varies only approximately 0.5 dB if the number of channels goes from 40 to 70 channels and approximately 0.3 dB if the variation is between 70 and 100 channels. In contrast, it is evident that the NZDSF is the one that implies a higher NLI PSD variation, varying 0.6 dB from 40 to 70 channels and approximately 0.4 dB from 70 to

100 channels. Thus, besides the NZDSF being the one with the highest NLI PSD values, it is also the one that is most impacted by the variation of the number of channels. Figure 3.3 allows also to conclude, by observing the NLI PSD increase with the number of WDM channels, that channels far away from the central channel are still contributing to the NLI of that channel, as already demonstrated in [8] and by experimental results in [42].

The impact of varying the channel spacing together with varying the number of channels is now analyzed. For this study, only the NLI powers of the center channel and edge channels of the WDM spectrum are calculated. To determine the NLI power, the locally-white noise (LWN) approximation is considered, since the asymptotic GN-model only allows to calculate the PSD of the NLI at the center frequencies of each channel. This approximation consists of assuming that the PSD of NLI is flat over any single WDM channel [17], [38]. Thus, it is only necessary to estimate the NLI PSD at one specific frequency, typically the center frequency f_m of the channel under test (CUT). The NLI power considering the LWN approximation is given by [17], [38]:

$$P_{NLI}(f_m) \approx G_{NLI}(f_m) \cdot R_{s,m} \tag{3.12}$$

where $G_{NLI}(f_m)$ is the NLI PSD for two polarizations evaluated at the center frequency f_m of the CUT. In this section, the NLI power is calculated only for one polarization.

Five channel spacings are considered: 37.5 GHz, 50 GHz, 62.5 GHz, 75 GHz and 100 GHz. The other system parameters are the same as the ones used to obtain the NLI PSD values presented in figure 3.3. In order not to exceed the 5 THz defined in this chapter for the C-band, the results are displayed and examined as a function of C-band occupancy, which takes into account the impact of varying channel spacing along with varying the number of channels. The C-band occupancy is defined by the ratio:

$$\epsilon_{\text{occupancy}} = \frac{\Delta f N_{ch}}{B_{\text{C-band}}} \tag{3.13}$$

where $B_{\text{C-band}} = 5\,\text{THz}$ is the C-band optical transmission bandwidth. A ratio of 100% means that the WDM signal bandwidth fully occupies the C-band. The results of this study will be presented from 20 channels up to the number of channels occupying 100% of the C-band.

Figure 3.4 (a) depicts the NLI power calculated as a function of the C-band occupancy, for the SMF and the center frequency of the center channel of the WDM signal. Figure 3.4 (b) shows the calculated NLI power as a function of C-band occupancy, for the SMF and for the center frequencies of the center and edge channels of the WDM signal. In figure 3.4 (b) only the results for the 37.5 GHz and 100 GHz spacings are presented for clarity. The solid lines

represent the NLI power of the center frequencies of the center channels and the dash-dotted lines correspond to the NLI power of the center frequencies of the edge channels of the WDM signal.

By observing figure 3.4 (a), it is noted that the power of the center channel increases with the number of WDM channels, as already demonstrated through figure 3.3, being the NLI power growth approximately logarithmic [8]. It can be seen that the NLI power peaks when the C-band is fully occupied for all the considered channel spacings, due to the higher number of WDM channels contributing to NLI. The difference in NLI power between the spacings varies steadily as the number of channels increases, as shown in figure 3.4 (a), which reveals a constant NLI power difference of approximately 1.3 dB, 0.9 dB, 0.7 dB and 1 dB, between respectively, 37.5 GHz and 50 GHz, 50 GHz and 62.5 GHz, 62.5 GHz and 75 GHz and 75 GHz and 100 GHz. Figure 3.4 (a) also demonstrates that the NLI power decreases as the channel spacing increases, since the XCI has less impact, as already pointed out in subsection 3.2.2. Regarding the differences between the center and edge channels, it can be seen in figure 3.4 (b) that the center channel is the most affected by varying the bandwidth of the WDM signal, as the NLI varies less significantly in the edge channels for the channel spacings considered. Furthermore, it can also be seen that the NLI power difference between the center and edge channels decreases with increasing channel spacing and increases slightly (less than 0.5 dB) as the number of channels increases.

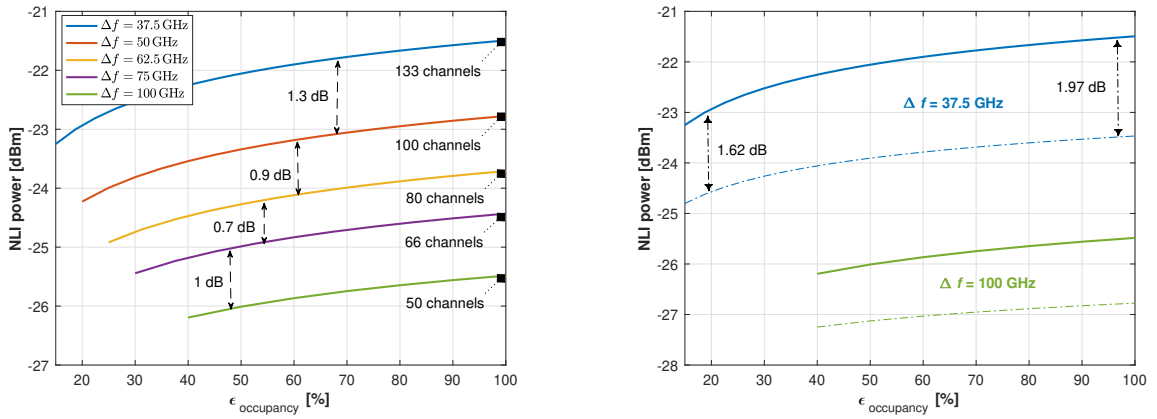

(a) NLI power for the center channel of the WDM signal.

(b) NLI power for the center and edge channels of the WDM signal.

Figure 3.4. NLI power calculated as a function of the C-band occupancy for the SMF. Solid lines: NLI power of the center channel. Dash-dotted lines: NLI power of the edge channels.

The impact of varying the system parameters on the NLI power using other types of fiber is now investigated. Figure 3.5 represents the NLI power in the center channel as a function

of the C-band occupancy and fiber type. For clarity, only the 75 GHz (red lines) and 100 GHz (blue lines) spacings are depicted. The dotted lines correspond to the NZDSF, the solid lines to the SMF and the dash-dotted lines to the PSCF. As can be seen in figure 3.5, the NZDSF is the one that exhibits the highest variation in NLI power with the different channel spacings, followed by the SMF and by the PSCF. As in figure 3.4 (a), it can be noted that the difference in NLI power between the spacings remains approximately constant as the number of channels increases, being 1.6 dB in NZDSF, 1 dB in SMF and 0.9 dB in PSCF.

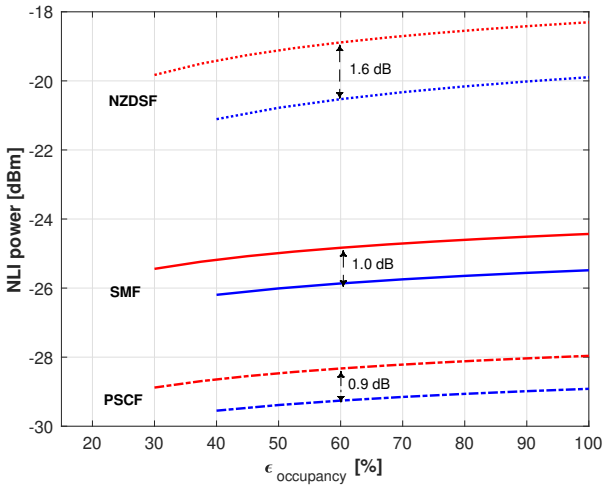

Figure 3.5. NLI power for the center frequency of the center channel as a function of C-band occupancy and fiber type. Blue lines: 75 GHz spacing. Red lines: 100 GHz spacing. Dotted lines: NZDSF. Solid lines: SMF. Dash-dotted lines: PSCF.

In conclusion, the NZDSF is the most affected by the nonlinear effects. This can be explained by the fact that this fiber has the highest non-linearity coefficient and the lowest dispersion parameter, which leads to the increased impact of the SCI and XCI. In [7], the impact of varying the number of WDM channels and channel spacing on the maximum system reach is studied for the three fiber types discussed in this work. The results obtained are in qualitative agreement with those presented in [7], with the NZDSF also being the fiber that obtains the worst performance, i.e., that leads to the lowest maximum system reach, since it is the one that has the highest NLI power.

3.3. GN-model

The GN-model is a nonlinear propagation model that describes the Kerr non-linear effect simply as Gaussian noise, i.e., NLI, at both the optical receiver input and receiver DSP output. The goal of developing this model was to acquire a faster and more practical tool than the SSFM simulations to predict the system performance in UT systems [7], [8], [17], [38]. In subsection

3.3.1, the original coherent and incoherent GN-model equations are explained as well as their physical meaning. In subsection 3.3.2, the model implementation is confirmed by comparison with results published in the literature. Finally, in the last subsection, the GN-model results are compared with the results obtained using the asymptotic GN-model described in section 3.2. Moreover, the evaluation of the impact of the variation of some system parameters on the model accuracy is also studied. The GN-model is the basis of all the other models studied in this work. Its main features are described with more detail in [7], [8], [17] and a detailed mathematical derivation of the model has been published in [21].

3.3.1. Equations, physical meaning and implementation

The GN-model presented in this section considers two polarizations and assumes that each span of the link is made up from one single fiber type [17], [21]. Assuming that all spans in the link are identical and that the loss in each span is exactly compensated by optical amplification, the GN-model reference formula (GNRF) can be written as [8], [17]:

$$G_{NLI}(f) = \frac{16}{27}\gamma^2 \cdot \int_{-\infty}^{\infty}\int_{-\infty}^{\infty} G_{WDM}(f_1)\, G_{WDM}(f_2)\, G_{WDM}(f_1+f_2-f) \cdot \rho(f_1,f_2,f)\cdot \chi(f_1,f_2,f)\, df_2 df_1 \tag{3.14}$$

The GNRF provides the NLI PSD generated at frequency f at the end of a link and can be physically interpreted as describing the beating of each frequency component of the WDM signal with all others (FWM process) along fiber propagation [8], [17]. The parameter $\rho(f_1, f_2, f)$ is the normalized FWM efficiency of the beating of three frequencies f_1, f_2 and $f_3 = f_1 + f_2 - f$, that create SCI, XCI or MCI at frequency f (see figure 2.3 in chapter 2). Assuming lumped amplification, $\rho(f_1, f_2, f)$ is defined by [8], [17]:

$$\rho(f_1,f_2,f) = \left| \frac{1-e^{-\alpha L_s} e^{j4\pi^2\beta_2 L_s (f_1-f)(f_2-f)}}{\alpha - j4\pi^2\beta_2(f_1-f)(f_2-f)} \right|^2 \tag{3.15}$$

Note that the definition of ρ is slightly different in [8], [17], due to the definition of the attenuation coefficient α in amplitude rather than power. The parameter $\chi(f_1, f_2, f)$, which is also called "phased-array factor", takes into account the coherent accumulation of NLI in multi-span links and it is given by [8], [17]:

$$\chi(f_1,f_2,f) = \frac{\sin^2(2N_s\pi^2(f_1-f)(f_2-f)\beta_2 L_s)}{\sin^2(2\pi^2(f_1-f)(f_2-f)\beta_2 L_s)} \tag{3.16}$$

Notice that by considering only one span, $N_s = 1$, the parameter $\chi(f_1, f_2, f)$ is equal to 1. Lastly, the integrated factor $G_{WDM}(f_1)\, G_{WDM}(f_2)\, G_{WDM}(f_1 + f_2 - f)$ represents the product of the WDM signal PSD at the three beating frequencies involved in the FWM process.

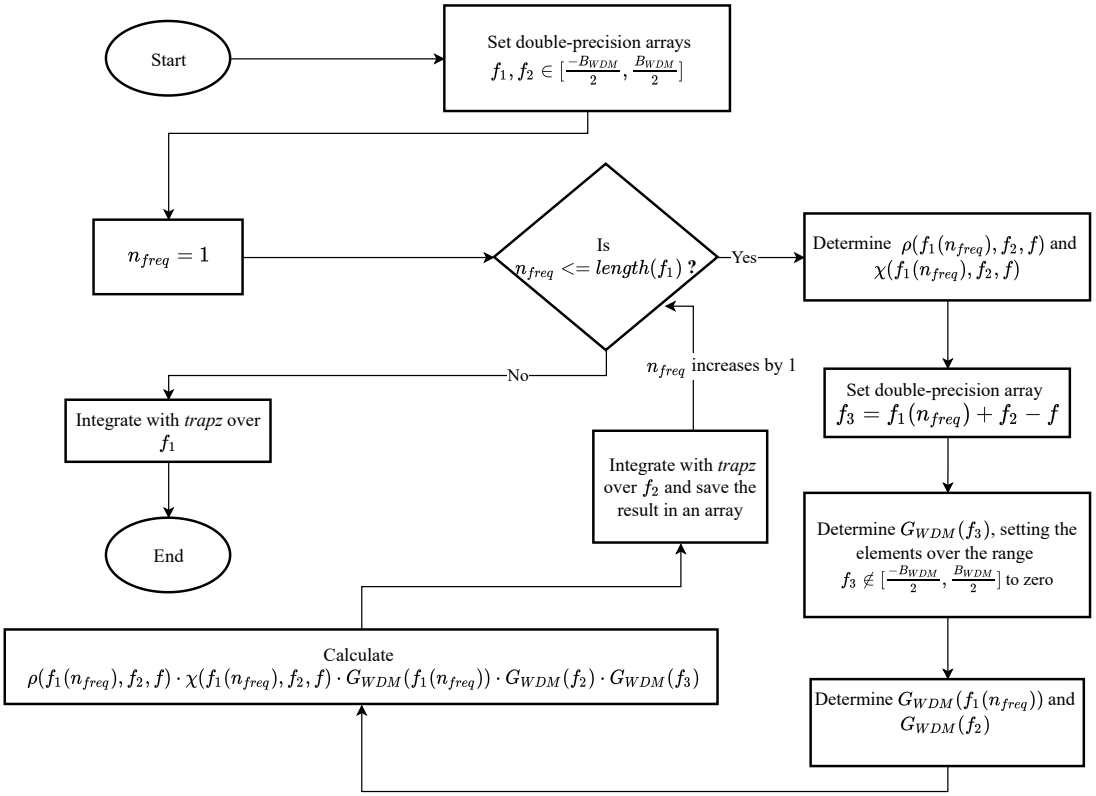

Figure 3.6. Flowchart that describes how the double integration of the GNRF is performed.

Because of the phased-array factor $\chi(f_1, f_2, f)$, equation (3.14) takes into consideration the coherent interference created at the receiver input due to the NLI generated in each span of the link. This factor adds a substantial amount of complexity to the numerical integration of the GNRF [8]. Alternatively, it can be assumed that NLI accumulates incoherently in each fiber span, and in that way, assuming a homogeneous link, the GNRF can be simplified to [17]:

$$G_{NLI}(f) = N_s \frac{16}{27}\gamma^2 \cdot \int_{-\infty}^{\infty}\int_{-\infty}^{\infty} G_{WDM}(f_1)\, G_{WDM}(f_2)\, G_{WDM}(f_1 + f_2 - f) \cdot \rho(f_1, f_2, f)\, df_2 df_1 \tag{3.17}$$

This model is called the incoherent GN-model (IGN-model) and its corresponding equation (3.17) the incoherent GNRF (IGNRF). Note that the IGN-model provides the same NLI PSD prediction as the GN-model if $N_s = 1$, since $\chi = 1$. Both models overestimate the NLI PSD in comparison with the SSFM. However, for most transmission systems, which have much more

than one channel, the IGN-model typically provides more accurate estimates of the NLI PSD as the number of spans increases, despite being an approximation of the GN-model [17]. As already stated in chapter 2, both GN and IGN models should not be used for symbol rates below 25 GBaud and for links with low levels of accumulated dispersion.

Regarding the implementation of the GN-model, the Matlab software is used to compute the GNRF and IGNRF given, respectively, by equations (3.14) and (3.17) at a specific frequency f. To that end, it is not mandatory consider the exact integration domain for f_1 and f_2, i.e., the same number of frequency components. However, in this work, the same integration domain for f_1 and f_2 is considered, being as follows: $f_1, f_2 \in [\frac{-B_{WDM}}{2}, \frac{B_{WDM}}{2}]$, where B_{WDM} is the overall WDM signal bandwidth. In Matlab, f_1 and f_2 are defined as double-precision arrays, where each array position, corresponding to each frequency component belonging to the established integration domain, is denoted as n_{freq}. Note that, consequently, f_3 is also a double-precision array, given by $f_3 = f_1 + f_2 - f$. The double integration in equations (3.14) and (3.17) is performed with the following steps:

(1) First, the integral is calculated along f_2 for each array position n_{freq} corresponding to a frequency component of f_1. The parameter $\rho(f_1(n_{freq}), f_2, f)$ and in the case of the GNRF, the parameter $\chi(f_1(n_{freq}), f_2, f)$, are determined for all frequency components of f_2, as well as the PSD values at the three beating frequencies $G_{WDM}(f_1(n_{freq}))\, G_{WDM}(f_2)\, G_{WDM}(f_1(n_{freq}) + f_2 - f)$. The values of the array $G_{WDM}(f_1(n_{freq}) + f_2 - f)$ that are outside the defined integration domain, i.e., $f_3 < -\frac{B_{WDM}}{2}$ or $f_3 > \frac{B_{WDM}}{2}$, are set to zero.

(2) After computing the inner integral for each frequency component of f_1, testing all possible combinations with f_2 (and corresponding f_3), the outer integral along f_1 is calculated.

The Matlab function *trapz* is used to perform the numerical integrations. The greater the number of frequency components considered within the WDM signal bandwidth (i.e., the length of f_1 or f_2), the more accurate the GNRF calculation will be. In figure 3.6, a flowchart is represented in order to better understand how the double integration of the GNRF is performed.

3.3.2. GN-model implementation and frequency resolution study

In this subsection, the GN and IGN models are implemented and their accuracy is confirmed by comparing with results available in the literature. For that purpose, in this section, a quasi-Nyquist WDM transmission signal (where $\Delta f > R_{s,m}$) is mainly considered. Therefore, the spectrum of each WDM channel can be characterized by a raised-cosine (RC) shape, whose

transfer function can be written as [38]:

$$H_{RC}(f) = \begin{cases} T_s, & \left(0 \leq |f| \leq \frac{1-\beta}{2T_s}\right) \\ \frac{T_s}{2}\left(1+\cos\left[\frac{\pi T_s}{\beta}\left(|f|-\frac{1-\beta}{2T_s}\right)\right]\right), & \left(\frac{1-\beta}{2T_s} < |f| \leq \frac{1+\beta}{2T_s}\right) \\ 0, & \left(|f| > \frac{1+\beta}{2T_s}\right) \end{cases} \tag{3.18}$$

where β is the roll-off factor and T_s is the symbol period defined by $T_s = \frac{1}{R_s}$. The transmitter transfer function $H_{Tx}(f)$ is defined as square-root raised cosine (SRRC), meaning that $|H_{Tx}(f)| = \sqrt{|H_{RC}(f)|}$. Notice that, in this way, the spectrum of the WDM signal $G_{WDM}(f)$, which is used as input to equations (3.14) and (3.17), assumes a SRRC shape at the Tx output. For M-QAM transmission formats, the low-pass equivalent power spectral density $G_{WDM}(f)$ can be written as [43]:

$$G_{WDM}(f) = 2 \cdot \frac{M-1}{3} R_{s,m} \cdot |P(f)|^2 \tag{3.19}$$

where $P(f)$ is the input pulse spectrum, which is equal to $H_{Tx}(f)$ after passing the SRRC filter.

The theoretical equation (3.19) is used to generate the WDM signal spectrum $G_{WDM}(f)$, considering a symbol rate of 32 GBaud. Figure 3.7 illustrates some of the generated WDM spectra that are considered in this section, in order to apply to the GNRF or the IGNRF. For figure 3.7 (a), 9 channels with roll-off $\beta = 0.02$ and 33.6 GHz spacing are taken into account, for (b), 41 channels with rectangular spectrum and 50 GHz spacing, for (c), 11 channels with roll-off $\beta = 0.3$ and 50 GHz spacing, and for (d), 17 Nyquist-WDM channels. By "Nyquist-WDM channels" is meant a system where each WDM channel has a rectangular spectrum ($\beta = 0$) and the channel spacing is equal to the symbol rate. The center frequency of the WDM signal is 193.1 THz. The WDM signals spectra represented in figures 3.7 (c) and (d) are in agreement with those presented in figure 3 and 4 of [17], respectively.

In addition to the assumptions previously mentioned, the transmission links are assumed to be homogeneous, which means that all fiber spans are identical, i.e., all have the same fiber type, span length and amplification configuration, and the WDM signal is considered uniform, i.e., all WDM channels have the same symbol rate, bandwidth, format and optical power. Furthermore, the loss of each span is exactly compensated by an optical amplifier with a gain G. Figure 3.8 depicts the multi-span transmission system scenario considered in this chapter (adapted from figure 2 of [7]).

The GN-model is substantially less intuitive and practical than the asymptotic GN-model presented in section 3.2, due to the complex and time-consuming numerical integration that

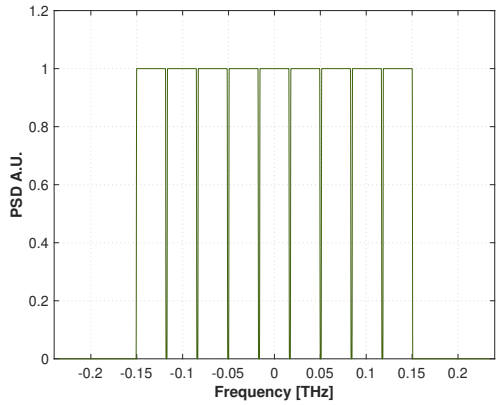

(a) WDM signal PSD for 9 channels with roll-off equal to 0.02 and 33.6 GHz spacing.

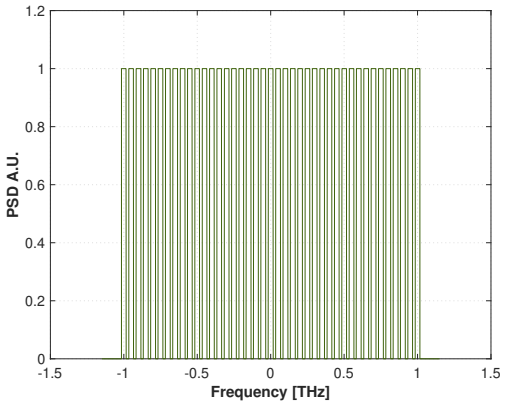

(b) WDM signal PSD for 41 rectangular channels and 50 GHz spacing.

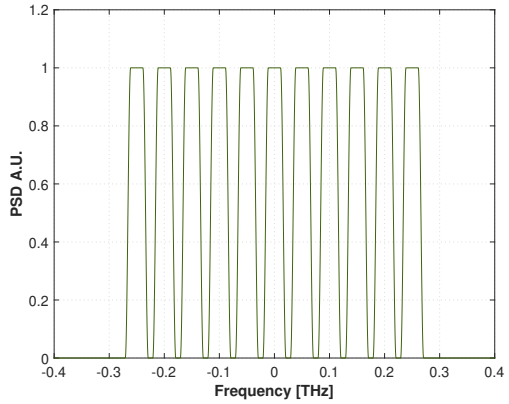

(c) WDM signal PSD for 11 channels with roll-off equal to 0.3 and 50 GHz spacing.

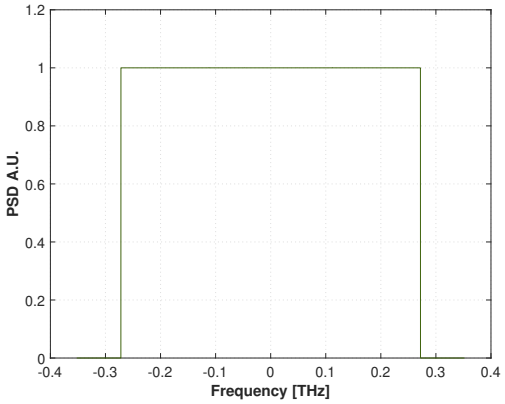

(d) WDM signal PSD for 17 rectangular channels and 32 GHz spacing.

Figure 3.7. WDM signal spectra at the Tx output generated through equation (3.19). The symbol rate is 32 GBaud.

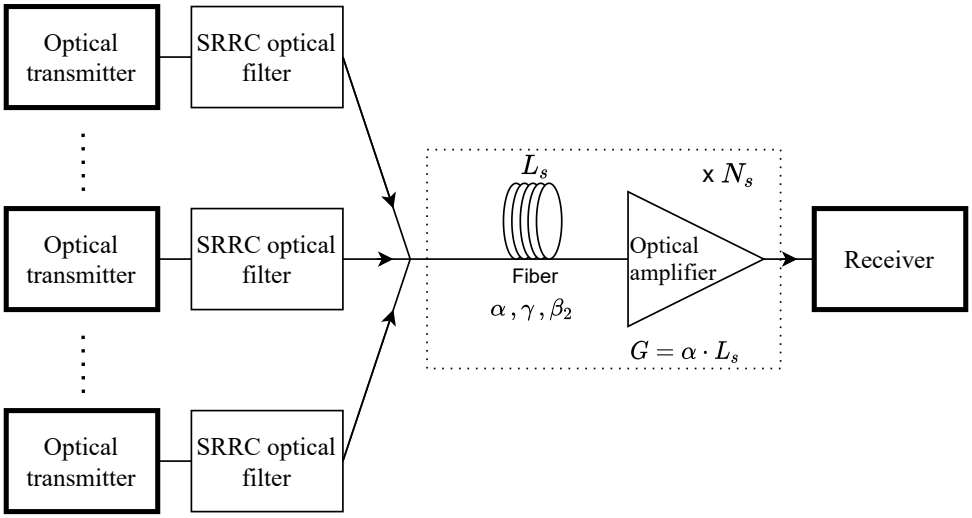

Figure 3.8. Layout of the optical link considered in this chapter (adapted from figure 2 of [7]). The parameter G corresponds to the gain of the optical amplifier at the end of each span of the transmission link.

must be performed to solve equations (3.14) and (3.17). Since the integration domain of the GN-model is considered from $\frac{-B_{WDM}}{2}$ to $\frac{B_{WDM}}{2}$, the numerical integration accuracy is determined by the number of frequency components that are considered within the bandwidth of the WDM signal. The frequency resolution used in the generation of the WDM signal is the parameter that defines the number of frequency components to be integrated. For this reason, an investigation of the impact of the frequency resolution on the accuracy of the numerical integration of the GN-model is performed. The aim of this study is to validate the model and find the minimum number of frequency samples, i.e., the minimum frequency resolution, that is required to achieve a reasonable accuracy in computing the integrals presented in expressions (3.14) and (3.17). To carry out this study, the non-linearity parameter η_{NLI} given by [38]:

$$\eta_{NLI} = \frac{P_{NLI}}{P_m^3} \tag{3.20}$$

is used, which represents the normalized NLI noise power, since it is independent of the power launched in each WDM channel P_m, given that $P_{NLI} \propto P_m^3$ [17]. The normalized NLI power depends only on the link and fiber parameters, so it is constant for a given system configuration. If the LWN approximation is considered, the NLI power can be determined from equation (3.12). Otherwise, the NLI power can be more accurately obtained from [38]:

$$P_{NLI} = \frac{R_{s,m}}{B_H} \int_{-\infty}^{\infty} G_{NLI}(f + f_m)|H_{Rx}(f)|^2 \, df \tag{3.21}$$

where f_m is the center frequency of the channel under test and B_H is a normalization factor, defined as [38]:

$$B_H = \int_{-\infty}^{\infty} |H_{Rx}(f)|^2 \, df \tag{3.22}$$

and $H_{Rx}(f)$ is the overall baseband transfer function of the receiver. In this work, the receiver is assumed matched to the incoming WDM channel, and hence, the receiver transfer function must be a SRRC, given by $|H_{Rx}(f)| = \sqrt{|H_{RC}(f)|}$, where $H_{RC}(f)$ is the RC frequency characteristic defined in (3.18).

Figure 3.9 shows the normalized NLI noise power η_{NLI} of the center channel and corresponding computation time as a function of the frequency resolution, for an uniform WDM signal with 9 PM-QPSK channels operating at 32 GBaud with a roll-off of 0.02. The frequency spacing is 33.6 GHz. Two different fibers are tested: (a) SMF and (b) NZDSF, whose parameters are presented in table 3.1. Figure 3.10 depicts the normalized NLI noise power η_{NLI} of the

center channel and the corresponding computation time as a function of the frequency resolution, for a WDM signal with 41 PM-QPSK channels with (a) 33.6 GHz spacing and (b) 50 GHz spacing. Only the SMF is considered in this case. The transmitted signal spectrum is rectangular with bandwidth equal to the symbol rate of 32 GBaud. Figure 3.9 (a) and (b) use similar parameters as the ones used in figure 7.5 of [38] and figure 7 of [17], respectively. The η_{NLI} values displayed in figure 3.10 are obtained with the same system configuration as the one considered in figure 7.9 of [38].

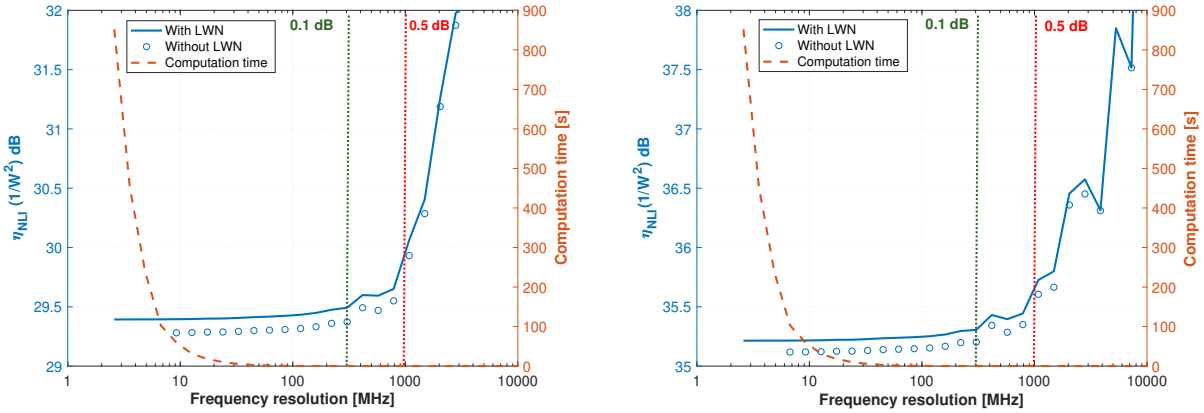

(a) η_{NLI} for $\Delta f = 33.6$ GHz and SMF with $\alpha = 0.2$ dB/km.

(b) η_{NLI} for $\Delta f = 33.6$ GHz and NZDSF with $\alpha = 0.22$ dB/km.

Figure 3.9. Normalized NLI noise power η_{NLI} as a function of the frequency resolution, for a 9-channel PM-QPSK system at 32 GBaud and a 100 km length span, with the LWN approximation using equation (3.12) and without LWN approximation using equation (3.21). Green dotted lines: 0.1 dB NLI overestimation. Red dotted lines: 0.5 dB NLI overestimation.

Both figures 3.9 and 3.10 are obtained for a fiber span with length equal to 100 km. The normalized NLI noise power is obtained using two calculation methods: with and without the LWN approximation. The blue solid lines are the results using the LWN approximation, the blue circles are those without the approximation and the orange dashed lines correspond to the computation time required to determine the NLI PSD at a single frequency. Since only one span is under consideration, the results are valid for both equations (3.14) and (3.17). The computer where the simulations were run, has an Intel Core i7-6700K 4 GHz processor and 16 GB of RAM memory.

Figures 3.9 (a) and (b) indicate that for a frequency resolution of about 300 MHz, the estimated normalized NLI power is only 0.1 dB higher than the most accurate value. Above

300 MHz, η_{NLI} tends to become unstable, with more abrupt variations as the frequency resolution decreases. Below 300 MHz of frequency resolution, the normalized NLI power is approximately constant, indicating that there are enough frequency components for the numerical integration of equation (3.17) to converge. If the LWN approximation is considered, the normalized NLI power stabilizes around 29.4 dB and 35.2 dB for SMF and NZDSF, respectively. On the other hand, if the more precise equation (3.21) is used, it turns out that η_{NLI} decreases by about 0.1 dB, settling with values of 29.3 dB and 35.1 dB for SMF and NZDSF, respectively. For a frequency resolution of about 1000 MHz, the NLI power is only 0.5 dB overestimated, thus representing an appealing option for modeling solutions that have more flexible criteria regarding NLI estimation with not very high demanding computation time. Due to the good agreement in η_{NLI} results for $N_s = 1$ between figure 3.9 (a) and figure 7.5 of [38] and figure 3.9 (b) and figure 7 of [17], it can be concluded that the IGN and GN models for $N_s = 1$ are well implemented. Notice that in [38], it is considered $\alpha = 0.22\,\mathrm{dB/km}$ instead of $\alpha = 0.2\,\mathrm{dB/km}$, being the results presented in figure 3.9 (a) slightly higher than those represented in figure 7.5 of [38].

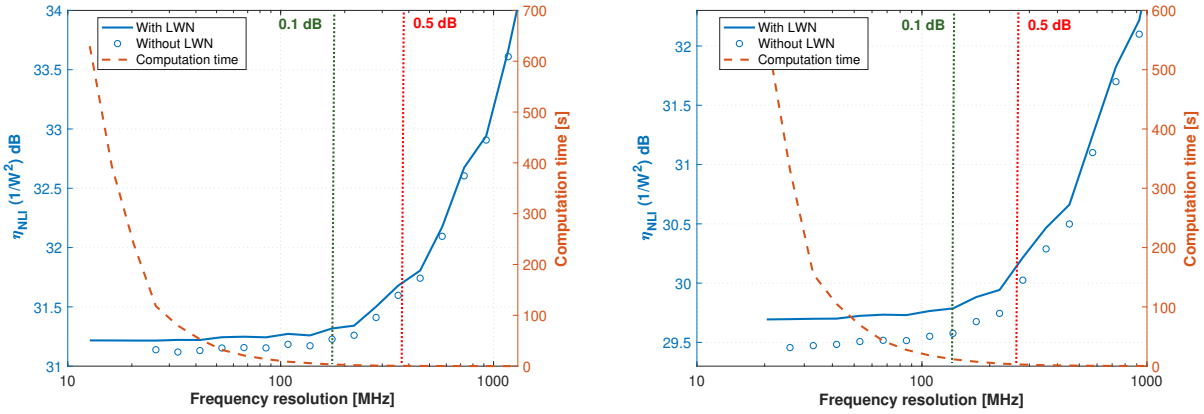

(a) η_{NLI} for $\Delta f = 33.6\,\mathrm{GHz}$ and SMF with $\alpha = 0.2\,\mathrm{dB/km}$.

(b) η_{NLI} for $\Delta f = 50\,\mathrm{GHz}$ and SMF with $\alpha = 0.2\,\mathrm{dB/km}$.

Figure 3.10. Normalized NLI noise power η_{NLI} as a function of the frequency resolution, for a 41-channel PM-QPSK system at 32 GBaud and a 100 km length span, with the LWN approximation using equation (3.12) and without the LWN approximation using equation (3.21). Green dotted lines: 0.1 dB NLI overestimation. Red dotted lines: 0.5 dB NLI overestimation.

By examining figure 3.10, it can be stated that the normalized NLI power remains almost constant until about 170 MHz in (a) and 140 MHz in (b), frequency where there is a 0.1 dB difference relative to the most accurate value obtained for higher frequency resolutions. Below

this threshold and taking into account the LWN approximation, the normalized NLI power stabilizes at about 31.2 dB for the 33.6 GHz spacing and at about 29.7 dB for the 50 GHz spacing. Without the LWN approximation, it is inferred that η_{NLI} decreases by about 0.1 dB for the 33.6 GHz spacing and about 0.2 dB for the 50 GHz spacing, flattening out at around 31.1 dB and 29.5 dB, respectively. For applications where it is not necessary to have a very strict NLI accuracy, a frequency resolution of about 360 MHz for 33.6 GHz spacing and about 280 MHz for 50 GHz spacing can be used, as it leads to only 0.5 dB of η_{NLI} overestimation. The η_{NLI} results for $N_s = 1$ are very similar to those presented in figure 7.9 of [38], which permits to conclude that the model estimates correct results for this system configuration. As in the case of figure 3.9 (a), it is important to remark that the η_{NLI} results for $N_s = 1$ in figure 3.10 are slightly higher than those displayed in figure 7.9 of [38], due to in [38] being considered $\alpha = 0.22\,\mathrm{dB/km}$ instead of $\alpha = 0.2\,\mathrm{dB/km}$.

Both figures 3.9 and 3.10 show that as the frequency resolution decreases, the numerical integration of equations (3.14) and (3.17) takes less time to perform, since there are fewer and fewer frequency components to integrate. Setting a 0.1 dB difference as the threshold in relation to the most accurate value, the 9-channel PM-QPSK system is the one that needs the lower time to reach this threshold with less than 100 milliseconds, followed by the 41-channel system with 33.6 GHz spacing with about 3 seconds and finally the 41-channel system with 50 GHz spacing with about 11 seconds. Thus, as the overall bandwidth of the WDM signal becomes larger, the more time-consuming is to numerically integrate the IGNRF or the GNRF for $N_s = 1$. In conclusion, the value of the frequency resolution has a direct impact on the computation time of the model. Higher values of frequency resolution improve the model computation accuracy, however, at the cost of higher computation times, which may make this approach unfeasible for large WDM signal bandwidths. On the other hand, when lower frequency resolutions are considered, overestimated NLI PSD predictions can be obtained. Therefore, it is essential to find a balance between a good model accuracy and an acceptable calculation time.

In the following, the coherent GN-model is applied to multi-span links. First, an assessment of the impact of frequency resolution on the accuracy of the numerical integration, considering the GN-model for more than one fiber span, is performed. Then, the differences between IGN and GN models from 1 up to 50 spans are examined. The system configurations considered are the same as the ones used in figures 3.9 and 3.10.

Figure 3.11 displays the non-linearity parameter η_{NLI} as a function of the frequency resolution and number of spans, for a SMF link and (a) $N_{ch} = 9$ with $\Delta f = 33.6\,\mathrm{GHz}$, (b) $N_{ch} = 41$

with $\Delta f = 33.6\,\text{GHz}$ and (c) $N_{ch} = 41$ with $\Delta f = 50\,\text{GHz}$. Additionally, in figure 3.11 (d), it is depicted the computation time for the system configuration of figure 3.11 (c) and $N_s = 20$. The coherent GN-model given by the GNRF (3.14) is considered. Unlike the IGN-model, the GN-model takes into account the coherent accumulation of NLI along the link spans. Therefore, in addition to analyzing the impact of η_{NLI} with the variation of the frequency resolution, this study also aims to investigate the role of the number of spans in choosing a frequency resolution that leads to an accurate NLI estimation. The number of spans taken into account are: 2,5,10,20 and 50. For the calculation of the NLI power, the LWN approximation is used.

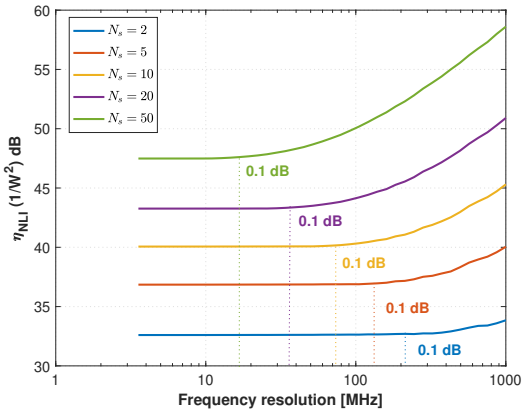

(a) η_{NLI} for $N_{ch} = 9$ with $\beta = 0.02$ and $\Delta f = 33.6\,\text{GHz}$.

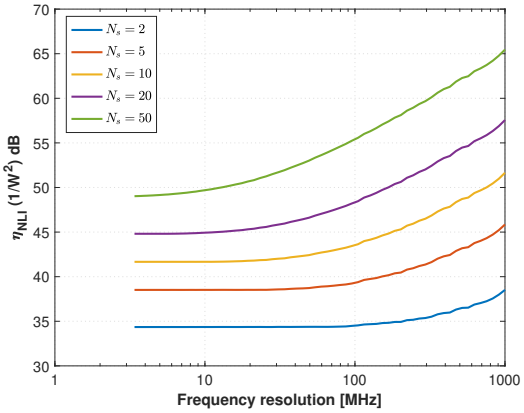

(b) η_{NLI} for $N_{ch} = 41$ with $\beta = 0$ and $\Delta f = 33.6\text{GHz}$.

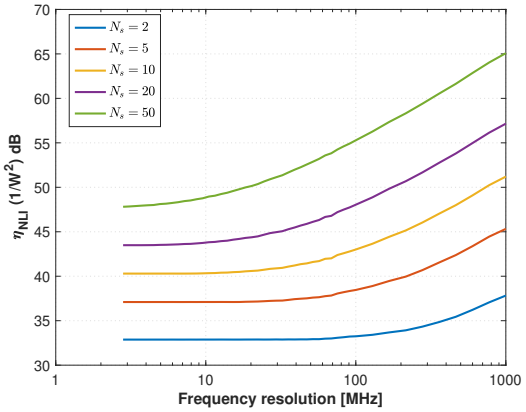

(c) η_{NLI} for $N_{ch} = 41$ with $\beta = 0$ and $\Delta f = 50\,\text{GHz}$.

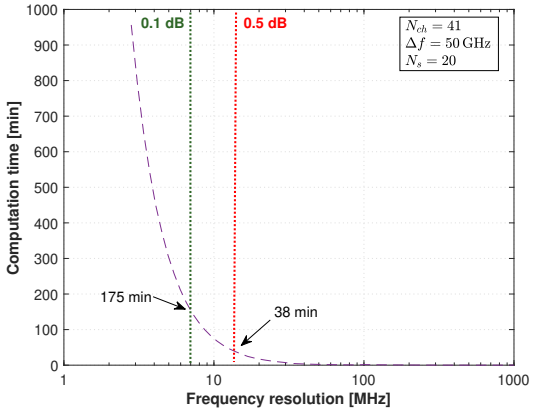

(d) Computation time for $N_{ch} = 41$ and $\Delta f = 50\,\text{GHz}$, with $N_s = 20$.

Figure 3.11. η_{NLI} as a function of the frequency resolution and number of SMF spans. The SMF attenuation is $\alpha = 0.2\,\text{dB/km}$. For the calculation of the NLI power, the LWN approximation given by (3.12) is used.

By analyzing the differences between the three system configurations, it can be seen that it is in figure 3.11 (c), with 41 channels and 50 GHz spacing, where there is the need to use higher frequency resolutions for the η_{NLI} parameter to stabilize. Furthermore, regardless of the

system configuration considered, it is inferred that to obtain accurate η_{NLI} estimates, a higher frequency resolution should be used for systems with a higher number of spans. For example, in figure 3.11 (a), frequency resolutions of 17 MHz, 39 MHz, 70 MHz, 139 MHz and 212 MHz correspond to 0.1 dB of η_{NLI} overestimation for $N_s = 50$, $N_s = 20$, $N_s = 10$, $N_s = 5$ and $N_s = 2$, respectively. Additionally, by observing figure 3.11 (d), it is clear that using the GN-model is significantly more time-consuming than using the IGN-model for more than one fiber span. Taking the case of $N_s = 20$ as an example, the GN-model requires approximately 3 hours to obtain a η_{NLI} with a 0.1 dB overestimation, while the IGN-model requires only 11 seconds for the same system configuration, as can be seen in figure 3.10 (b). Notice that the computation time of the IGN-model is the same regardless of the number of spans considered. In conclusion, it is noticeable that the GN-model is more time demanding than the IGN-model and that the larger the number of spans considered, the greater the need for a higher frequency resolution for the GNRF numerical integration to converge to a constant η_{NLI} value.

The fact that the coherent GN-model is considerably more time-consuming than the IGN-model and requires more frequency components as the number of spans increases is justified in figure 3.12, which shows the phased-array factor $\chi(f_1, f_2, 0)$ with $f = 0$ and $f_1 = 10$ GHz, over the interval $f_2 \in [-0.1, 0.1]$ THz. The phased-array factor $\chi(f_1, f_2, 0)$ results are depicted for figure 3.12 (a) $N_s = 10$ and a frequency resolution of 40 MHz, figure 3.12 (b) $N_s = 50$ and a frequency resolution of 40 MHz and figure 3.12 (c) $N_s = 50$ and a frequency resolution of 4 MHz. The system configuration is the same as in figure 3.11 (a). Notice that a frequency resolution of 40 MHz corresponds to a very stable normalized NLI power value for $N_s = 10$ and to about 0.8 dB of normalized NLI power overestimation for $N_s = 50$. In contrast, a frequency resolution of 4 MHz represents an accurate η_{NLI} calculation for all the number of fiber spans considered in figure 3.11 (a).

According to [8], the factor $\chi(f_1, f_2, 0)$ is characterized by very steep peaks with a height of N_s^2 and with a width inversely proportional to N_s. By analyzing figure 3.12 (a), it can be seen that is very similar to figure 21 of [8], since for $N_s = 10$, the peaks have all height equal to 100 and width inversely proportional to N_s. On the other hand, in figure 3.12 (b) for $N_s = 50$, the amplitude and width of the peaks are not well defined and vary, causing the normalized NLI power to be overestimated by about 0.8 dB, as can be seen when the frequency resolution is 40 MHz in figure 3.11 (a). However, by examining figure 3.12 (c), it is inferred that when the frequency resolution is increased to 4 MHz for $N_s = 50$, all peaks are already well defined with height equal to N_s^2. Therefore, it is concluded that, as the number of spans considered increases,

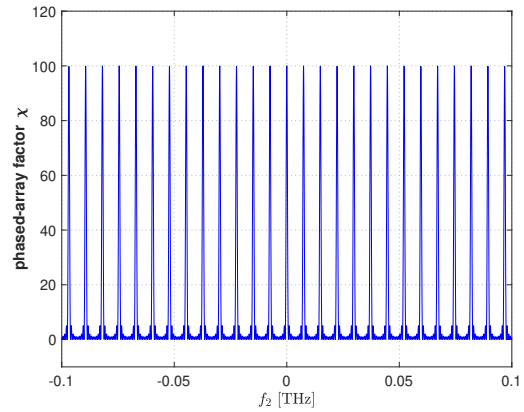

(a) Factor $\chi(f_1, f_2, 0)$ for $N_s = 10$ and 40 MHz resolution.

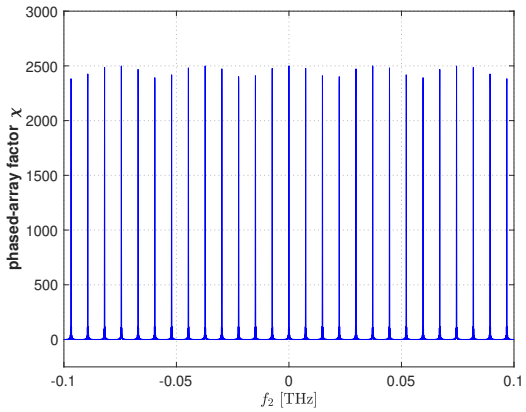

(b) Factor $\chi(f_1, f_2, 0)$ for $N_s = 50$ and 40 MHz resolution.

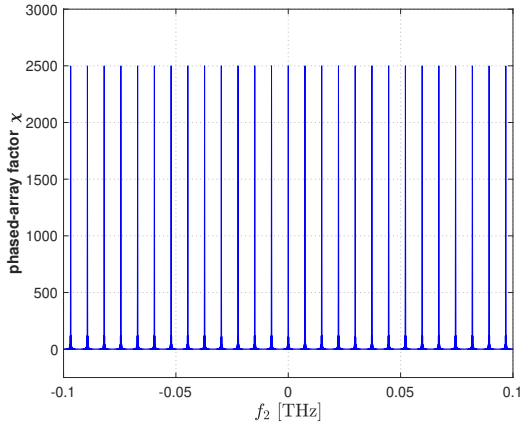

(c) Factor $\chi(f_1, f_2, 0)$ for $N_s = 50$ and 4 MHz resolution.

Figure 3.12. Phased-array factor $\chi(f_1, f_2, 0)$ for $f_1 = 10\,\text{GHz}$ and $f_2 \in [-0.1, 0.1]$ THz.

more frequencies components must be taken into account in order to precisely represent the phased-array factor.

In the following, the implementation of GN and IGN models is now confirmed for different fibers and different system configurations. Figure 3.13 represents the normalized NLI power η_{NLI} as a function of the number of spans, for (a) $N_{ch} = 9$ with $\beta = 0.02$ and $\Delta f = 33.6\,\text{GHz}$ and (b) $N_{ch} = 41$ with $\beta = 0$ with spacings of $\Delta f = 33.6\,\text{GHz}$ and $\Delta f = 50\,\text{GHz}$. In figure 3.13 (a), results for the SMF (orange lines) and NZDSF (blue lines) are shown, while in figure 3.13 (b) only results obtained with the SMF are presented. The solid lines correspond to the GN-model and the dash-dotted lines to the IGN-model. The SMF and NZDSF parameters are shown in table 3.1, being $\alpha = 0.22\,\text{dB/km}$. The NLI power is determined by equation (3.21) without the LWN approximation. The WDM signal spectra are generated with frequency resolutions adjusted according to the number of spans considered, being the maximum η_{NLI} prediction

error about 0.1 dB. In order to confirm the implementation of the GN models, figures 3.13 (a) and (b) are compared with figure 7 of [17] and figure 7.9 of [38], respectively.

As expected, in figure 3.13 (a), it can be observed that when the link consists of only one span, the GN-model and the IGN-model estimate the same normalized NLI power, that is, about 28.8 dB for SMF and around 35.1 dB for NZDSF. As the number of spans increases, the GN-model begins to predict higher η_{NLI} than the IGN-model. For $N_s = 50$, the difference in the η_{NLI} estimates between the GN and IGN models amounts to around 1.3 dB and 1.1 dB for NZDSF and SMF, respectively. Notice that, in [17], [38], it was proven that the IGN-model is more accurate in estimating the NLI power than the GN-model as the number of spans increases, by comparison with the SSFM results. From figure 3.13 (b), it can be noted that with $N_{ch} = 41$, the GN-model provides lower normalized NLI power predictions with $\Delta f = 50$ GHz than with $\Delta f = 33.6$ GHz. This can be explained by the decreasing levels of XCI as the channel spacing increases. Lastly, due to the high similarity of figure 3.13 (a) with figure 7 of [17] and of figure 3.13 (b) with figure 7.9 of [38], it can be concluded that both the GN-model and the IGN-model are correctly implemented for multi-span links.

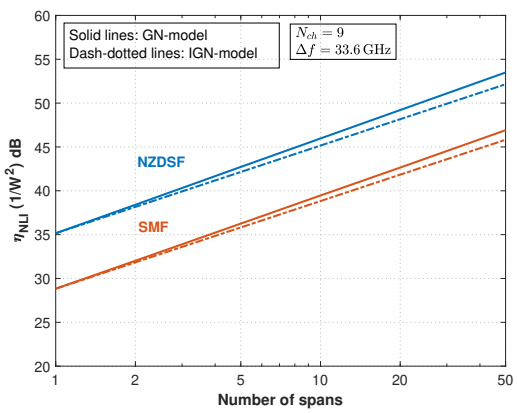

(a) η_{NLI} for 9 channels with roll-off equal to 0.02 and 33.6 GHz spacing.

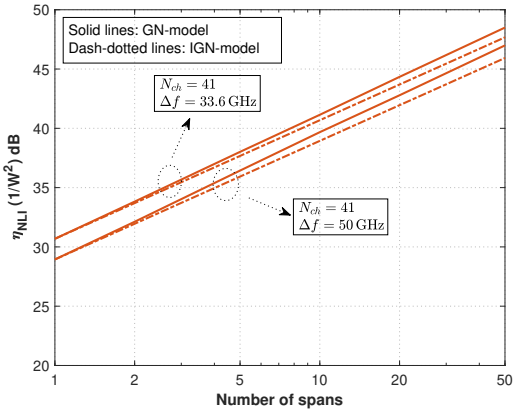

(b) η_{NLI} for 41 rectangular channels, for 33.6 GHz and 50 GHz spacings.

Figure 3.13. Normalized NLI power η_{NLI} as a function of the number of spans.

To complete the verification of the correct implementation of the model, its accuracy when estimating the NLI PSD of all frequencies of the WDM signal is now evaluated. In addition, the implementation is also confirmed for signals with roll-off higher than 0.02. The results that will be used to confirm the GN models implementation are represented in figures 3 and 4 of [17].

Figure 3.14 (a) illustrates the transmitted signal spectrum, zoomed on the center channel, and the corresponding PSD of NLI noise estimated using the GN and IGN models, for $N_{ch} = 11$ and $\beta = 0.3$. The corresponding WDM spectrum is represented in figure 3.7 (c). Figure 3.14

(b) shows the transmitted signal spectrum for 17 Nyquist-WDM channels and the corresponding NLI PSD. The link parameters are the following: $N_s = 20$, $L_s = 100\,\text{km}$, $\alpha = 0.2\,\text{dB/km}$, $\beta_2 = -20.7\,\text{ps}^2/\text{km}$ and $\gamma = 1.3\,\text{W}^{-1} \cdot \text{km}^{-1}$. The green lines represent the PSD of the transmitted signal, the blue lines the NLI PSD using the GN-model and the red lines the NLI PSD determined by IGN-model.

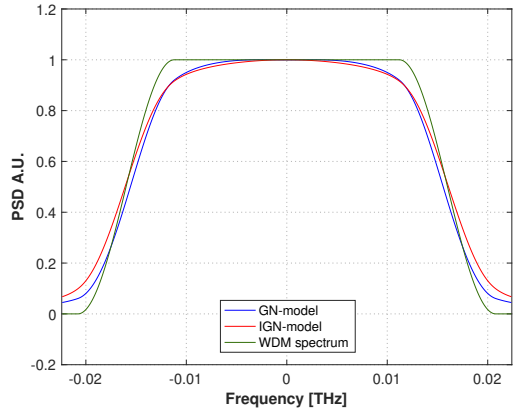

(a) NLI PSD and PSD of the transmitted signal, with $R_{s,m} = 32\,\text{GBaud}$ and with $\beta = 0.3$, zoomed on the center channel.

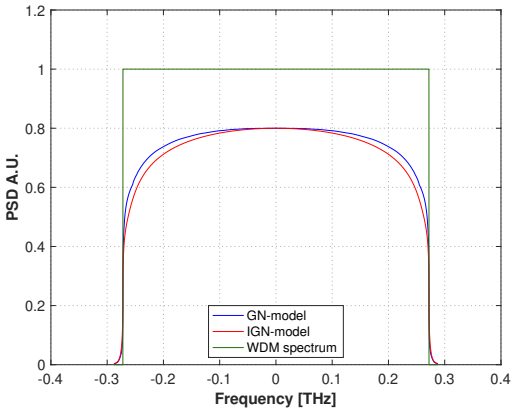

(b) NLI PSD and PSD of the transmitted signal, equivalent to 17 Nyquist-WDM channels at 32 GBaud.

Figure 3.14. NLI PSD and PSD of the transmitted signal for $N_s = 20$ and $L_s = 100\,\text{km}$, for (a) $N_{ch} = 11$ with $\beta = 0.3$ and (b) 17 Nyquist-WDM channels.

By observing figure 3.14 (a), it can be seen that the NLI PSD has a similar shape to the PSD of the transmitted channel, independently of the model used. However, it can be observed that between -0.01 and 0.01 THz, the NLI PSD has a flatter shape when estimated using the GN-model than with the IGN-model, providing higher NLI PSD predictions. At the WDM channel edges, the IGN-model provides higher NLI PSD estimates than the GN-model. Note that the center channel is always the most impacted by NLI. Regarding the Nyquist-WDM signal represented in figure 3.14 (b), it can be stated that the NLI PSD is flat over the center channel for both models. Outside the center channel, the GN-model provides higher NLI PSD predictions than the IGN-model. The very good agreement between figure 3.14 (a) and figure 3 of [17], and figure 3.14 (b) and figure 4 of [17], shows that the GN and IGN models are well implemented for all frequencies of the WDM signal and for spectra with high roll-off.

3.3.3. Impact of the system parameters on the GN-model accuracy and comparison between GN-model variants

First, in this subsection, the effect of decreasing the frequency resolution of the CUT to calculate the NLI power over the center channel is studied. Then, the NLI PSD estimates using the

different variants of the GN-model presented in this work are analyzed and their accuracy is compared for different system configurations.

As noted previously, the NLI power can be determined using the equation (3.21) or by resorting to the so-called LWN approximation given by equation (3.12). The simplicity of the latter calculation method is accomplished at the cost of slightly overestimating the power of the NLI. For instance, for a transmission system with 25 channels, the NLI power is around 0.3 dB overestimated for $\Delta f = 50\,\text{GHz}$ and around 0.2 dB for $\Delta f = 35\,\text{GHz}$ [17]. Therefore, for applications where it is required to estimate very accurately the NLI in the system, the NLI power given by equation (3.21) should be considered. However, while calculating the NLI power using the LWN approximation is straightforward, calculating it using equation (3.21) constitutes a greater challenge, related to the fact that solving this equation requires to evaluate the NLI PSD at each frequency f within the CUT. In addition, and as already pointed out in this work, the correct frequency resolution of the arrays f_1 and f_2 must be considered in order to achieve a good accuracy in the NLI PSD estimation through equations (3.14) and (3.17). The higher the frequency resolution, the greater the number of frequencies components present in the entire WDM signal, i.e., the greater the length of the array f_1 and f_2. Consequently, if the same frequency resolution of f_1 or f_2 is considered within the CUT, the higher is the number of frequencies components that must be taken into account to calculate the NLI power in that same channel. In this scenario and for high WDM signal bandwidths, which require high frequency resolutions, the process of solving the integral of equation (3.21) can be very time-consuming. Given this, the impact of decreasing the frequency resolution within the CUT on the NLI power estimation accuracy is analyzed. This study is performed by decreasing the number of frequency components inside the CUT, while maintaining the frequency resolution of the WDM signal (the length of f_1 and f_2) in order to accurately calculate the NLI PSD at each frequency f.

In figure 3.15, the normalized NLI power η_{NLI} is shown as a function of the CUT frequency resolution, for different systems configurations. The analysis is done for one span and by considering the center channel of the WDM comb as the CUT. The system parameters are the same as the ones used in figures 3.9 and 3.10. The WDM signal is generated with the arrays f_1 and f_2 having a frequency resolution equal to 50 MHz. As shown in figures 3.9 and 3.10, this frequency resolution corresponds to a very precise computation of η_{NLI}, regardless of the system configuration addressed.

Notice that 50 MHz of frequency resolution corresponds to the maximum accuracy in the NLI power calculation that can be obtained, since the frequency resolution of the CUT is the

same of the arrays f_1 and f_2. For the system configurations with 33.6 GHz, the η_{NLI} variations are always less than 0.1 dB up to 4.8 GHz of frequency resolution, which corresponds to a frequency resolution where there are only 6 frequency components inside the CUT bandwidth for the calculation of NLI power. Above 1 GHz of the CUT frequency resolution, for 41 channels and 50 GHz of channel spacing, there are more oscillations in the η_{NLI} estimates, reaching maximums deviations of around 0.3 dB to the most precise value. As a main conclusion, figure 3.15 shows that the accuracy of the calculation of the NLI power is not greatly affected by decreasing the frequency resolution of the center channel up to 1 GHz.

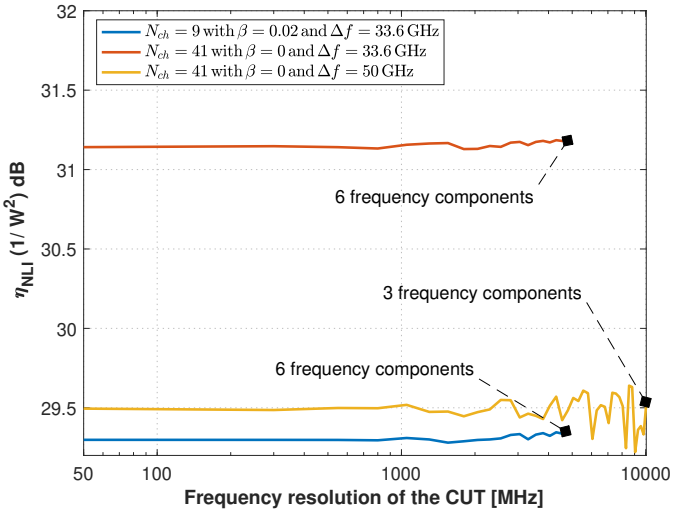

Figure 3.15. Normalized NLI power η_{NLI} over the center channel as a function of the CUT frequency resolution. NLI power calculated using equation (3.21). SMF parameters: $L_s = 100$ km and $\alpha = 0.2$ dB/km.

In the following, the estimation of the NLI using the different GN models is performed and discussed. The GN models predictions accuracy is tested for several system configurations, in order to assess their limitations and validation range. The variants of the GN-model studied so far demand different levels of complexity. Consequently, these studies also aim to clarify which GN-model should be used depending on the accuracy criteria for a given system configuration. As mentioned in section 3.2, one of the main assumptions of the asymptotic GN-model is that the transmitted spectrum is rectangular. In the following studies, spectra with $\beta = 0$ and $\beta = 0.1$ are considered, in order to evaluate possible inaccuracies of the asymptotic GN-model due to the higher roll-off. Furthermore, the LWN approximation is used to determine the NLI power, since the asymptotic GN-model is only valid for evaluating the NLI PSD at the center frequency of each channel. As a final remark, it is important to note that the following studies consider two signal polarizations. Therefore, equation (3.8) of the asymptotic GN-model and the simplified

equation (3.11) are multiplied by a factor of 2 in order to compare their results with the results obtained from the GN and IGN models.

The NLI PSDs for the center frequencies of each WDM channel are depicted in figure 3.16. Two system configurations are considered: (a) 9 channels with 33.6 GHz spacing and (b) 41 channels with 33.6 GHz spacing. The power per channel is -6 dBm. The results displayed in orange, blue and yellow correspond to the GN-model, the asymptotic GN-model and the IGN-model, respectively. The solid lines refer to the estimates obtained with $\beta = 0$ and the circles to the ones obtained with $\beta = 0.1$.

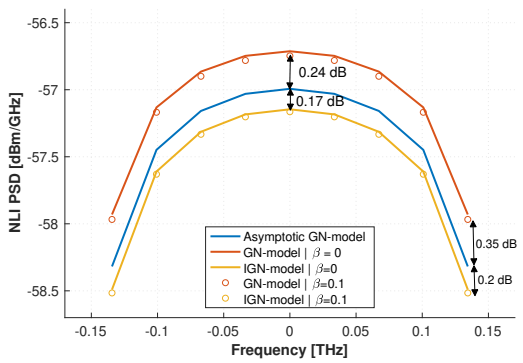

(a) NLI PSD calculated at the center frequency of each WDM channel for $N_{ch} = 9$ and $\Delta f = 33.6\,\text{GHz}$.

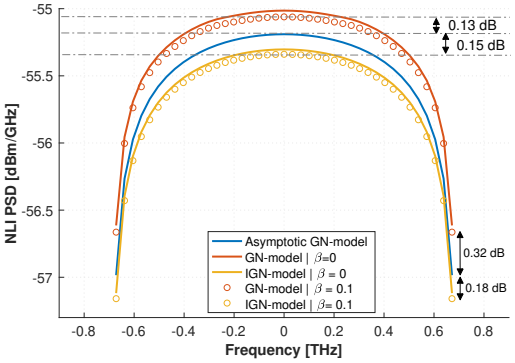

(b) NLI PSD calculated at the center frequency of each WDM channel for $N_{ch} = 41$ and $\Delta f = 33.6\,\text{GHz}$.

Figure 3.16. NLI PSD calculated at the center frequencies of each WDM channel, with $\beta = 0$ and $\beta = 0.1$ and for 5 spans of SMF with $\alpha = 0.22\,\text{dB/km}$.

As expected, the GN-model provides the highest NLI PSD predictions, followed by the asymptotic GN-model and the IGN-model. In figure 3.16 (a), by considering $\beta = 0.1$, the difference in the NLI PSDs in the center channel is about 0.24 dB between the GN-model and the asymptotic GN-model and around 0.17 dB between the asymptotic and IGN models. In figure 3.16 (b), it can be seen that the NLI PSD differences between the models decrease to only 0.13 dB and 0.15 dB. Therefore, it can be inferred that as the WDM signal bandwidth increases, the GN-model predictions tend to approximate to those of the asymptotic GN-model. For the edge channels, the difference in NLI PSD estimates is about 0.2 dB between the IGN and asymptotic models. Between the GN-model and the asymptotic GN-model, the difference is about 0.3 dB. Notice that, according to the results depicted in figure 3.13, if $N_s > 5$, it can be deduced that the discrepancy in the NLI predictions between the GN-model and its variants tends to grow as the number of spans increases.

As previously mentioned, the asymptotic GN-model does not take into account the influence of span length in the NLI generation. In section 3.2.2, a study of the dependence of the span

length is performed and the results obtained are shown in figure 3.2. In this section, the same study is carried out by including the GN-model. Figure 3.17 represents the variation of the normalized NLI power η_{NLI} with the SMF span length, for (a) $N_s = 1$ and (b) $N_s = 5$. The number of WDM channels is 41 and the channel spacings are: 33.6 GHz (purple lines), 50 GHz (blue lines) and 100 GHz (black lines). The dashed, dash-dotted, dotted and solid lines correspond, respectively, to equation (3.11), IGN-model, GN-model and asymptotic GN-model. Note that, in figure 3.17 (a), the results displayed by the dash-dotted lines are valid for both GN and IGN models, since the analysis is done for N_s = 1.

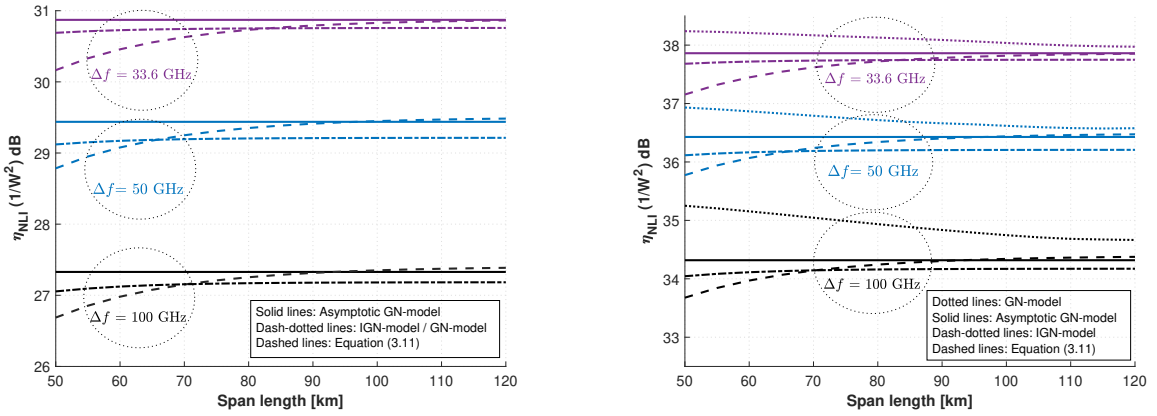

(a) η_{NLI} for $N_s = 1$. (b) η_{NLI} for $N_s = 5$.

Figure 3.17. Normalized NLI power η_{NLI} versus the length of span, for $N_{ch} = 41$ with $\beta = 0$ and a SMF with $\alpha = 0.22\,\text{dB/km}$.

By analyzing figures 3.17 (a) and (b), it can be stated that for a span length of 50 km, the differences in the NLI estimates between the asymptotic and IGN models never exceed about 0.3 dB for all the channel spacings considered. Above 65 km, the maximum differences in NLI power estimates between these two models decrease to about 0.2 dB. From both figures 3.17 (a) and (b), it can also be seen that the estimates of equation (3.11) are closer to the IGN-model estimates between around 75 km and 100 km for $\Delta f = 33.6\,\text{GHz}$, between about 65 km and 75 km for $\Delta f = 50\,\text{GHz}$ and between around 65 km and 85 km for $\Delta f = 100\,\text{GHz}$. For spans less than 45 km long, equation (3.11) should not be used, since it is not accurate for spans with losses below 10 dB [17]. For $N_s = 5$, the GN-model no longer provides the same NLI power estimates as the IGN-model, as evidenced in figure 3.17 (b). This figure also shows that the NLI power estimated using the GN-model decrease with the span length, stabilizing at about 38 dB for $\Delta f = 33.6\,\text{GHz}$, at 36.6 dB for $\Delta f = 50\,\text{GHz}$ and at about 34.7 dB for $\Delta f = 100\,\text{GHz}$.

The performance of the models up to the C-band limit is now investigated. To conduct this study, the NLI power values will be displayed as a function of the C-band occupancy ratio

$\epsilon_{\text{occupancy}}$, previously defined by equation (3.13). Figure 3.18 illustrates the normalized NLI power η_{NLI} as the C-band occupancy increases. One SMF span with a length of 100 km and three channel spacings are taken into account: 33.6 GHz (blue lines), 50 GHz (orange lines) and 100 GHz (yellow lines). The number of channels goes from 21 to the number of channels that fills the entire C-band for each channel spacing. The center frequency of the WDM signal is 193.7 THz, due to the 5 THz bandwidth considered for the C-band [40], [44]. A frequency resolution of 25 MHz is chosen to perform this study, owing to the fact that it provides accurate NLI power estimation independently of the C-band occupancy. The solid lines correspond to the asymptotic GN-model, while the dash-dotted lines and circles correspond to the GN-model for, respectively, $\beta = 0$ and $\beta = 0.1$.

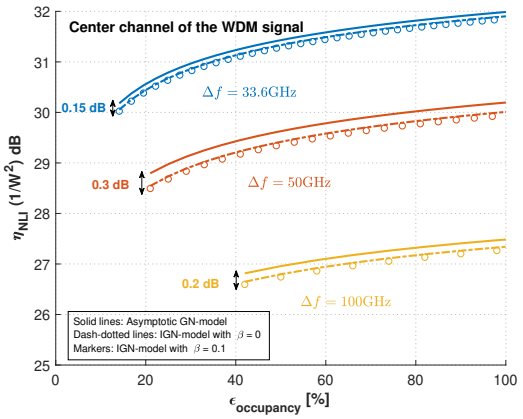

(a) Normalized NLI power η_{NLI} for the center channel of the WDM signal.

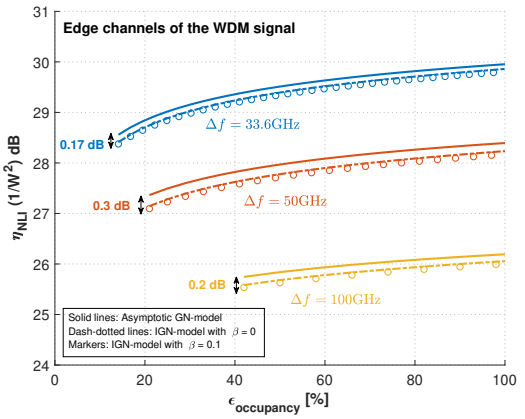

(b) Normalized NLI power η_{NLI} for the edge channels of the WDM signal.

Figure 3.18. Normalized NLI power η_{NLI} as a function of the C-band occupancy, for one span of SMF with $L_s = 100$ km and $\alpha = 0.22$ dB/km. The C-band occupancy is given by equation (3.13).

Considering the case of $\beta = 0.1$, the η_{NLI} results displayed in figure 3.18 show that, as the C-band occupancy grows, the discrepancy in NLI power predictions between the asymptotic GN-model and the GN-model is always around 0.2 dB for $\Delta f = 33.6$ GHz, about 0.3 dB for $\Delta f = 50$ GHz and about 0.2 dB for $\Delta f = 100$ GHz, independently of considering the center channel or the edge channels. Hence, it can be concluded that the asymptotic GN-model overestimation of the NLI power is independent of the C-band occupancy. As expected, figure 3.18 also reveals that the NLI power increases as the channel spacing decreases and the number of channels increases, due to the higher levels of XCI. The difference between the results with $\beta = 0$ and $\beta = 0.1$ never reaches 0.1 dB, which indicates that the asymptotic GN-model can be an appealing option for estimating the NLI in typical optical communication systems that have a roll-off below 0.1 [38].

As already mentioned, in this chapter, a C-band bandwidth of approximately 5 THz is assumed [8], [38], [40]. Thus, there are several frequencies where the WDM transmission system can be centered. The last study of this section focuses on analyzing the influence of the center frequency of the WDM signal on the asymptotic and GN models estimates. Figure 3.19 illustrates the η_{NLI} variation with the central frequency of the WDM signal, for $N_{ch} = 41$, $\beta = 0.02$ and $\Delta f = 50\,\text{GHz}$ (purple lines) and $N_{ch} = 9$, $\beta = 0.02$ and $\Delta f = 33.6\,\text{GHz}$ (green lines). The results are depicted for one SMF span with 100 km and for the GN/IGN model (dash-dotted lines) and asymptotic GN-model (solid lines).

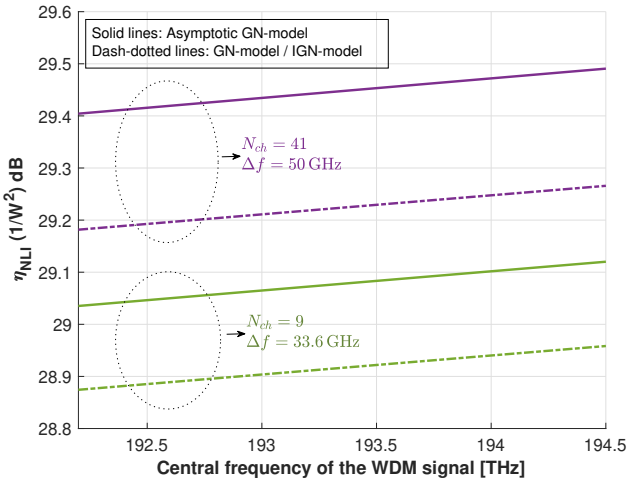

Figure 3.19. η_{NLI} as a function of the center frequency of the WDM system, for $\beta = 0.02$, $L_s = 100\,\text{km}$ and $\alpha = 0.22\,\text{dB/km}$.

Figure 3.19 shows that the estimates of both models increase only about 0.1 dB for higher center frequencies of the WDM signal. From this figure, it can also be concluded that both the asymptotic and GN models show the same behavior as the center frequency of the WDM signal increases, independently of the system configuration studied. Notice that the case where the C-band is fully occupied is not represented in figure 3.19, due to the center frequency of 193.7 THz being the only valid one in order to not exceed the C-band limits. For this frequency and with $N_{ch} = 99$ and $\Delta f = 50\,\text{GHz}$, the normalized NLI power η_{NLI} is equal to about 30 dB.

3.4. Conclusion

In this chapter, the original coherent GN-model and its variants have been studied.

The asymptotic GN-model was successfully implemented and it was concluded that equation (3.8) is more accurate than equations (3.2) and (3.9), since it is the one that least overestimates the NLI for the transmission systems considered. It was inferred that the NZDSF is the most affected

by the NLI and that the NLI power estimates are greater as the number of WDM channels increases and spacing decreases.

The GN and IGN models have been also analyzed. It was concluded that both models were correctly implemented for different system configurations and that the frequency resolution, i.e., the number of frequency components inside the WDM signal bandwidth, plays a crucial role to accurately perform the numerical integration involved in these models. It was inferred that due to the phased-array factor included in the GNRF, the GN-model is more time-consuming and requires a higher frequency resolution than the IGN-model, when considering more than one span. For instance, for a system with $N_{ch} = 41$, $\Delta f = 50$ GHz, $R_{s,m} = 32$ GBaud and $N_s = 20$ and by setting a threshold accuracy of 0.1 dB, it was discovered that the GN-model requires a frequency resolution of about 7 MHz and it takes 3 hours to compute the NLI PSD on a single frequency, while the IGN-model requires a minimum frequency resolution of 140 MHz and only takes 11 seconds of computation. Given this, it is concluded that the IGN-model is more advantageous because, besides being much less time-consuming, it leads to more accurate NLI estimates after several fiber spans [11], [17].

For the system configuration studied, it was found that the maximum difference in NLI power estimates between the asymptotic and IGN models is only about 0.3 dB, for transmission links with span lengths greater than 50 km. By analyzing the NLI estimates of each model up to the C-band limit and considering a roll-off factor equal to 0.1, it was concluded that the maximum overestimation of the NLI power by the asymptotic GN-model relative to the more accurate IGN-model is approximately 0.3 dB for $\Delta f = 50$ GHz. Furthermore, it can also be inferred that the difference in NLI power estimates between the asymptotic and IGN models is approximately constant as the C-band occupancy increases. Thus, the results of this work indicate that the asymptotic GN-model can represent an appealing and practical modeling solution for a network environment operating in the C-band. For transmission systems that require higher NLI accuracy estimates, the use of the IGN-model is recommended.

CHAPTER 4

Generalized Gaussian noise model

4.1. Introduction

In this chapter, the GGN-model is studied and its performance to predict the NLI in a C+L transmission system is evaluated. First, in section 4.2, the GGN-model equations are presented and their physical meaning is explained. In section 4.3, the equations in hyperbolic coordinates of the GN and GGN models are presented and a study regarding the computation time of the GN-model is exhibited. In section 4.4, the implementation of the GGN-model is confirmed through comparison with literature results. Finally, in section 4.5, the OSNR is assessed in an optical network scenario operating in the C+L band, using several of the GN models studied in this work.

The GN models previously studied provide a rapid and efficient solution to predict the NLI in transmission systems that operate over the entire C-band [8], [10], [11], [38]. In the C+L band, in addition to the nonlinear Kerr effect, the SRS should also be taken into account. The SRS is a nonlinear process that causes the transference of power from high to low frequency components within the same WDM signal [15], [19], [31]. The GGN-model was developed in order to estimate the NLI in the C+L transmission systems, where the joint effect of the NLI and SRS must be properly evaluated [15], [19], [31]. In this chapter, the analytical GGN-model proposed in [15] is implemented as well as its closed formula approximation presented in [16].

4.2. Equations and physical meaning

In C+L band optical systems, the SRS leads to an amplification of the power of the low frequency components of the WDM signal at the expense of the power of high frequency components. This power transfer is described mathematically by the signal power profile $\rho(z, f)$, which can be determined by numerically solving a set of coupled differential equations (see, for example, equation (6) of [15]). By solving numerically these differential equations, a GGN-model that takes into account the frequency dependent attenuation, the SRS and Raman amplification systems can be obtained [15], [19]. However, by using the triangular approximation of the Raman gain spectrum up to 15 THz and considering that the variation of the attenuation coefficient in

the C+L band is negligible, the normalized signal power profile can be calculated analytically by [15]:

$$\rho(z,f) = \frac{P_{tot}e^{-\alpha z - P_{tot}C_r L_{eff} f}}{\int_{-\infty}^{\infty} G_{WDM}(\nu)e^{-P_{tot}C_r L_{eff}\nu}\, d\nu} \tag{4.1}$$

where P_{tot} is the total optical launch power of the WDM signal and C_r is the Raman gain slope. The denominator of equation (4.1) represents mathematically the spectral distribution of the WDM signal power [15]. Using the signal power profile provided by equation (4.1) and considering a homogeneous transmission link, where each span has identical signal power profiles, the analytical GGN-model can be written as [15], [16]:

$$\begin{aligned} G_{NLI}(f) = \frac{16}{27}\gamma^2 \int_{-\infty}^{\infty} df_1 \int_{-\infty}^{\infty} df_2\, G_{WDM}(f_1)\, G_{WDM}(f_2)\, G_{WDM}(f_1+f_2-f) \\ \cdot \left| \int_0^{L_s} \rho(\zeta, f_1+f_2-f) e^{j\phi(f_1,f_2,f,\zeta)}\, d\zeta \right|^2 \end{aligned} \tag{4.2}$$

where $\phi = -4\pi^2(f_1 - f)(f_2 - f)\left[\beta_2 + \pi\beta_3(f_1+f_2)\right]\zeta$, in which β_3 is the group velocity dispersion slope. It is important to remark that equation (4.2) considers that NLI accumulates incoherently. For a coherent accumulation, the phased-array factor provided by equation (3.16) must be inserted in equation (4.2). The different power gains or losses that each frequency component experiences due to the SRS are taken into account by equation (4.1), making it possible to estimate the NLI in C+L band systems using equation (4.2) [15].

Although the GGN-model analytical equation (4.2) provides an accurate modeling solution for the C+L band transmission systems [15], [16], it involves performing numerically a triple integration, making the process of estimating the PSD of NLI more complex and time-consuming. For physical layer aware network optimization and to predict the performance in a network scenario, a simpler and a much less time-consuming model is more appropriate. On this basis, a GGN-model closed formula has been proposed [16].

As previously mentioned, in coherent UT systems, the NLI can essentially be divided in two contributions: XCI and SCI. This assumption allows to write the total normalized NLI power of a given transmission link as [16]:

$$\eta_{NLI}^{link}(f_m) \approx \sum_{j=1}^{N_s} \left[\frac{P_{m,j}}{P_{m,1}}\right]^2 \left[\eta_{\text{SCI},j}(f_m) N_s^{\epsilon} + \eta_{\text{XCI},j}(f_m)\right] \tag{4.3}$$

where $P_{m,j}$ is the power of the m-th channel launched in the j-th span, $P_{m,1}$ is the power of the m-th channel launched in the first span, $\eta_{\text{SCI}}(f_m)$ and $\eta_{\text{XCI}}(f_m)$ are the normalized NLI power

of the SCI and XCI contributions, respectively. The parameter ϵ is the coherence factor, which represents how the NLI accumulates along the link. For non-Nyquist-WDM systems with more than one span, the coherence factor ϵ can be written as [8]:

$$\epsilon = \frac{3}{10} \cdot \ln\left(1 + \frac{6}{L_s} \frac{L_{eff,a}}{\operatorname{asinh}\left(\frac{\pi^2}{2}|\beta_2| L_{eff,a} B_m^2 [N_{ch}^2]^{\frac{B_m}{\Delta f}}\right)}\right) \tag{4.4}$$

By using equation (4.4) in the closed-form GGN-model, it is assumed that the SRS does not influence the coherence factor. However, the coherence factor ϵ is dependent on the signal power profile, and therefore, the SRS affects this factor and the evaluation of the NLI [15]. The accuracy error in NLI prediction resulting from this assumption is about 0.1 dB and 0.2 dB for a 10 THz WDM C+L signal after 10 and 50 SMF spans, respectively [15], [16]. Notice that $\epsilon = 0$ means that the NLI only accumulates incoherently, while $\epsilon = 1$ means a NLI coherent accumulation over all link spans. As the WDM signal bandwidth increases, the value of ϵ decreases. For example, for the entire C-band and considering a Nyquist-WDM signal without power transfer between the outer channels, the coherence factor is only about 0.035 [8]. As can be observed from equation (4.3), this model considers that only the SCI contribution can accumulate coherently. In equation (4.3), the SCI and XCI contributions are defined, respectively, by [16]:

$$\eta_{\text{SCI}}(f_m) \approx \frac{4}{9} \frac{\gamma^2}{B_m^2} \frac{\pi}{\phi_m \overline{\alpha}(2\alpha + \overline{\alpha})} \cdot \left[\frac{T_m - \alpha^2}{\alpha} \operatorname{asinh}\left(\frac{\phi_m B_m^2}{\pi\alpha}\right) + \frac{A^2 - T_m}{A} \operatorname{asinh}\left(\frac{\phi_m B_m^2}{\pi A}\right)\right] \tag{4.5}$$

$$\eta_{\text{XCI}}(f_m) \approx \frac{32}{27} \sum_{k=1, k\neq m}^{N_{ch}} \left(\frac{P_k}{P_m}\right)^2 \frac{\gamma^2}{B_k \phi_{m,k} \overline{\alpha}(2\alpha + \overline{\alpha})} \cdot \left[\frac{T_k - \alpha^2}{\alpha} \operatorname{atan}\left(\frac{\phi_{m,k} B_m}{\alpha}\right) + \frac{A^2 - T_k}{A} \operatorname{atan}\left(\frac{\phi_{m,k} B_m}{A}\right)\right] \tag{4.6}$$

where $\phi_m = \frac{3}{2}\pi^2(\beta_2 + 2\pi\beta_3 f_m)$, $A = \alpha + \overline{\alpha}$, $T_m = (\alpha + \overline{\alpha} - P_{tot} C_r f_m)^2$ and $\phi_{m,k} = 2\pi^2(f_k - f_m)[\beta_2 + \pi\beta_3(f_m + f_k)]$. The SCI contribution $\eta_{\text{SCI}}(f_m)$ results from the nonlinear interaction of channel m on itself and the XCI contribution $\eta_{\text{XCI}}(f_m)$ represents the nonlinear interference resulting from all interferers (k) on channel m, such that $k \neq m$. The parameter $\overline{\alpha}$

is an adjustment parameter that can be used to generalize equation (4.3) to more specific cases [16], however, in this work, it is assumed that $\overline{\alpha} = \alpha$.

As in the GN-model, both the GGN-model in integral and closed formulas also consider the Gaussianity assumption, which leads to the overestimation of the NLI PSD when the WDM signal is not yet sufficiently dispersed [15], [16]. Considering a Gaussian modulation, i.e., that the WDM signal has a Gaussian distribution at the fiber input, and when comparing with the SSFM and integration results, the average deviation in NLI power regarding the GGN-model closed formula (4.3) is 0.2 dB for SMF spans in C+L band systems [16]. This loss of accuracy of the equation (4.3) compared to equation (4.2) is essentially due to the fact that the MCI contribution has been neglected and to a weak SRS assumption, as explained in chapter 2 [16].

4.3. GN and GGN models in hyperbolic coordinates

One of the main benefits of the GN-model is that a relatively fast evaluation of the NLI can be performed, when compared with the SSFM [8], [17]. Even so, as pointed out in the last chapter, the computation of the GN-model can be very time-consuming for WDM signals with very large bandwidths. The GGN-model requires an even higher computation time, since the C+L band (approximately 11.5 THz) must be considered. In addition, a triple integration must be solved, which demands the manipulation of very large matrices. For this reason, a change from cartesian to hyperbolic coordinates, in order to reduce the computation time of the GN models, is carried out in this section. The GN and GGN models formulations in hyperbolic coordinates are presented and a study regarding the calculation time of the GN-model is performed.

By making the change of integration variables for $f_1 = \nu_1 e^{\nu_2}$ and $f_2 = \nu_1 e^{-\nu_2}$, where $\nu_1 = \sqrt{f_1 f_2}$ and $\nu_2 = -\frac{1}{2}\ln(\frac{f_2}{f_1})$, the GN-model in hyperbolic coordinates can be written as equation (35) of [8]:

$$
\begin{aligned}
G_{NLI}(f) = \frac{32}{27}\gamma^2 L_{eff}^2 \int_0^{B_{\text{WDM}}} d\nu_1 \, \rho(\nu_1,0)\chi(\nu_1,0)|2\nu_1| \int_0^{\ln(\frac{B_{\text{WDM}}}{\nu_1})} d\nu_2 \, [G_{WDM}(\nu_1 e^{\nu_2}+f) \\
\cdot G_{WDM}(\nu_1 e^{-\nu_2}+f) G_{WDM}[2\nu_1 \cosh(\nu_2)+f] \\
+ G_{WDM}(\nu_1 e^{\nu_2}+f) G_{WDM}(-\nu_1 e^{-\nu_2}+f) G_{WDM}[2\nu_1 \sinh(\nu_2)+f] \\
+ G_{WDM}(-\nu_1 e^{\nu_2}+f) G_{WDM}(\nu_1 e^{-\nu_2}+f) G_{WDM}[-2\nu_1 \sinh(\nu_2)+f] \\
+ G_{WDM}(-\nu_1 e^{\nu_2}+f) G_{WDM}(-\nu_1 e^{-\nu_2}+f) G_{WDM}[-2\nu_1 \cosh(\nu_2)+f]] \quad (4.7)
\end{aligned}
$$

where ρ and χ are defined, respectively, by [8]:

$$\rho(\nu_1, 0) = \left| \frac{1 - e^{-\alpha L_s} e^{j4\pi^2 \beta_2 L_s \nu_1^2}}{\alpha - j4\pi^2 \beta_2 \nu_1^2} \right|^2 \cdot L_{eff}^{-2} \tag{4.8}$$

$$\rho(\nu_1, 0) = \frac{\sin^2(2N_s \pi^2 \nu_1^2 \beta_2 L_s)}{\sin^2(2\pi^2 \nu_1^2 \beta_2 L_s)} \tag{4.9}$$

Using equation (4.7) makes the GNRF numerical integration significantly faster, since it is possible to limit the integration range $[0, B_{WDM}]$ of the outer integral over ν_1, taking into account the decay of $\rho(\nu_1, 0)$ as ν_1 increases (see figure 7 of [8]). Additionally, as can be observed in equation (4.7), the inner integral only contains the spectrum of the WDM signal and in the outer integral, the parameters ρ and χ depend only on ν_1. A more elaborate explanation and a detailed derivation of the GN-model in hyperbolic coordinates can be found in [8].

Figure 4.1 shows the computation time of the GN-model in cartesian and hyperbolic coordinates as a function of the frequency resolution, for $N_s = 20$ and for the same system configuration of figure 3.11 (c) of chapter 3. Additionally, in order to understand which computing alternative is more time-consuming, two insets are also represented in figure 4.1, corresponding to the η_{NLI} estimates as a function of frequency resolutions between 27 MHz and 1000 MHz. The dashed and solid lines correspond, respectively, to the computation times and η_{NLI} estimates of the GN-model in cartesian (purple lines) and hyperbolic (red lines) coordinates.

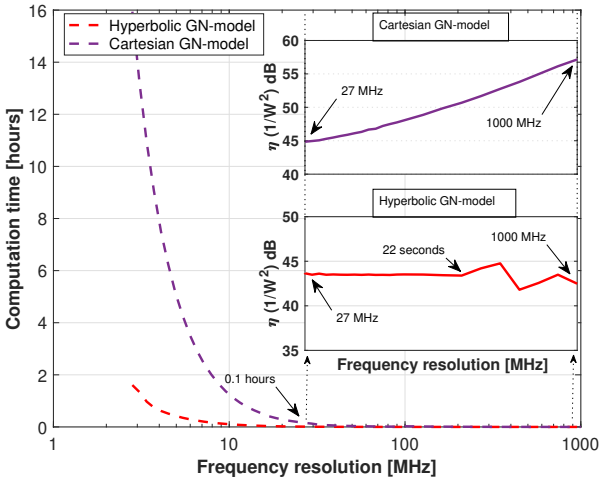

Figure 4.1. Computation time of the GN-model in cartesian and hyperbolic coordinates as a function of the frequency resolution. Using equation (4.7), the numerical integration is stopped when ρ becomes below -40 dB. The solid lines correspond to the η_{NLI} estimates using each method.

From figure 4.1, it can be seen that the GN-model in hyperbolic coordinates starts to provide stable normalized NLI power η_{NLI} estimates with a frequency resolution greater than 215 MHz, which corresponds to only 22 seconds of computation time. On the other hand, for the

same frequency resolution interval, the GN-model in cartesian coordinates delivers η_{NLI} estimates far from being stabilized. In fact, by inspecting figure 3.11 (c), it can be stated that the GN-model in cartesian coordinates requires a minimum frequency resolution of about 7 MHz, which is equivalent to 3 hours of computation time. Therefore, besides allowing the integration domain to be reduced, the use of hyperbolic coordinates decreases the need of high frequency resolutions, that translates into lower computation times when compared with the GN-model solved in cartesian coordinates.

Using the same change of integration variables, a GGN-model equation in hyperbolic coordinates can be obtained. A more detailed derivation of this formula can be found in the appendix A. The GGN-model formula in hyperbolic coordinates can be written as:

$$G_{NLI}(f) = \frac{32}{27}\gamma^2 \int_0^{B_{\text{WDM}}} d\nu_1 |2\nu_1| \int_0^{\ln(\frac{B_{\text{WDM}}}{\nu_1})} d\nu_2 \, [Q_1(\nu_1,\nu_2,f) + Q_2(\nu_1,\nu_2,f) + Q_3(\nu_1,\nu_2,f) + Q_4(\nu_1,\nu_2,f)] \quad (4.10)$$

where Q_1, Q_2, Q_3 and Q_4 correspond to the integrand functions in each quadrant of the integration domain and are, respectively, given by:

$$Q_1(\nu_1,\nu_2,f) = G_{WDM}(\nu_1 e^{\nu_2}+f) G_{WDM}(\nu_1 e^{-\nu_2}+f) G_{WDM}[2\nu_1 \cosh(\nu_2)+f] \cdot \left| \int_0^{L_s} d\zeta \frac{P_{tot} e^{-\alpha\zeta - P_{tot} C_r L_{eff}[2\nu_1\cosh(\nu_2)+f]}}{\int G_{WDM}(x) e^{-P_{tot} C_r L_{eff} x}\, dx} e^{-j4\pi^2\nu_1^2[\beta_2+\pi\beta_3(2\nu_1\cosh(\nu_2)+2f)]\zeta} \right|^2$$

$$Q_2(\nu_1,\nu_2,f) = G_{WDM}(-\nu_1 e^{\nu_2}+f) G_{WDM}(\nu_1 e^{-\nu_2}+f) G_{WDM}[-2\nu_1 \sinh(\nu_2)+f] \cdot \left| \int_0^{L_s} d\zeta \frac{P_{tot} e^{-\alpha\zeta - P_{tot} C_r L_{eff}[-2\nu_1\sinh(\nu_2)+f]}}{\int G_{WDM}(x) e^{-P_{tot} C_r L_{eff} x}\, dx} e^{j4\pi^2\nu_1^2[\beta_2+\pi\beta_3(-2\nu_1\sinh(\nu_2)+2f)]\zeta} \right|^2$$

$$Q_3(\nu_1,\nu_2,f) = G_{WDM}(-\nu_1 e^{\nu_2}+f) G_{WDM}(-\nu_1 e^{-\nu_2}+f) G_{WDM}[-2\nu_1 \cosh(\nu_2)+f] \cdot \left| \int_0^{L_s} d\zeta \frac{P_{tot} e^{-\alpha\zeta - P_{tot} C_r L_{eff}[-2\nu_1\cosh(\nu_2)+f]}}{\int G_{WDM}(x) e^{-P_{tot} C_r L_{eff} x}\, dx} e^{-j4\pi^2\nu_1^2[\beta_2+\pi\beta_3(-2\nu_1\cosh(\nu_2)+2f)]\zeta} \right|^2$$

$$Q_4(\nu_1,\nu_2,f) = G_{WDM}(\nu_1 e^{\nu_2}+f)G_{WDM}(-\nu_1 e^{-\nu_2}+f)G_{WDM}[2\nu_1\sinh(\nu_2)+f] \cdot \left| \int_0^{L_s} d\zeta \frac{P_{tot} e^{-\alpha\zeta - P_{tot}C_r L_{eff}[2\nu_1\sinh(\nu_2)+f]}}{\int G_{WDM}(x) e^{-P_{tot}C_r L_{eff} x}\, dx} e^{j4\pi^2\nu_1^2[\beta_2+\pi\beta_3(2\nu_1\sinh(\nu_2)+2f)]\zeta} \right|^2$$

Differently from the equation in hyperbolic coordinates of the GN-model, the inner integral in equation (4.10) depends on the FWM efficiency parameter and the signal power profile, which brings a disadvantage regarding its numerical integration. The main advantage of equation (4.10) is that the integration domain can be curtailed. In this work, a proper function that serves as a metric for limiting the integration domain of equation (4.10) has not been derived. Instead, the integration domain is limited until an accurate result for all frequencies is reached, i.e., when the value of the calculated NLI power starts to stabilize.

4.4. Implementation of the GGN-model for a point-to-point transmission scenario

In this section, the accuracy of the implementation of the GGN-model and its closed-form approximation is verified and their estimates compared in a point-to-point transmission scenario.

As already referred in section 4.2, the signal power profile $\rho(z,f)$ describes the loss or gain that each WDM frequency component undergoes during fiber propagation. Using equation (4.1), the power profile of each frequency of a WDM signal can be calculated analytically. In the following, the correct implementation of equation (4.1) is confirmed by comparing with the results illustrated in figure 1 of [15]. Figure 4.2 depicts the SRS gain (or loss) as a function of the center frequency of each channel of a 10 THz bandwidth WDM signal, for $N_s = 1$, with $L_s = 100\,\text{km}$ and several total WDM signal launch powers and power transfers. The results are presented for $C_r = 0.028\,\text{W}^{-1}\text{km}^{-1}\text{THz}^{-1}$ and $\alpha = 0.2\,\text{dB/km}$. The net power transfer between the edge channels of the WDM signal is denoted as $\Delta\rho(L)$ and can be obtained by summing the net SRS gains/losses of the highest and lowest frequencies of the WDM signal. The SRS gain G_{SRS} is calculated relative to a situation where there is no power transfer, i.e., $G_{\text{SRS}}[\text{dB}] = 10\log_{10}\left(\frac{\rho(z,f)_{(\Delta\rho(L)\neq 0)}}{\rho(z,f)_{(\Delta\rho(L)=0)}}\right)$.

By observing figure 4.2, it can be seen that as the total launch power increases, the higher is the power transfer between the outer channels of the WDM signal. For instance, a $P_{tot} = 19\,\text{dBm}$ yields a power transfer of only 2 dB between the outer channels, while a $P_{tot} = 28\,\text{dBm}$ yields a power transfer of 16.3 dB. For $P_{tot} = 5\,\text{dBm}$, the power transfer is less than 0.1 dB, being the SRS effect negligible. Using the parameters of modern fibers, the power transfer is usually greater than 4 dB for $B_{\text{WDM}} > 10.6\,\text{THz}$ [15]. The power transfer between the edge channels

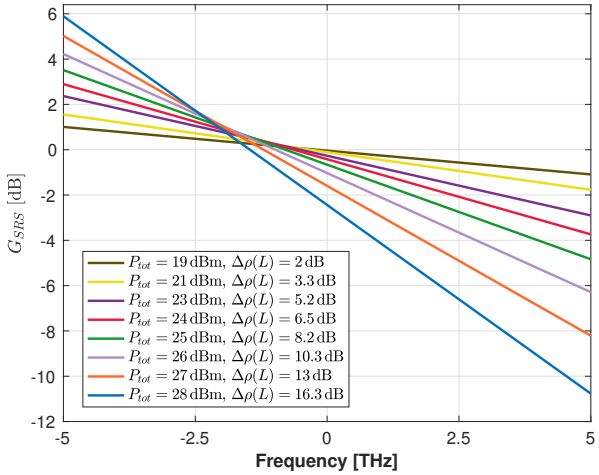

Figure 4.2. SRS gain for a 10 THz WDM signal over 100 km of fiber, for several total launch powers. $\Delta\rho(L)$ represents the power transfer between the edge channels due to SRS.

can be calculated theoretically using [15], [16]:

$$\Delta\rho(z)\,[\text{dB}] = 4.3 \cdot P_{tot} C_r L_{eff} B_{\text{WDM}} \tag{4.11}$$

Due to the similarity of figure 4.2 with figure 1 of [15], it can be stated that the implementation of the signal power profile, provided by the analytical equation (4.1), is correct. According to [15], a $P_{tot} = 28$ dBm leads to a maximum difference of only 0.18 dB between the results obtained using the analytical equation (4.1) and those obtained by solving numerically the differential equations that allow obtaining more accurately the signal power profile due to SRS. This indicates that equation (4.1) provides sufficiently accurate estimates of the signal power profile for any frequency component of any given WDM signal [15], [16].

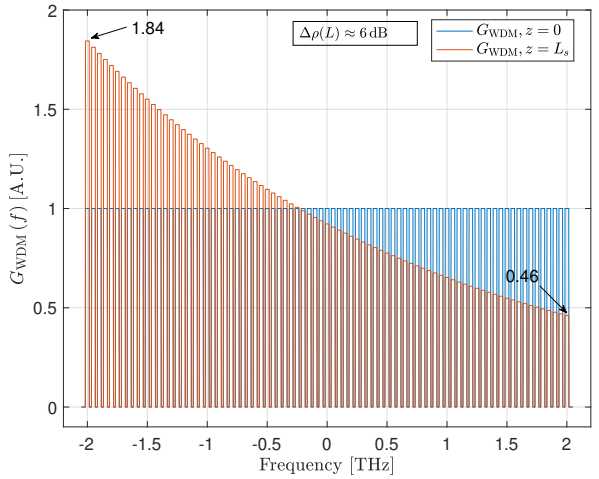

Figure 4.3. G_{WDM} as a function of frequency, for $z = 0$ and $z = L_s$.

The impact of the frequencies power gains/losses due to the SRS can be seen in figure 4.3, where the normalized PSD of an uniform WDM signal G_{WDM} at the input ($z = 0$) and at the end ($z = L_s$) of a span is depicted. The spectrum of each WDM channel is rectangular with a SRRC shape. A WDM signal with $N_{ch} = 81$, $\Delta f = 50\,\text{GHz}$ and $P_m = -1.1\,\text{dBm}$ is considered. To achieve a power transfer of $\Delta\rho(L) = 6\,\text{dB}$, an unrealistic $C_r = 0.28\,\text{W}^{-1}\text{km}^{-1}\text{THz}^{-1}$ is considered.

By analyzing figure 4.3, it becomes more clearer the impact that the SRS has on the WDM signal during fiber propagation. For $z = L_s$, the higher and lower frequencies components have a lower and higher G_{WDM} than for $z = 0$, respectively, due to the SRS that leads to a power transfer of about 6 dB from higher to lower frequency components. Notice that this power transfer can be extracted from figure 4.3 by calculating the ratio between the maximum and minimum WDM signal PSD, i.e., $\Delta\rho(L) = 10\log_{10}\left(\frac{1.84}{0.46}\right) \approx 6\,\text{dB}$. The G_{WDM} differences between $z = 0$ and $z > 0$ are even more pronounced as $\Delta\rho(L)$ increases. In this work, it is assumed that the power transfer due to the SRS is exactly compensated after every span. For that purpose, it is considered that all optical amplifiers of the link have gain equalization (achieved using gain flattening filters) [15], [16], [32].

In the following, the correct implementation of the GGN-model and its closed approximation is verified. This verification is performed by comparing the results obtained from the Matlab implementation of equations (4.3) and (4.10) with the results shown, respectively, in figures 5 and 6 of [16] and figure 2 of [15].

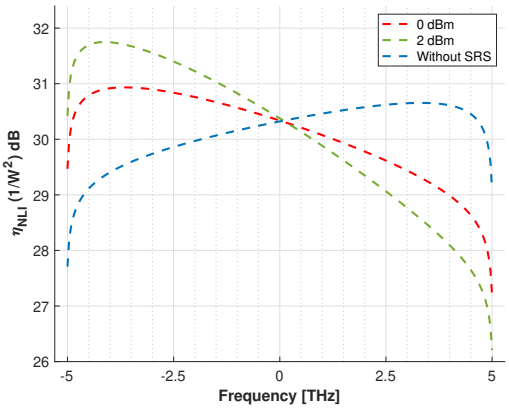

(a) η_{NLI} for $N_s = 1$ and several channel launch powers.

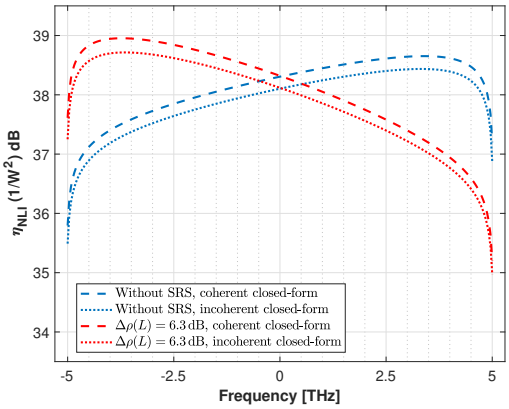

(b) η_{NLI} for $N_s = 6$ and $P_m = 0\,\text{dBm}$, for a coherent and incoherent assumption.

Figure 4.4. Normalized NLI power η_{NLI} as a function of channels center frequencies of the WDM signal. Equation (4.3) is used to obtain the η_{NLI} estimates. Homogeneous links and an uniform WDM signal are considered.

In figure 4.4, the parameter η_{NLI} is represented as a function of the center frequency of each WDM channel. The GGN-model closed equation (4.3) is used to obtain the normalized NLI power and the WDM system parameters considered are the following: $N_{ch} = 251$, $\Delta f = 40.005\,\text{GHz}$, $B_m = 40.004\,\text{GHz}$, $R_{s,m} = 40\,\text{GBaud}$, $\beta = 0.01$, $C_r = 0.028\,\text{W}^{-1}\text{km}^{-1}\text{THz}^{-1}$, $D = 17\,\text{ps/nm/km}$ and the dispersion slope $S_r = 0.067\,\text{ps/nm}^2\text{/km}$. In figure 4.4 (a), the η_{NLI} estimates are illustrated for $N_s = 1$ and for transmission scenarios without SRS ($C_r = 0\,\text{W}^{-1}\text{km}^{-1}\text{THz}^{-1}$) and with channel launch powers of 0 dBm and 2 dBm, corresponding to power transfers of $\Delta\rho(L) = 6.3\,\text{dB}$ and $\Delta\rho(L) = 10.3\,\text{dB}$, respectively. In figure 4.4 (b), the η_{NLI} estimates are depicted for $N_s = 6$, using equation (4.3) assuming a coherent NLI accumulation ($\epsilon \approx 0.14$) and an incoherent NLI accumulation ($\epsilon = 0$), represented by the dashed and dotted lines, respectively. Uniform WDM signals and homogeneous transmission links are considered in figure 4.4.

For the situation with SRS, as can be observed in figure 4.4 (a), the low frequency components of the WDM signal exhibit a higher normalized NLI power η_{NLI}, resulting from the power transfer from the high frequency components, and will suffer a higher impact of the NLI on the performance. As can be inferred from figure 4.2 and equation (4.11), as the total signal launch power increases, the greater is the power transfer between the frequencies of the WDM signal. The maximum η_{NLI} difference between the outer channels is about 4.2 dB and 2.3 dB for $P_m = 2\,\text{dBm}$ and $P_m = 0\,\text{dBm}$, respectively. In the situation without SRS, i.e., without power transfer, the normalized NLI power is tilted due to the higher order GVD term β_3, which makes the low frequency components to experience a higher level of dispersion, leading to a lower NLI [15], [16]. Figure 4.4 (b) shows that assuming a coherent accumulation ($\epsilon \neq 0$) of SCI results in higher η_{NLI} estimates relative to assuming an incoherent accumulation. According to [16], the average η_{NLI} difference between the estimates of the GGN-model in integral and closed forms is about 0.1 dB and 0.2 dB without and with SRS, respectively. The results presented in figure 4.4 (a) and (b) correspond to the η_{NLI} values outlined in figures 5 and 6 of [16], respectively. The very good agreement with [16] allows concluding that the implementation of the GGN-model closed-formula provided by equation (4.3) is correct.

Figure 4.5 depicts the normalized NLI power as a function of the frequencies of a WDM signal, with the following system parameters: $N_{ch} = 101$, $\Delta f = 10.001\,\text{GHz}$, $S_r = 0\,\text{ps/nm}^2\text{/km}$ and $R_{s,m} = 10\,\text{GBaud}$. Since the WDM signal bandwidth is only about 1 THz, in order to produce a considerable power transfer between the outer channels, a $C_r = 0.28\,\text{W}^{-1}\text{km}^{-1}\text{THz}^{-1}$ is used. Notice that this value of Raman gain slope is unrealistic, since for modern fiber parameters

a $C_r \approx 0.008\,\mathrm{W^{-1}km^{-1}THz^{-1}}$ is usually adopted [15]. The remaining WDM system parameters are the same as the ones used to obtain the results presented in figure 4.4. The GGN-model provided by the equation (4.10) is represented by the solid lines and the GGN-model closed formula (4.3) corresponds to the dashed lines.

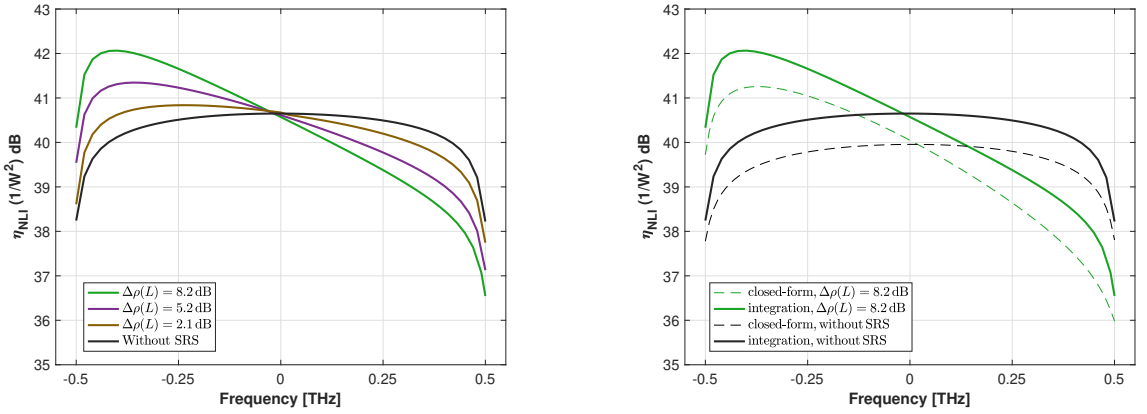

(a) η_{NLI} calculated by integration using equation (4.10).

(b) η_{NLI} calculated using equations (4.10) and (4.3).

Figure 4.5. η_{NLI} as a function of the frequency of a WDM signal with $B_{WDM} = 1$ THz, for $N_s = 1$ and several $\Delta\rho(L)$.

From analysis of figure 4.5, it can be concluded once again that the lower frequency components exhibit a higher η_{NLI} that increases as the power transfer increases. The η_{NLI} estimates by the closed-form are at most about 0.7 dB and 0.8 dB lower without SRS and with $\Delta\rho(L) = 8.2$ dB, respectively, than the estimates obtained using numerical integration of equation (4.10). In the center channel, the difference is about 0.7 dB and 0.5 dB, as can be seen in figure 4.5 (b). Due to the good agreement between figure 4.5 (a) and figure 2 of [15], it can be concluded that the numerical integration of the GGN-model using hyperbolic coordinates, given by equation (4.10), is well implemented.

Figure 4.6 shows the variation of the normalized NLI power η_{NLI}, with (a) the percentage of WDM signal bandwidth B_{WDM} integrated in equation (4.10) and (b) the number of ζ samples considered for integration. Three WDM channels are considered: lowest frequency channel, center channel and highest frequency channel. The system parameters are the same as the ones used in figure 4.5, being $\Delta\rho(L) \approx 8.2$ dB. Additionally, in figure 4.6 (a), the computation time of the GGN-model equation (4.10) is also represented as a function of the bandwidth B_{WDM} integrated. A frequency resolution of 100 MHz is used, as it provides sufficiently accurate η_{NLI} estimates for this signal bandwidth. The error associated with this frequency resolution is less than 0.1 dB.

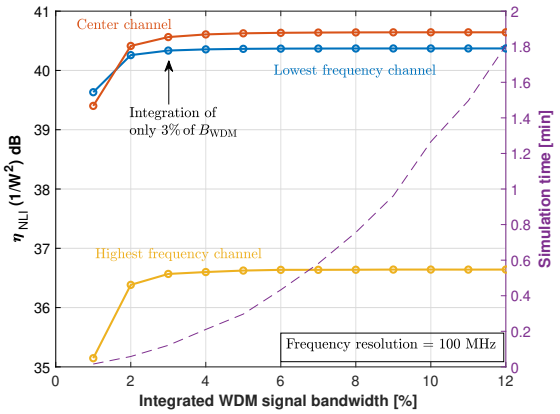

(a) Variation of the η_{NLI} and computation time with the B_{WDM} integrated.

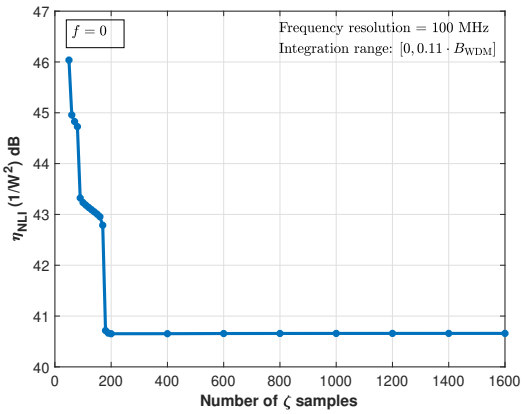

(b) Variation of the η_{NLI} with the number of ζ samples.

Figure 4.6. η_{NLI} as a function of the number of ζ samples and integrated WDM signal bandwidth obtained using equation (4.10).

From figure 4.6 (a), it can be concluded that the η_{NLI} obtained from equation (4.10) starts to stabilize with only 3% of the signal bandwidth integrated for all WDM frequencies considered, being the corresponding computation time only about 7 seconds. In contrast, it takes about several hours to obtain an accurate η_{NLI} using the GGN-model in cartesian coordinates. This considerable computation time is because, besides the integration domain cannot be reduced, it is also necessary a greater frequency resolution and number of ζ samples than in the case of the hyperbolic coordinates to obtain the same accuracy of the normalized NLI power. As can be seen in figure 4.6 (b), for this system configuration, the η_{NLI} stabilizes with about 200 samples of ζ. On the other hand, solving the GGN-model in cartesian coordinates requires at least 3000 samples of ζ. It is important to state that these computation times are presented to provide an insight into the differences in efficiency between the GGN-model calculation methods and depend on several factors, such as the implementation and computer resources. A computer with an Intel Core i7-6700K 4 GHz processor and 16 GB of RAM memory is used to perform the calculations.

4.5. Performance analysis in a mesh optical network scenario

In this section, the performance of the GGN-model is evaluated in an optical network transmission scenario in order to estimate the OSNR at the receiver input, and thereby, estimate the system performance. Since an optical network analysis must be efficient and quickly performed [10], [16], only the GGN-model in closed-form is used. This model is a good solution for quantifying the NLI impact in a mesh optical network scenario, as proven in [16]. By default, the

coherent accumulation of SCI in GGN-model formula is considered ($\epsilon \neq 0$). First, the implementation of the network transmission scenario considered in this section is confirmed by comparison with the results presented in figures 8 (a) and (b) of [16]. Then, several network parameters are varied in order to quantify their impact on the NLI, and consequently, on the OSNR.

4.5.1. Impact of system parameters variation on NLI estimation

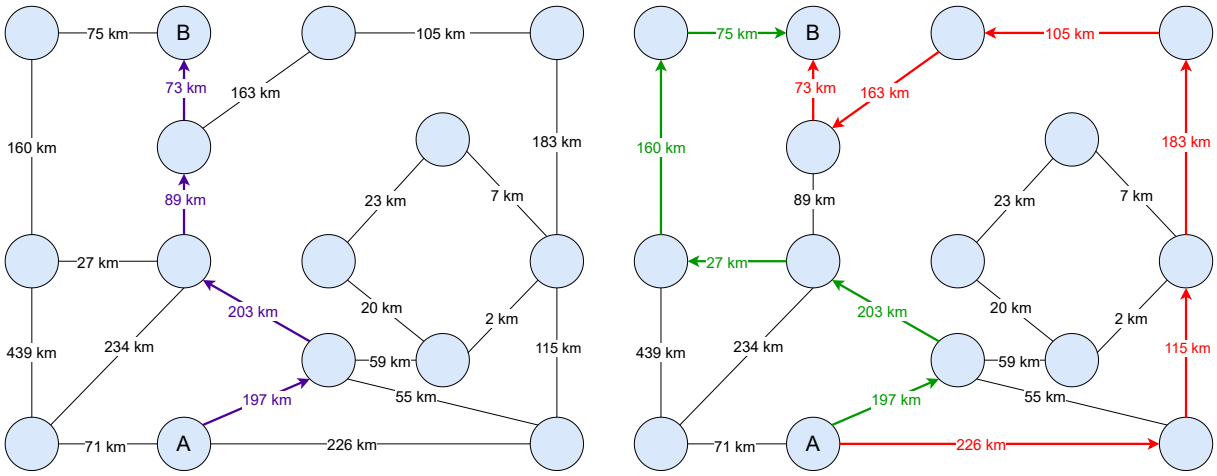

(a) Lightpath between node A and B used for confirmation of the optical network simulator.

(b) Two possible lightpaths between node A and B analyzed in this section.

Figure 4.7. A region from the BT topology of the United Kingdom core network (adapted from [16], [45]).

An optical network is composed by several nodes, known as reconfigurable optical add/drop multiplexers (ROADMs), where the WDM channels can be added, dropped or simply pass through the node (express channels) [46]. In this way, the WDM signal spectrum changes during the optical lightpath, resulting in different levels of NLI and accumulated signal dispersion along the network. Figure 4.7 depicts a region of the British Telecommunications (BT) topology of the United Kingdom core network [16], [45]. The lightpath between A and B used to test the accuracy of the optical network simulator is highlighted in purple in figure 4.7 (a). In figure 4.7 (b), two alternative lightpaths between nodes A and B are highlighted in red and green.

For the analysis of the lightpaths highlighted in figure 4.7, the WDM channels are classified in two categories: *channels under test* and *add/drop channels*. The channels under test (CUTs) correspond to the WDM wavelengths that are transmitted/expressed along the complete lightpath, i.e., from the first node to the last node of the lightpath without any add/drop occurring in those wavelengths. The add/drop channels are the wavelengths that can be added or dropped in any ROADM belonging to the considered lightpath [16]. For a given span of a lightpath, the

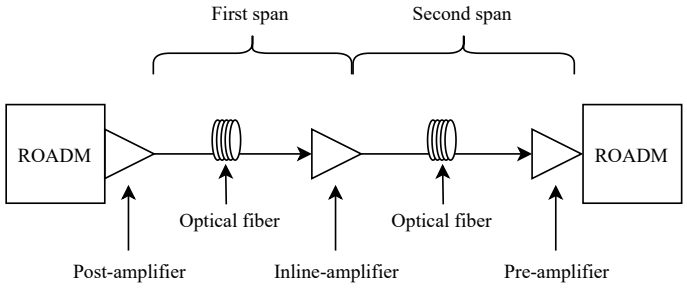

Figure 4.8. Placement of the ROADMs and optical amplifiers in a link.

ratio between the number of channels transmitted in that span and the total number of WDM channels is defined as network utilization, which is denoted as ϵ_{span}. Consequently, for the entire lightpath, the network utilization $\epsilon_{\text{network}}$ is the average of the network utilizations of all spans. Thus, $\epsilon_{\text{network}}$ can be written as:

$$\epsilon_{\text{network}} = \frac{1}{N_s}\sum_{j=1}^{N_s}\epsilon_{\text{span},j} = \frac{1}{N_s}\sum_{j=1}^{N_s}\frac{N_{ch,j}}{N_{ch}} \tag{4.12}$$

where $N_{ch,j}$ is the number of WDM channels transmitted in the j-th span.

In each ROADM, the simulator determines which add/drop channels are added or dropped randomly using an uniform distribution. The number of add/drop channels $N_{\text{add/drop}}$ that are added/dropped depends on the required $\epsilon_{\text{network}}$. The launch power of the added channels has a random offset of ± 1 dB relative to the launch power of the channels under test [16]. The added channels always maintain the same power until they are dropped, i.e., for a given lightpath, the power of a channel only changes if it is added to the optical network a second time. This last assumption differs from the optical transmission scenario considered in [16], where the add/drop channels that have not been dropped may not maintain the same power they have in the previous span. A perfect compensation of the losses of the transmission system is assumed in this work. Therefore, pre and post amplifiers are used in order to compensate the losses of the fiber spans and ROADMs, respectively. Additionally, due to the gain limitations of optical amplifiers, in the spans with a length longer than 110 km, inline-amplifiers are also used, as illustrated in figure 4.8. Notice that, to use equation (4.3) in the described network scenario, only the channel launch power at the input of each span needs to be changed. For instance, for a given span, if the algorithm determines that a specific channel has been dropped, the channel launch power is set to zero. Otherwise, the launch power of the added channels in that span is set randomly, as previously stated. It is important to remark that the launch powers of the CUTs are maintained along the complete lightpath. The data structure that contains the channel launch powers at the input of each span, which are used in GGN-model equation (4.3), is designated

as *power configuration*. This procedure is described in the flowchart represented in figure 4.9. The parameter $\epsilon_{req,j}$ is defined as the required network utilization in the j-th span, N_{CUT} is the number of channels under test and P_{CUT} is the reference power of the CUT.

A randomly generated normalized PSD of a WDM signal transmitted in the network scenario previously described is shown in figure 4.10, for $z = 0$ and $z = L_s$, for a network utilization $\epsilon_{\text{network}} = 80\%$ and the same system configuration of figure 4.3. Notice that due to the network utilization being less than 100%, the power transfer obtained is lower than in figure 4.3.

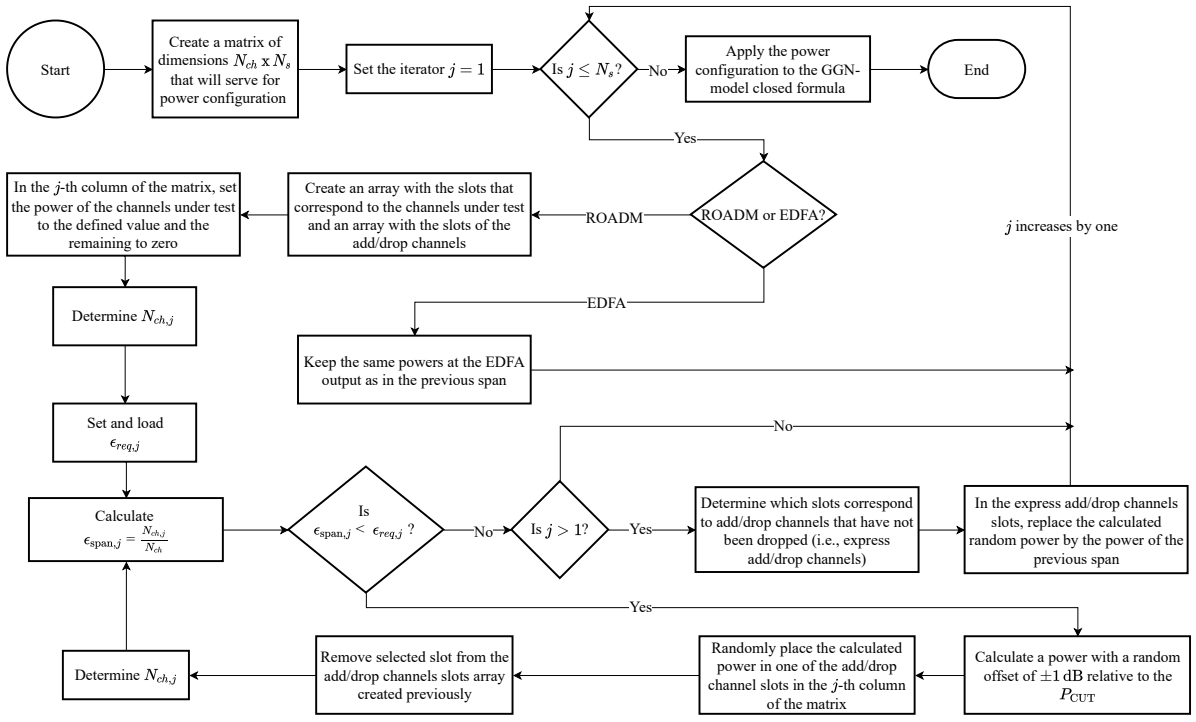

Figure 4.9. Flowchart describing the implementation of the power configuration and how to apply it to GGN-model equation (4.3).

By observing figure 4.10, it can be seen that, as a consequence of the considered network scenario with $\epsilon_{\text{network}} = 80\%$, there is the presence of unused channel slots and oscillations in the WDM signal amplitudes. In the case of $z = 0$, these oscillations are only a result of the WDM channels having a power with a random offset of ± 1 dB relative to P_{CUT}. For $z = L_s$, i.e., after the WDM signal has been transmitted through the optical fiber, the G_{WDM} variation is tilted due to the impact of the SRS, which causes the power transfer from higher to lower frequency components.

To validate the network simulator, the WDM system parameters are the same as the ones considered to obtain figure 4.4, being $P_{\text{CUT}} = 0$ dBm. The number of channels under test is $N_{\text{CUT}} = 51$ and the number of add/drop channels is $N_{\text{add/drop}} = 200$. The normalized NLI power η_{NLI} of the channels under test is shown in figure 4.11 as a function of their frequencies.

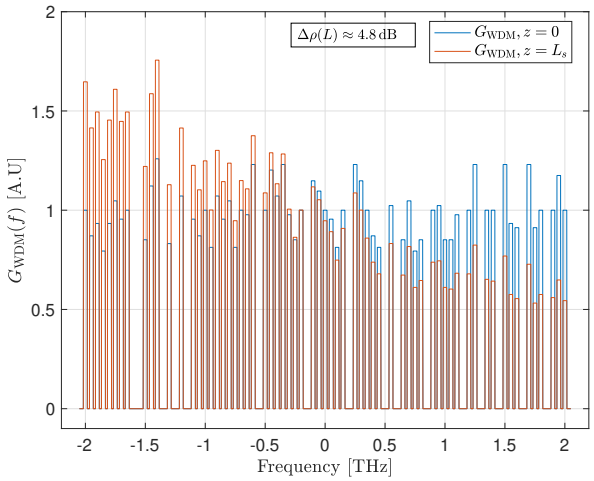

Figure 4.10. G_{WDM} in a network transmission scenario as a function of frequency, for $z = 0$ and $z = L_s$.

In figures 4.11 (a) and (b), the η_{NLI} is depicted, respectively, for $\epsilon_{\mathrm{network}} = 80\%$ and $\epsilon_{\mathrm{network}} = 90\%$ and for two different power configurations: the launch powers of the add/drop channels considered in [16] (solid line) and launch powers obtained in this work (markers). The location of the CUTs is the same in both power configurations. In order to validate the network simulator according to the assumptions made in [16], the express add/drop channels may not maintain the same power as the previous span. The lightpath considered is highlighted in purple in figure 4.7 and the configuration of each span with the ROADMs and EDFAs placement can be seen in figure 7 of [16].

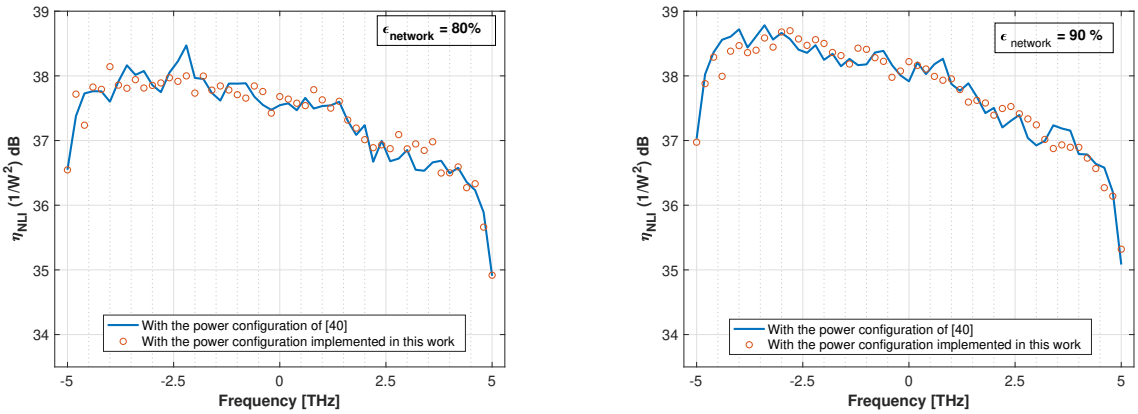

(a) η_{NLI} for $\epsilon_{\mathrm{network}} = 80\%$.

(b) η_{NLI} for $\epsilon_{\mathrm{network}} = 90\%$.

Figure 4.11. Channels under test η_{NLI} as a function of the frequency. Equation (4.3) is used to calculate the η_{NLI}. The lightpath considered is marked in purple in figure 4.7.

One of the consequences of considering an optical network scenario with a dynamic (random) add/drop channels variation is the oscillatory behavior of the parameter η_{NLI}, each time

the lightpath is simulated, as can be verified in figure 4.11. Since the network utilization is higher in figure 4.11 (b), there is more overall average in terms of η_{NLI} calculation, which leads to less oscillatory behavior than in figure 4.11 (a) with lower network utilization [16]. Due to the fact that the channel launch power of each added channel is set randomly, the η_{NLI} estimates resulting from the power configuration implemented in this work do not have exactly the same value as the estimates obtained with the power configuration used in [16]. However, the results presented in figures 4.11 (a) and (b) show the same η_{NLI} behavior as the one shown in figure 8 of [16], which proves that the network simulator is correctly implemented.

In figure 4.12 (a), the CUTs average η_{NLI} and some simulated realizations of η_{NLI} are represented as a function of the WDM signal frequency, for $\epsilon_{\text{network}} = 100\%$. In addition to the average η_{NLI}, in figure 4.12 (b), the standard deviation of the normalized NLI power $\sigma_{\eta_{NLI}}$ is also represented through the error bars. For the purpose of analyzing the η_{NLI} standard deviation for several $\epsilon_{\text{network}}$, the standard deviation $\sigma_{\eta_{NLI}}$ of the CUTs is depicted in figures 4.12 (c) and (d) as a function of their center frequencies and network utilization $\epsilon_{\text{network}}$, respectively. In order to obtain stabilized η_{NLI} and $\sigma_{\eta_{NLI}}$ distributions, 200 and 30000 simulations of the η_{NLI} estimates were performed, respectively. The system configuration is the same as the one used in figure 4.11.

Figure 4.12 shows that, in general, the $\sigma_{\eta_{NLI}}$ increases as the WDM signal frequency decreases, meaning that there is a greater oscillatory behavior of η_{NLI} in the lower frequency channels, when compared with higher frequency channels. First, by analyzing figure 4.12 (a) when $\epsilon_{\text{network}} = 100\%$, it can be seen that, with the exception of the edge channels, the η_{NLI} estimates are more dispersed around the average in the lower frequency components. This can be confirmed by the higher $\sigma_{\eta_{NLI}}$ found in these frequencies, illustrated through the error bars in figure 4.12 (b). As $\epsilon_{\text{network}}$ decreases, the difference between the $\sigma_{\eta_{NLI}}$ of the higher and lower frequencies is also reduced, as can be seen in figure 4.12 (c). For $\epsilon_{\text{network}} = 40\%$, the $\sigma_{\eta_{NLI}}$ remains approximately constant along the WDM signal bandwidth, once again with the exception for the edge channels. This variation of the $\sigma_{\eta_{NLI}}$ with the network utilization can be seen with more detail in figure 4.12 (d). It can be concluded that as the WDM signal frequency decreases, the peak of the η_{NLI} standard deviation happens for higher network utilizations. For instance, the channel with the frequency equal to 5 THz has the highest NLI deviation when $\epsilon_{\text{network}} = 55\%$, decreasing thereafter for higher $\epsilon_{\text{network}}$. The increase of the $\sigma_{\eta_{NLI}}$ as frequency decreases can be related with the growth of the SRS effect and the consequent higher power transfer.

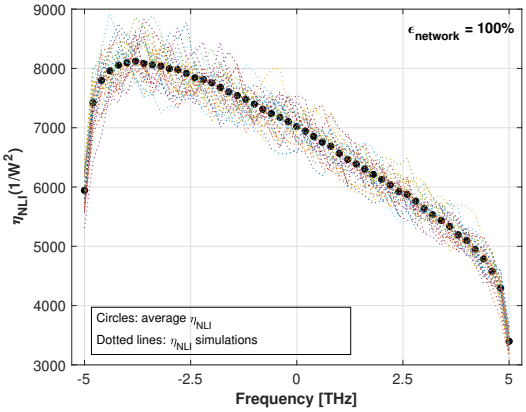

(a) Several simulated realizations of η_{NLI} and its average as a function of the frequency.

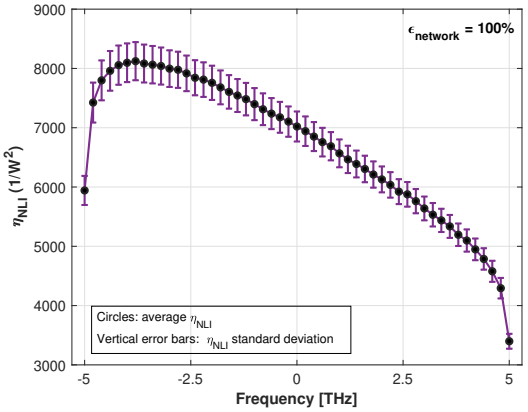

(b) Average η_{NLI} and $\sigma_{\eta_{NLI}}$ as a function of the frequency.

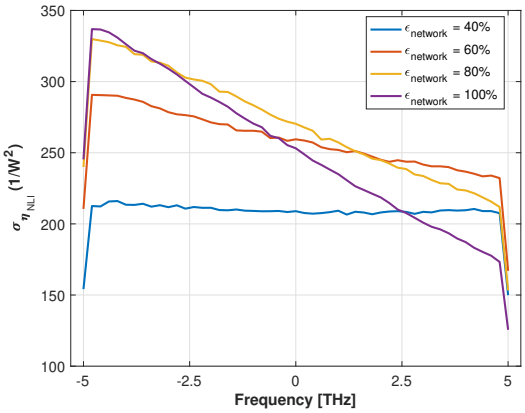

(c) $\sigma_{\eta_{NLI}}$ as a function of the frequency.

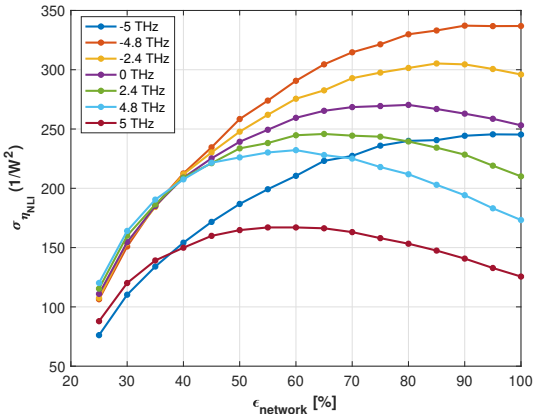

(d) $\sigma_{\eta_{NLI}}$ as a function of the $\epsilon_{\text{network}}$.

Figure 4.12. Standard deviation of the η_{NLI} of the CUTs in the considered network scenario. The lightpath used is marked in purple in figure 4.7.

With figure 4.13, the goal is to analyze how the network utilization $\epsilon_{\text{network}}$ impacts the normalized NLI power η_{NLI} estimation and how the choice of the lightpath affects the NLI estimation. In figure 4.13 (a), an average value for η_{NLI} is represented for the following network utilizations: 20%, 40%, 60%, 80% and 100%. Notice that $\epsilon_{\text{network}} = 20\%$ corresponds to a situation where only the CUTs are transmitted across the optical network and $\epsilon_{\text{network}} = 100\%$ means that both channels under test and add/drop channels are transmitted along the complete lightpath. In the inset of figure 4.13 (a), the dotted lines correspond to some of the simulations performed to stabilize the η_{NLI} distribution for $\epsilon_{\text{network}} = 100\%$. In figure 4.13 (b), the power transfer between the outer channels $\Delta\rho(L)$ is depicted as a function of $\epsilon_{\text{network}}$, for several CUTs launch powers P_{CUT}. Lastly, in figure 4.13 (c), the same study of figure 4.13 (a) is repeated, but this time considering the lightpaths highlighted in red and green in figure 4.7 (b).

From figure 4.13 (a), it stands out that the average η_{NLI}, obtained after several simulations of the lightpath in figure 4.7 (a) and corresponding η_{NLI} estimation, exhibits a stable behavior

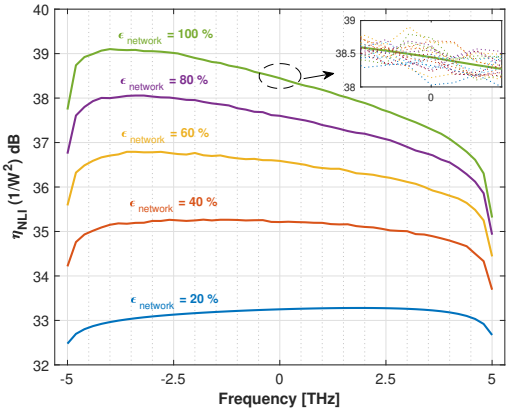

(a) Average η_{NLI} as a function of frequency, for several $\epsilon_{\text{network}}$.

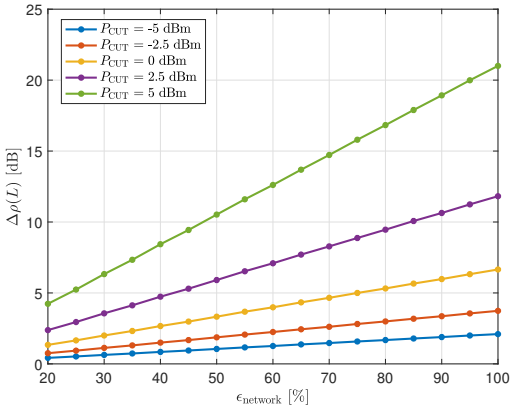

(b) $\Delta\rho(L)$ variation with $\epsilon_{\text{network}}$, for several P_{CUT}.

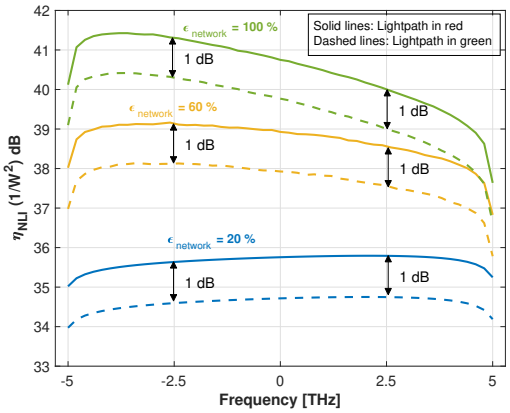

(c) Average η_{NLI} as a function of frequency, for several $\epsilon_{\text{network}}$.

Figure 4.13. Variation of the average η_{NLI} and $\Delta\rho(L)$ with the $\epsilon_{\text{network}}$. The dotted-lines in the inset in (a) correspond to several η_{NLI} simulations. In (a) and (b), the lightpath considered is marked in purple in figure 4.7 (a). In (c), the lightpaths considered are marked in red and green in figure 4.7 (b).

after 200 simulations for all the network utilizations considered. In general, figure 4.13 (a) indicates that η_{NLI} increases as the network utilization increases, which is a fact that can be explained by the increasing SCI and XCI as the number of transmitted WDM channels in the optical network grows. Notice that the tilt on the left side of the spectrum of the η_{NLI} distribution is more noticeable from $\epsilon_{\text{network}} \geq 60\%$, where the average occupancy of the C+L band starts to increase. The increase of η_{NLI} with the network utilization can be further explained through the higher power transfer between outer channels as $\epsilon_{\text{network}}$ grows, as evidenced in figure 4.13 (b). This figure also shows that $\Delta\rho(L)$ varies more sharply as the P_{CUT} increases due to the higher impact of SRS. For $P_{\text{CUT}} = 5$ dBm, there is a power transfer increase of about 17 dB from $\epsilon_{\text{network}} = 20\%$ to $\epsilon_{\text{network}} = 100\%$, while for $P_{\text{CUT}} = 0$ dBm, the power transfer varies only about 5.3 dB. Regarding figure 4.13 (c), it can be concluded that the red lightpath is more impacted by

the NLI than the green lightpath, being the η_{NLI} difference constant at about 1 dB for the entire signal bandwidth. This difference in η_{NLI} is due to the fact that the red lightpath is composed by one more span than the green lightpath. When also taking into account the η_{NLI} estimates of the purple lightpath represented in figure 4.13 (a), it is concluded that the η_{NLI} differences remain constant at about 1 dB and 2 dB relative to the green and red lightpaths, respectively. Since the difference between the η_{NLI} estimates remains approximately constant, the slope of the NLI variation does not seem to vary much with the lightpath chosen. This suggests that the lightpath length does not have much impact on the power transfer between outer channels that causes the NLI tilting.

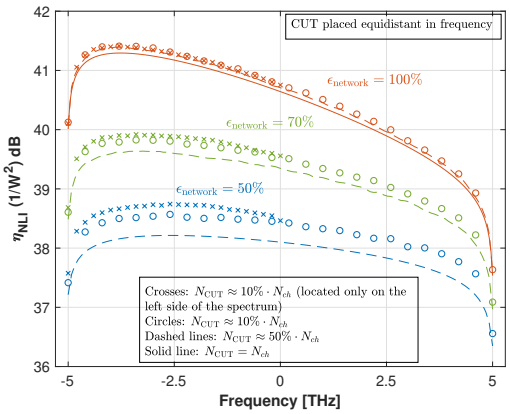

(a) Average η_{NLI} considering that CUTs are placed equidistant in frequency.

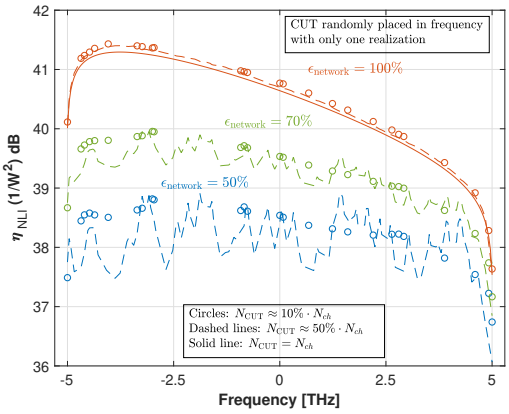

(b) Average η_{NLI} considering that CUTs are placed randomly in frequency. The random selection of the CUTs is only performed once for each network utilization.

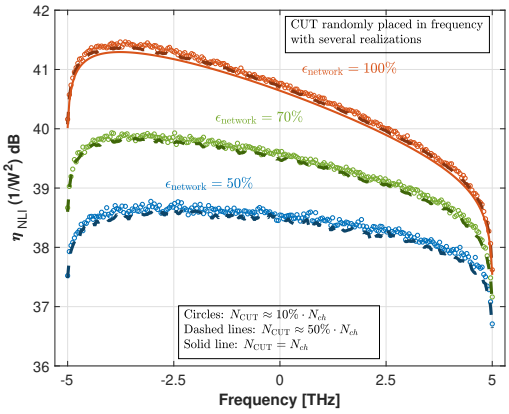

(c) Average η_{NLI} considering that CUTs are placed randomly in frequency. For each network utilization, the selection of the CUTs is performed randomly in each of the 300 simulations.

Figure 4.14. Average η_{NLI} of the CUTs as a function of frequency, for several N_{CUT} and $\epsilon_{\text{network}}$. The lightpath considered is marked in red in figure 4.7.

Figure 4.14 shows the normalized NLI power η_{NLI} as a function of the WDM signal frequency, for 10%, 50% and 100% of channels under test and for network utilizations of 50%,

70% and 100%, considering the total number of WDM channels $N_{ch} = 251$. The remaining WDM system parameters are the same as the ones considered in figure 4.13 and the lightpath analyzed is the one highlighted in red in figure 4.7. The circles and the dashed and solid lines correspond, respectively, to 10%, 50% and 100% of CUTs. The crosses represent the results when there are 10% of the CUTs and when they are only located on the left side of the spectrum. To obtain an average value for η_{NLI}, 300 simulations are considered. As in the previous studies, in figure 4.14 (a), the CUTs are placed equidistant in frequency over the entire WDM signal bandwidth. In figure 4.14 (b), for each different case of N_{CUT}, the CUTs are maintained when the network utilization varies. In figure 4.14 (c), for each network utilization, the CUTs are randomly chosen in each simulation performed to estimate the η_{NLI} parameter, being different from simulation to simulation.

Figure 4.14 (a) indicates that, as the number of CUTs is reduced, there is an increase of the η_{NLI} across the entire WDM signal bandwidth and that this increase is more pronounced for low network utilizations. For $\epsilon_{\text{network}} = 50\%$, the normalized NLI power difference is about 0.3 dB between the cases where $N_{\text{CUT}} = 10\% \cdot N_{ch}$ and $N_{\text{CUT}} = 50\% \cdot N_{ch}$. For $\epsilon_{\text{network}} = 70\%$ and $\epsilon_{\text{network}} = 100\%$, this difference decreases, respectively, to about 0.2 dB and 0.1 dB. When taking into account the case of $N_{\text{CUT}} = N_{ch}$, the difference is less than 0.1 dB and may be considered negligible. This behavior occurs, because to maintain the network utilization, as N_{CUT} decreases, there are more add/drop channels transmitted across the network, which leads to an increase of SCI and XCI. From this figure, it is also noticeable that the NLI is higher when the 10% of CUTs are only on the left side of the spectrum. This is due to the enhanced XCI, as the CUTs are closer in frequency.

As a consequence of randomly choosing the CUTs, in figure 4.14 (b), it can be seen that η_{NLI} shows a fluctuating behavior for $\epsilon_{\text{network}} < 100\%$. The highest η_{NLI} oscillation behavior occurs when $N_{\text{CUT}} = 50\% \cdot N_{ch}$ and $\epsilon_{\text{network}} = 50\%$ and very negligible oscillations occur when $\epsilon_{\text{network}} = 100\%$, independently of the N_{CUT} considered. Notice that for $N_{\text{CUT}} = N_{ch}$, it is insignificant how the CUTs are spaced in frequency, since there are no add/drop channels and the $\epsilon_{\text{network}}$ is 100%. From figure 4.14 (c), it is noted that, by generating the CUTs randomly in each simulation, there are more CUTs to calculate the average over the entire WDM spectrum, leading to a more stable η_{NLI} than in figure 4.14 (b). Additionally, it can also be concluded that, for each network utilization, the influence of the number of CUTs on the η_{NLI} parameter is very small, when compared to figures 4.14 (a) and (b).

4.5.2. Impact of system parameters variation on OSNR estimation

In the following, the optical network analysis is performed considering the lightpaths displayed in red and green in figure 4.7. The OSNR of these lightpaths is calculated and the impact of varying several optical network parameters is evaluated.

The NLI power estimated using the GN-model is typically used in the calculation of the OSNR [8], [17]. As explained in chapter 2, the GN-model assumes that the NLI can be processed as AGN, which permits to redefine the OSNR as [11]:

$$\text{OSNR}_m = \frac{P_m}{P_{ASE,tot} + P_{NLI,tot}} \tag{4.13}$$

where, for a given lightpath, P_m is the power of the channel under test at the Rx input, $P_{ASE,tot}$ is the total power of the ASE noise and $P_{NLI,tot}$ is the total NLI noise power arriving at the Rx input corresponding to channel m. The total NLI power $P_{NLI,tot}$ and the total ASE noise power $P_{ASE,tot}$ can, respectively, be written as:

$$P_{NLI,tot} = \eta_{NLI}^{link}(f_m) \cdot P_m^3 \tag{4.14}$$

$$P_{ASE,tot} = \sum_{i=1}^{N_{amp}} P_{ASE,i} \tag{4.15}$$

where $\eta_{NLI}^{link}(f_m)$ is provided by the GGN-model equation (4.3) and $P_{\text{ASE},i}$ is the ASE noise power introduced by the i-th optical amplifier (e.g., EDFA) of the optical path, being N_{amp} the total number of optical amplifiers placed along the lightpath. The ASE noise power for two polarizations introduced by each optical amplifier is given by [32]:

$$P_{ASE,i} = f_n(g_i - 1)h(f_m + \nu_c)R_{s,m} \tag{4.16}$$

where f_n is the noise figure, g_i is the gain of the i-th optical amplifier, h is the Planck constant and ν_c is the nominal optical frequency of the center channel. Notice that equation (4.16) assumes a noise bandwidth equal to the symbol rate.

The lightpaths highlighted in red and green in the network topology shown in figure 4.7 (b) that a channel under test experiences are represented in figures 4.15 (a) and (b). It is considered that the ROADMs architecture is Route and Select (R&S), so that the losses of the add/drop and express structures are 15 dB and 18 dB, respectively [47]. Since only the worst loss case is considered, the post-amplifiers after all ROADMs are designed with a gain of 18 dB. By default, the WDM system parameters considered are those presented in table 4.1. The SMF

parameters are given in table 3.1, being $\alpha = 0.22\,\mathrm{dB/km}$ and $S_r = 0.067\,\mathrm{ps/nm^2/km}$. All optical amplifiers considered in the lightpaths are EDFAs with dynamic gain equalization. Thus, besides the EDFAs compensate exactly the previous fiber losses and ROADM losses, they also compensate the power transfer in each span due to the SRS [32].

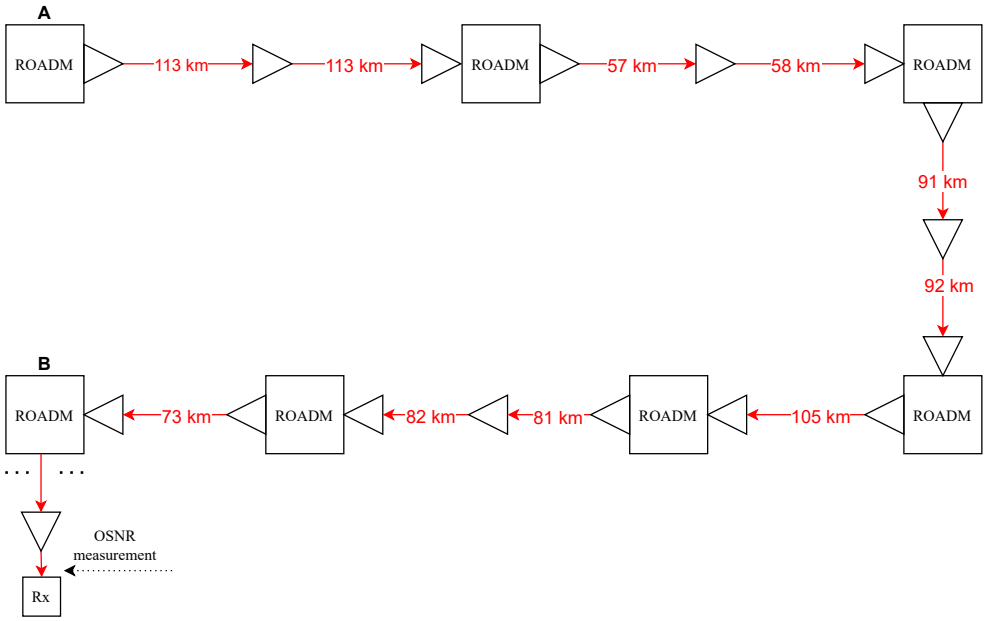

(a) Lightpath highlighted in red in figure 4.7 (b).

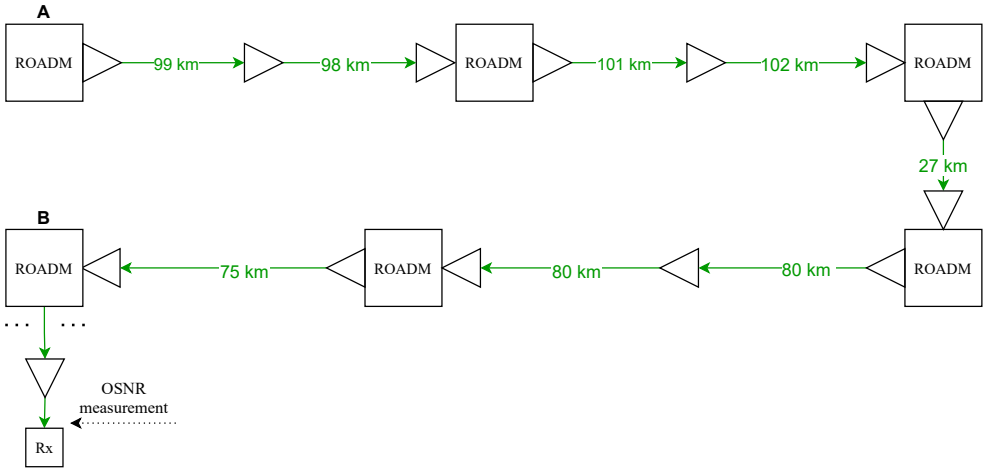

(b) Lightpath highlighted in green in figure 4.7 (b).

Figure 4.15. Possible arrangement of the ROADMs and EDFAs in the lightpaths analyzed.

In figure 4.16, the OSNR as function of the power transfer between the outer channels is depicted for $\epsilon_{\text{network}} = 90\%$ and for the channels allocated in the following frequencies: -5 THz, -2.5 THz, 0 THz, 2.5 THz and 5 THz. With this figure, it is aimed to show how the OSNR changes as $\Delta\rho(L)$ increases. To simulate this effect, the channel launch power P_m has been

System parameters	
N_{ch}	201
N_{CUT}	41 (20% $\cdot N_{ch}$)
$N_{\text{add/drop}}$	160
Δf [GHz]	50
R_s [GBaud]	32
B_m [GHz]	32
β	0
S_r [ps/nm^2/km]	0.067
C_r [W^{-1}km^{-1}THz^{-1}]	0.028
ROADMs architecture	R&S
EDFAs noise figure [dB]	5

Table 4.1. System parameters used by default for calculate the OSNR.

increased. The power transfer $\Delta\rho(L)$ is obtained by averaging the power transfers of all spans of the lightpath. The solid and dashed lines represent the red and green lightpaths of figures 4.15 (a) and (b), respectively.

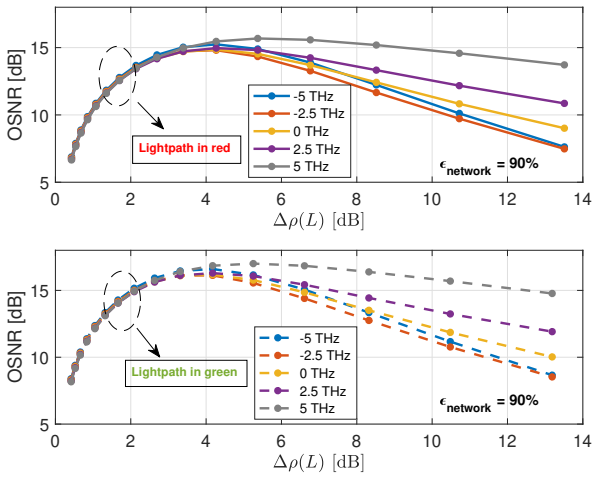

Figure 4.16. OSNR as a function of the power transfer between the outer channels $\Delta\rho(L)$, for the lightpaths introduced in figure 4.15.

The OSNR starts to grow with the increase of the power transfer, reaching the maximum between $\Delta\rho(L) \approx 3.5$ dB and $\Delta\rho(L) \approx 6$ dB. After reaching the maximum value, the OSNR decreases more smoothly for all signal frequencies, practically with a linear behavior. The previously described OSNR variation is explained by the levels of NLI in the link. In other words, first, the OSNR increases, since the ASE noise is the dominant contribution to the performance degradation, for low power transfers. When the NLI starts to have a significant contribution to the performance degradation, the OSNR variation is smoothed and reaches the maximum possible value. After this maximum, the NLI becomes the dominant contribution and starts to

degrade the system performance, leading to the decreasing OSNR observed in figure 4.16. From this figure, it can be concluded that, for the optimum situation, the maximum OSNR variation between the WDM channels is only about 0.7 dB. The maximum possible value for OSNR, also called the optimum OSNR, occurs when the NLI noise power is approximately half the ASE noise power [27]. It is important to note that this condition is an approximation, since in its derivation it was considered that the launch power distribution has no impact on η_{NLI}, which has been proven not to be strictly correct [48].

The OSNR as a function of the WDM signal frequencies is shown in figures 4.17 (a) and (b) for several network utilizations. In figure 4.17 (a), the power transfers of the green and red lightpaths correspond, respectively, to about 4.2 dB and 4.3 dB and in figure 4.17 (b) to about 13.2 dB and 13.5 dB, for $\epsilon_{\text{network}} = 90\%$. Notice that, according to figure 4.16, for $\epsilon_{\text{network}} = 90\%$, a power transfer of about 4 dB corresponds to an OSNR very close to the maximum and a power transfer of about 13 dB corresponds to the lowest OSNR. Additionally, the required OSNR to achieve a line bit error-rate (BER) of 10^{-2} is depicted using horizontal dash-dotted lines [49]. The solid and dashed lines in figure 4.17 represent the red and green lightpaths of figures 4.15 (a) and (b), respectively.

By examining figures 4.17 (a) and (b), in general, it can be concluded that the OSNR decreases as $\epsilon_{\text{network}}$ increases. This is a consequence of the increase of η_{NLI} with the $\epsilon_{\text{network}}$, as previously shown in figure 4.13. Also as an effect of the increase of the NLI power, it can be seen that as $\epsilon_{\text{network}}$ increases, the OSNR variation tends to tilt, with the higher frequency components of the WDM signal performing better than the lower frequency components. Due to the high value of power transfer $\Delta\rho(L) \approx 13.5\,\text{dB}$ used in figure 4.17 (b), the NLI tilt is much more sharper, which means that the lowest frequency channels in figure 4.17 (b) are much more impacted by the NLI. In fact, the OSNR of the highest WDM frequencies converge to the same value, which indicates that the ASE noise has become the only source of performance degradation. Consequently, the OSNR differences between the edge channels in figure 4.17 (b) are much higher than in the case of figure 4.17 (a), where $\Delta\rho(L) \approx 4.2\,\text{dB}$. For instance, while in figure 4.17 (a) there is an OSNR difference of only about 0.5 dB between the edge channels for $\epsilon_{\text{network}} = 90\%$, in figure 4.17 (b), this difference rises to about 6 dB. In figure 4.17 (a), the OSNR variation is approximately symmetric around $f = 0$ when $\epsilon_{\text{network}} = 50\%$, since the weight between the powers of the ASE noise and NLI is similar. For $\epsilon_{\text{network}} = 30\%$, the OSNR estimates are slightly tilted to the opposite direction, with the lower frequency components of the WDM signal showing a better performance, due to the higher impact of the ASE noise.

Regarding the discrepancy between the two lightpaths considered in figure 4.17, it is noticeable that the lightpath marked in green provides better OSNRs. This difference in performance can be explained by the length of both lightpaths and the number of spans that compose each one. While the red lightpath is composed by ten spans with a total length of 865 km, the green lightpath has eight spans with a total length of 662 km. This increase of two spans and of 223 km causes the ASE noise power to grow in the longest lightpath, due to the higher losses that must be compensated. Additionally, the increase by two spans in the red lightpath also leads to a higher NLI, as shown in figure 4.13 (c). Regarding the minimum OSNR required to obtain a BER of 10^{-2}, in figure 4.17 (a), the obtained OSNRs meet the minimum requirements, for QPSK and 16-QAM, independently of the lightpath and $\epsilon_{\text{network}}$ considered. For figure 4.17 (b), it can be concluded that the calculated OSNR complies with the requirements in the case of the QPSK modulation, with the exception for the red lightpath and $\epsilon_{\text{network}} = 90\%$. For a 16-QAM WDM signal, the required OSNR for a BER of 10^{-2} is only achieved considering the green lightpath and the highest frequency channels. Notice that the GGN-model closed formula considered in this work does not take into account the modulation format, and therefore, overestimates the NLI power leading to conservative OSNR estimates. In order to also take into consideration the modulation format, the GGN-model closed formula proposed in [36] should be used.

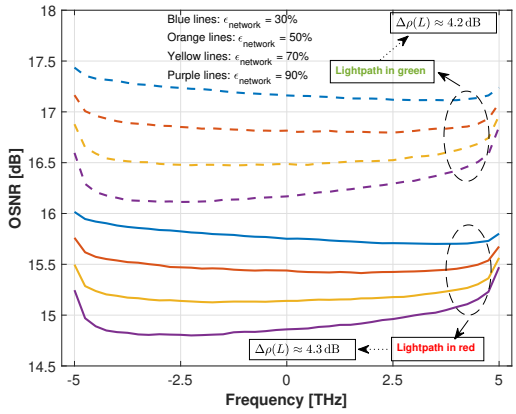

(a) OSNR for power transfers of 4.2 dB and 4.3 dB.

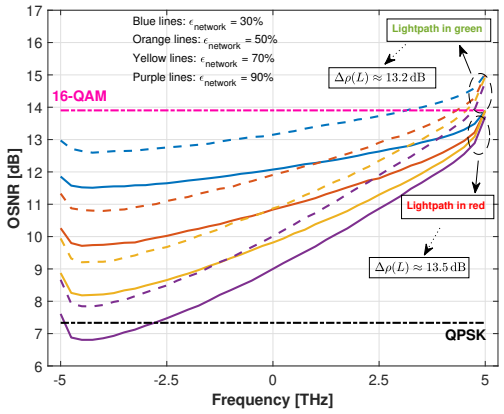

(b) OSNR for power transfers of 13.2 dB and 13.5 dB.

Figure 4.17. OSNR as a function of the frequency, for $\epsilon_{\text{network}}$ equal to 30%, 50%, 70% and 90% and for the lightpaths analyzed in figure 4.15. In (b), the required OSNR to obtain a BER of 10^{-2} for QPSK and 16-QAM modulations is also presented. The power of the CUTs is 0 dBm.

As seen previously in figure 4.16 for the case of $\epsilon_{\text{network}} = 90\%$, the OSNR reaches its maximum when the NLI begins to impact significantly the system performance. Figure 4.18 shows

the maximum OSNR (OSNR_{opt}) and the corresponding average power transfer ($\Delta\rho(L)_{opt}$) leading up to it as a function of the network utilization $\epsilon_{\text{network}}$, for the (a) red lightpath and the (b) green lightpath. The following WDM frequencies are considered: -5 THz, -2.5 THz, 0 THz, 2.5 THz and 5 THz. It is important to remark that due to the random patterns of the network scenario, an average value for $\Delta\rho(L)_{opt}$ is considered in figure 4.18.

As can be seen in both figures 4.18 (a) and (b), the maximum OSNR decreases with the increase of the $\epsilon_{\text{network}}$, for all frequencies considered. This happens because the NLI grows with the network utilization, as shown previously in figure 4.13. The channels with the lower OSNR_{opt} are allocated in -2.5, 0 and 2.5 THz. Additionally, it can be concluded that $\Delta\rho(L)_{opt}$ increases as the network utilization grows and that it varies with the WDM channel frequency. For $\epsilon_{\text{network}} = 20\%$, $\Delta\rho(L)_{opt}$ is approximately the same for all WDM frequencies considered. For $\epsilon_{\text{network}} > 20\%$, the WDM channel frequency with the highest $\Delta\rho(L)_{opt}$ is located at 5 THz, with the difference to the remaining channels getting larger as the network utilization increases. This can be explained by the fact that as the power transfer increases, the highest frequency channel has a higher power depletion, becoming less impacted by NLI. Thus, it can be concluded that, for the lightpaths considered and in an optimum situation, the maximum power transfer does not exceed about 6.4 dB. Notice that there is a limit to which the power transfer can be increased without impairing the overall system performance, as can be seen in figure 4.17 (b) when $\Delta\rho(L) \approx 13$ dB. From figure 4.18, it can also be concluded that $\Delta\rho(L)_{opt}$ is higher in the red lightpath. However, it seems to vary very slightly with the lightpath, being the maximum variation below about 0.5 dB.

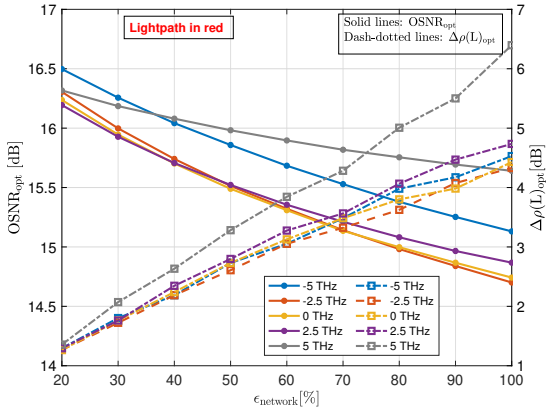

(a) OSNR_{opt} and $\Delta\rho(L)_{opt}$ for the red lightpath of figure 4.15 (a).

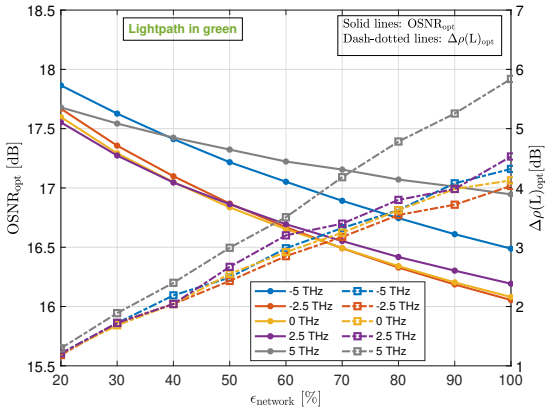

(b) OSNR_{opt} and $\Delta\rho(L)_{opt}$ for the green lightpath of figure 4.15 (b).

Figure 4.18. OSNR_{opt} and $\Delta\rho(L)_{opt}$ as a function of the network utilization, for the lightpaths represented in figure 4.15.

In the previous studies, a 10 THz WDM signal has been considered. The next results consist of analyzing the variation of the OSNR with the C+L band occupancy. Besides using the GGN-model closed formula, the maximum OSNR difference by using the asymptotic GN-model is also quantified. To carry out the next studies, the C-band occupancy ratio given by equation (3.13) is reformulated in order to also take into account the L-band. Thus, the C+L band occupancy ratio can be defined as:

$$\epsilon_{\text{occupancy}} = \frac{\Delta f N_{ch}}{B_{\text{C+L-band}}} \tag{4.17}$$

where $B_{\text{C+L-band}}$ is the C+L optical transmission bandwidth. The C+L band optical bandwidth is assumed to be about $B_{\text{C+L-band}} = 11.5\,\text{THz}$ (1530 nm - 1625 nm) [20].

Figure 4.19 shows the OSNR and $\Delta\rho(L)$ as a function of the C+L band occupancy, for (a) the lowest frequency WDM channel, (b) the center WDM channel and (c) the highest frequency WDM channel. Additionally, in figure 4.19 (d), the OSNR for the lowest frequency WDM channel is also depicted for $S_r = 0$, instead of only for $S_r = 0.067\,\text{ps/nm}^2\text{/km}$. The network utilization considered is 95% and the CUTs have a power equal to 0 dBm. This power leads to approximately the maximum OSNR in the center channel for the network utilization considered. The first, center and last WDM channels are assumed to be CUTs. Using an uniform distribution, the remaining CUTs are chosen randomly until the number of channels under test is 20% of the total number of WDM channels. The network models used to estimate the NLI are the following: asymptotic GN-model (lines with asterisks) and the two variants of the closed-form GGN-model, the coherent GGN-model (dashed lines) and the incoherent GGN-model (lines with circles). The division that marks the end of the C-band and the beginning of the L-band is highlighted by dashed black vertical lines. The OSNR and $\Delta\rho(L)$ results are represented, respectively, by lines and points. The estimates illustrated in blue and yellow correspond to $\Delta f = 50\,\text{GHz}$ and $\Delta f = 100\,\text{GHz}$, respectively.

For the center channel with the two channel spacings, the OSNR estimates using the asymptotic GN-model show a very good agreement with the ones obtained through the incoherent GGN-model for the entire C+L band. Due to the SCI coherent assumption and, consequently, higher NLI estimates, the coherent GGN-model provides lower OSNR results, with the maximum difference in the center channel being about 0.2 dB to the other GN models. For the lowest and highest WDM channel frequencies and $\Delta f = 100\,\text{GHz}$, the OSNR results from the asymptotic GN-model are also very similar to the OSNR results from the incoherent GN-model. For $\Delta f = 50\,\text{GHz}$, the OSNR difference between these two models is negligible below about

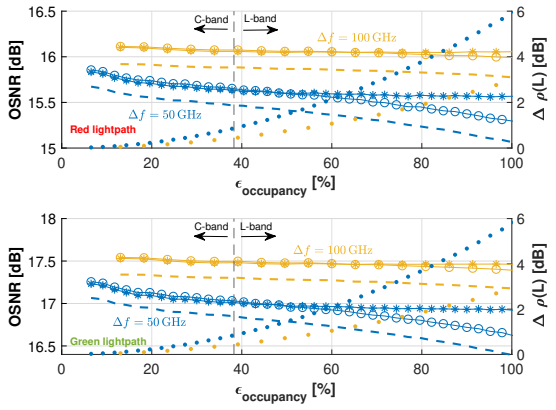

(a) OSNR for the lowest frequency channel.

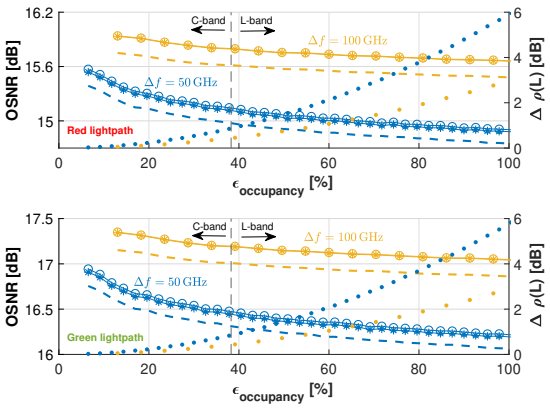

(b) OSNR for the center channel.

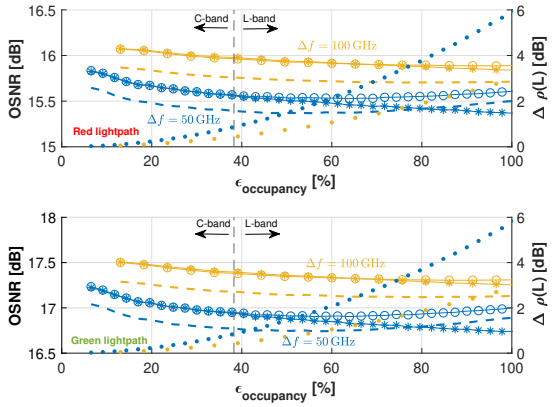

(c) OSNR for the highest frequency channel.

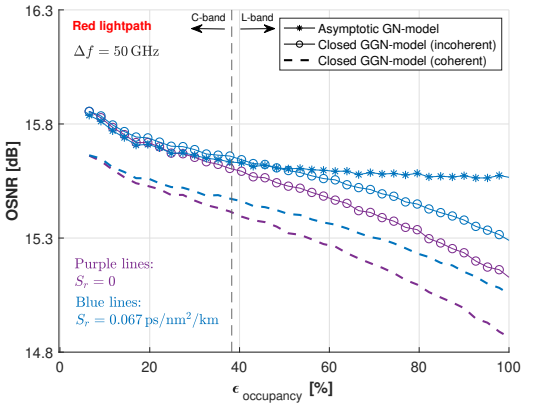

(d) OSNR for the lowest frequency channel, including results with $S_r = 0$.

Figure 4.19. OSNR as a function of the C+L band occupancy $\epsilon_{\text{occupancy}}$, for $\epsilon_{\text{network}} = 95\%$, $\Delta f = 50$ GHz and $\Delta f = 100$ GHz. Circles: closed GGN-model (incoherent). Dashed lines: closed GGN-model (coherent). Asterisks: asymptotic GN-model. Points: $\Delta\rho(L)$.

$\epsilon_{\text{occupancy}} = 70\%$, where $\Delta\rho(L) \approx 3.5$ dB. For $\epsilon_{\text{occupancy}} > 70\%$, the asymptotic GN-model delivers higher and lower OSNR results than the incoherent GGN-model for the lowest and highest WDM frequencies, respectively. The maximum difference between these models reaches about 0.3 dB when the C+L band is completely full and the average power transfer is approximately 6 dB. For this $\epsilon_{\text{occupancy}}$, the maximum OSNR discrepancy between the asymptotic GN-model and the coherent GGN-model is about 0.5 dB for $\Delta f = 50$ GHz in the lowest frequency channel and about 0.1 dB for both spacings in the highest frequency channel.

Considering also the OSNR estimates for $S_r = 0$, the maximum discrepancy between the asymptotic GN-model and incoherent and coherent GGN models increases to about 0.4 dB and 0.7 dB, respectively. The greater difference between the GN models estimates in relation to $S_r = 0.067\,\text{ps/nm}^2\text{/km}$ results from the lower dispersion in the lowest frequency channels

for $S_r = 0$. For $S_r = 0.067\,\text{ps/nm}^2\text{/km}$, the higher levels of dispersion produced counteract the NLI tilt due to the SRS effect. It should be noted that among the GN models covered, the coherent GGN-model is the one that provides η_{NLI} results closest to the SSFM [16]. The higher discrepancy in the OSNR results for $\Delta f = 50\,\text{GHz}$ is due to the higher $\Delta\rho(L)$. In other words, for the same $\epsilon_{\text{occupancy}}$, the WDM system with $\Delta f = 50\,\text{GHz}$ has twice the number of channels than for $\Delta f = 100\,\text{GHz}$, which leads to a higher NLI and lower OSNR. From figure 4.19, it can also be concluded that, as $\epsilon_{\text{occupancy}}$ increases, the OSNR differences between the GN models are approximately the same for both lightpaths.

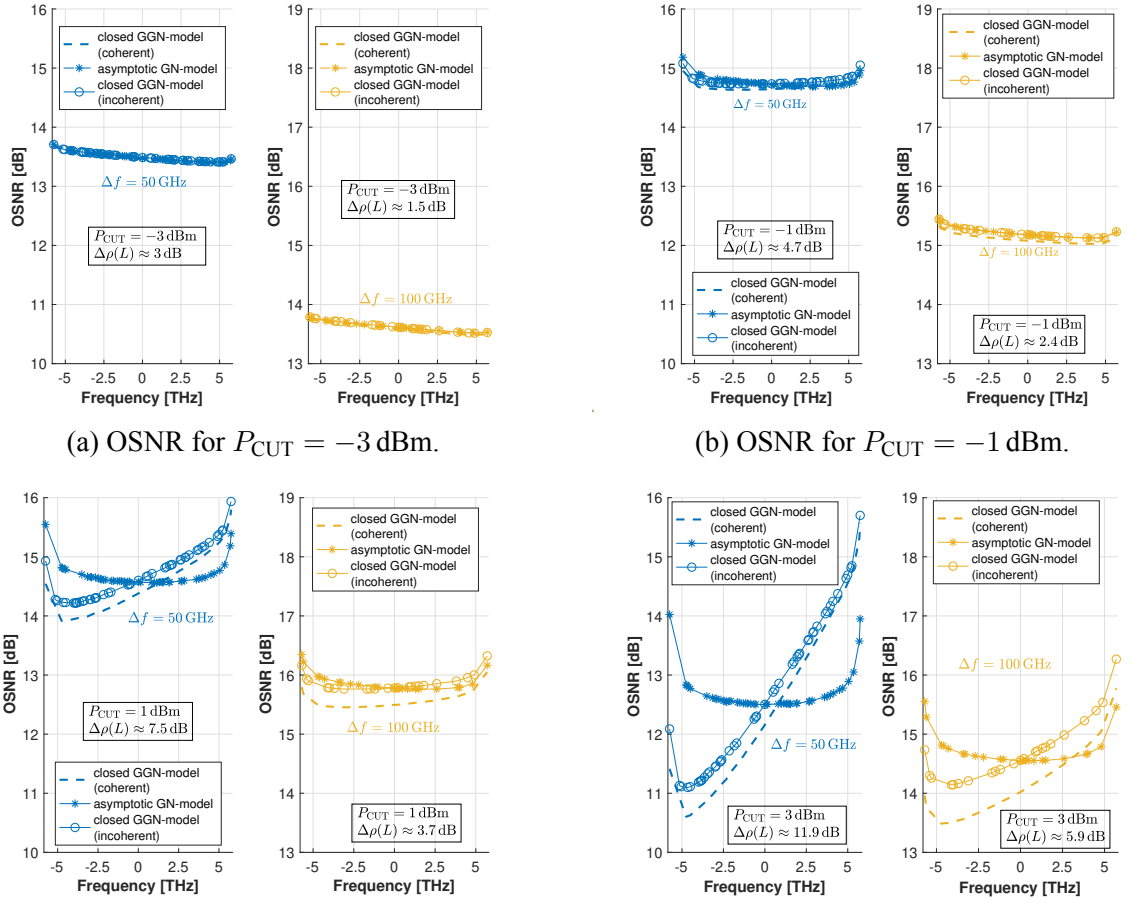

(a) OSNR for $P_{\text{CUT}} = -3\,\text{dBm}$.

(b) OSNR for $P_{\text{CUT}} = -1\,\text{dBm}$.

(c) OSNR for $P_{\text{CUT}} = 1\,\text{dBm}$.

(d) OSNR for $P_{\text{CUT}} = 3\,\text{dBm}$.

Figure 4.20. OSNR as a function of CUTs frequencies, for $\epsilon_{\text{network}} = 95\%$ and several P_{CUT}. The channel spacings $\Delta f = 50\,\text{GHz}$ and $\Delta f = 100\,\text{GHz}$ are considered.

In figure 4.20, the OSNR is depicted as a function of the CUTs frequencies, for (a) $P_{\text{CUT}} = -3\,\text{dBm}$, (b) $P_{\text{CUT}} = -1\,\text{dBm}$, (c) $P_{\text{CUT}} = 1\,\text{dBm}$ and (d) $P_{\text{CUT}} = 3\,\text{dBm}$. The WDM signal bandwidth fills the entire C+L band occupancy and the network utilization is about 95%. The lightpath considered is the one represented in figure 4.15 (a). The channels under test are chosen in the same way as in figure 4.19.

In figures 4.20 (a) and (b), since there is no considerable power transfer between the outer channels for $P_{\text{CUT}} < 0$ dBm, the maximum variation between the asymptotic GN-model and the coherent GGN-model is below about 0.3 dB for both channel spacings and the OSNR increases with the higher signal power. In figures 4.20 (c) and (d), the considered CUTs powers surpass the optimal power of 0 dBm and due to SRS, a tilt in the OSNR can be observed in the GGN-model results. For $P_{\text{CUT}} = 1$ dBm, the maximum deviation between the GGN models and the asymptotic GN-model occurs in the lowest WDM frequencies, being about 1 dB and 0.6 dB for $\Delta f = 50$ GHz and $\Delta f = 100$ GHz, respectively. When P_{CUT} is increased from 1 dBm to 3 dBm, the maximum average $\Delta\rho(L)$ rises, respectively, from about 7.5 dB to 11.9 dB for $\Delta f = 50$ GHz and from about 3.7 dB to 5.9 dB for $\Delta f = 100$ GHz. Consequently, the maximum OSNR difference increases to about 2.6 dB and 1.6 dB compared to the coherent GGN-model and increases to about 1.9 dB and 0.8 dB compared to the incoherent GGN-model.

Lastly, it is important to analyze how the $\epsilon_{\text{network}}$ impacts the performance of the GN models when the WDM signal covers the full C+L band. Figure 4.21 depicts the OSNR as a function of the $\epsilon_{\text{network}}$, for (a) $P_{\text{CUT}} = -3$ dBm, (b) $P_{\text{CUT}} = 0$ dBm and (c) $P_{\text{CUT}} = 3$ dBm. The remaining WDM system assumptions and parameters are the same as the ones considered in figure 4.20. For convenience, it is assumed that the lowest and highest frequency channels correspond to the first and last channels of the WDM signal, respectively.

For $P_{\text{CUT}} = -3$ dBm, the OSNR estimates vary steadily with the network utilization, with the difference between the GN models being smaller than 0.1 dB, independently of $\epsilon_{\text{network}}$ and WDM channel considered. The good agreement between the models predictions is due to the fact that the maximum possible power transfer is only about 3.1 dB, which occurs when $\epsilon_{\text{network}} = 100\%$ and $\Delta f = 50$ GHz.

For $P_{\text{CUT}} = 0$ dBm, the overall power transfer increases, leading to greater differences between the OSNR estimates as the network utilization increases, as can be observed in figure 4.21 (b). First, the edge channels are analyzed. It can be concluded that the OSNR differences using the incoherent GGN-model and the asymptotic GN-model are below 0.1 dB until $\epsilon_{\text{network}} = 60\%$ for $\Delta f = 50$ GHz (where $\Delta\rho(L) \approx 3.7$ dB). The OSNR differences reach about 0.3 dB when $\epsilon_{\text{network}} = 100\%$ and $\Delta\rho(L) \approx 6.2$ dB. For $\Delta f = 100$ GHz, since the maximum power transfer achievable is only 3.1 dB, the discrepancies in the OSNR estimates between these two models never exceed 0.1 dB. For the coherent GGN-model and for $\Delta f = 50$ GHz, the OSNR deviation in the first channel relative to the asymptotic GN-model is about 0.3 dB and 0.5 dB for $\epsilon_{\text{network}} = 50\%$ and $\epsilon_{\text{network}} = 100\%$, respectively. For $\Delta f = 100$ GHz, this discrepancy is

always below about 0.3 dB. For the last channel, the OSNR estimates are very similar to the estimates of the asymptotic GN-model for all $\epsilon_{\text{network}}$ considered.

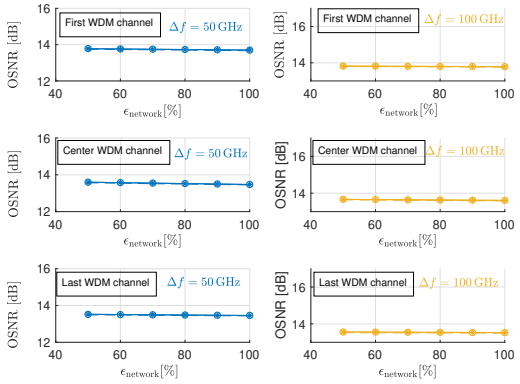

(a) OSNR for $P_{\text{CUT}} = -3$ dBm.

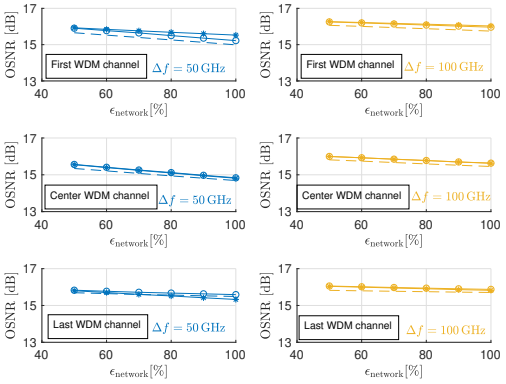

(b) OSNR for $P_{\text{CUT}} = 0$ dBm.

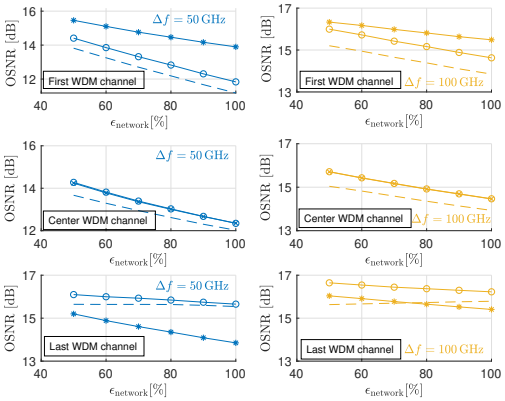

(c) OSNR for $P_{\text{CUT}} = 3$ dBm.

Figure 4.21. OSNR as a function of $\epsilon_{\text{network}}$, for the center channel and for the first and last WDM channels. The channel spacings $\Delta f = 50$ GHz and $\Delta f = 100$ GHz are considered. Lines with circles: closed GGN-model (incoherent). Dashed lines: closed GGN-model (coherent). Lines with asterisks: asymptotic GN-model.

Lastly, by analyzing figure 4.21 (c), it is inferred that the OSNR estimates from the GN models have the same behavior as the case when $P_{\text{CUT}} = 0$ dBm, but that due to the higher power transfer, the OSNR prediction deviations between the models for the edge channels is larger. For instance, for the first channel with $\Delta f = 50$ GHz, the asymptotic GN-model overestimates the OSNR at least by about 1 dB and 2 dB for $\epsilon_{\text{network}} = 50\%$ and $\epsilon_{\text{network}} = 100\%$, respectively. For the last channel and $\epsilon_{\text{network}} = 100\%$, the asymptotic GN-model underestimates the OSNR by about 1.7 dB and 0.8 dB for $\Delta f = 50$ GHz and $\Delta f = 100$ GHz, respectively.

Regarding the center channel, it can be concluded that the results from the asymptotic GN-model are very similar to the ones obtained by the GGN models for $P_{\text{CUT}} < 3\,\text{dBm}$. For $P_{\text{CUT}} = 3\,\text{dBm}$, the maximum difference achieves only about 0.7 dB.

4.6. Conclusion

In this chapter, the GGN-model has been studied and the impact of varying several system parameters in an optical network C+L transmission scenario on the estimation of the normalized NLI power and OSNR has been assessed.

The GGN-model in integral and closed forms, as well as the GN-model in hyperbolic coordinates, have been successfully implemented for a point-to-point transmission scenario. A formula in hyperbolic coordinates for the GGN-model is derived in this chapter and it was concluded that using it is much less time-consuming than using the GGN-model in cartesian coordinates. For example, to obtain the NLI PSD for a 1 THz bandwidth WDM signal, the computation time has been drastically reduced from several hours to just about 7 seconds using the GGN-model in hyperbolic coordinates. It has been found that this decrease in the computation time is due to three factors: lower frequency resolution, smaller number of ζ samples and the possibility of stopping the numerical integration before integrating the full range of the integration domain. Additionally, using the GGN-model, it was concluded that the SRS leads to a significant power transfer from higher to lower frequency channels and causes a tilt in the NLI variation, with the lower frequency channels being the most impacted.

The optical network simulator used in this work with the closed-form GGN-model was implemented and its high accuracy was confirmed by comparison with other results in the literature. Using the closed-form GGN-model, it has been shown that as the network utilization increases, the power transfer between outer channels grows, thus increasing the NLI magnitude and the tilt of its variation across the WDM signal. For example, for a 10 THz bandwidth WDM signal and from $\epsilon_{\text{network}} = 20\%$ to $\epsilon_{\text{network}} = 100\%$, the power transfer increases about 5.3 dB and 17 dB for, respectively, $P_{\text{CUT}} = 0\,\text{dBm}$ and $P_{\text{CUT}} = 5\,\text{dBm}$. Moreover, it was discovered that 150 to 200 realizations are needed to obtain a stabilized NLI variation across the signal spectrum and that, in general, the lower frequency channels exhibit a greater oscillatory behavior, which is more pronounced as $\epsilon_{\text{network}}$ grows.

For a 10 THz WDM signal and $\epsilon_{\text{network}} = 90\%$, it was concluded that, for the optimum launch power, the maximum OSNR difference along the WDM signal spectrum is 0.7 dB. It was concluded that the OSNR decreases for higher $\epsilon_{\text{network}}$ due to the increasing NLI. For the same WDM signal configuration, it was inferred that, by varying the network utilization and

considering the optimal OSNR for each WDM signal frequency, the maximum power transfer lies between 4.4 dB and 6.4 dB. For the maximum C+L band occupancy (11.5 THz) and in an optimum OSNR scenario for the center channel, it was concluded that the maximum OSNR difference by using the asymptotic GN-model in comparison with the closed-form GGN-model is less than about 0.5 dB for all network utilizations considered. These differences occur for the lowest frequency component, when $\Delta\rho(L) \approx 6\,\text{dB}$. For $\Delta\rho(L) \approx 11.9\,\text{dB}$, the maximum difference to the coherent GGN-model increases to about 2.6 dB. Additionally, it was also concluded that the maximum difference between the models decreases as the dispersion slope increases, as the asymptotic GN-model does not include this influence in its formulation and the dispersion counteracts the NLI tilt in the opposite direction. At optimum launch power, it was found that the maximum OSNR discrepancy between the models predictions increase to about 0.7 dB for a null dispersion slope.

CHAPTER 5

Conclusions and future work

In this chapter, the main conclusions of this work are presented, as well as some proposals for future work.

5.1. Final conclusions

In this dissertation, the GN-model and several of its variants proposed over the years to estimate the non-linearity impact in coherent UT fiber optic transmission in the C and L bands have been studied.

In chapter 2, the physical interpretation of the non-linearity in UT systems was explained, as well as the assumptions that have been made to derive the GN models studied in this work and their accuracy limitations. Regarding the GN models limitations, it was concluded that the GGN-model is the only model that is suitable for C+L band transmissions. It was also concluded that the EGN-model is the only one indicated for zero-dispersion WDM systems and for channels with low symbol rates (below 25 GBaud). In contrast, the remaining GN models, i.e., GN, GGN and asymptotic models, are only suitable for WDM signals with a symbol rate above 25 GBaud and systems with a minimum total accumulated dispersion of about 1900 ps/nm.

In chapter 3, the GN-model and its variants were implemented, studied and compared for transmission systems operating exclusively in the C-band. It was verified that the coherent and incoherent GN models were correctly implemented and it was concluded that, because of the phased array-factor, the coherent GN-model demands higher frequency resolutions than the IGN-model to accurately estimate the NLI in systems with more than one span. Consequently, the IGN-model has proven to be much less time-consuming than the coherent GN-model and, according to [11], [17], also more accurate in comparison with SSFM results. By comparing the performance of GN models up to the C-band limit, it was inferred that the maximum overestimation of the asymptotic GN-model in comparison with the most accurate IGN-model is about 0.3 dB for $\Delta f = 50\,\text{GHz}$ and $\beta = 0.1$. Thus, it was concluded that the asymptotic GN-model can represent an appealing alternative for estimating the NLI in WDM systems with roll-off factors below 0.1 and for applications whose priority is fast network performance estimation rather than high accuracy requirements.

In chapter 4, the GGN-model in integral and closed forms have been studied and the performance of the several GN models has been tested in a mesh optical network scenario. It was verified by comparison with literature results that both GGN-model in hyperbolic coordinates and closed GGN-model are well implemented. Regarding the GGN-model in integral form, it was inferred that solving the numerical integration using hyperbolic coordinates is much less time-consuming than solving with cartesian coordinates, since it is possible to limit the integration range and a smaller number of ζ samples is required, as well as a lower frequency resolution. For example, to estimate the NLI PSD for a 1 THz bandwidth WDM signal, it was concluded that the computation time is reduced from several hours to only about 7 seconds using the hyperbolic GGN-model.

In a network scenario, with a random WDM signal spectrum occupancy to emulate wavelength add/drops along the signal path, it was concluded that the NLI increases with the network utilization, due to increased power transfer from the WDM signal higher frequencies to the lower frequencies due to the SRS. For a 10 THz bandwidth WDM signal and a channel launch power of 0 dBm, it was concluded that the power transfer increases about 5.3 dB from $\epsilon_{\text{network}} = 20\%$ to $\epsilon_{\text{network}} = 100\%$. Furthermore, it was also discovered that the standard deviation of the normalized NLI power reaches the maximum for lower frequency channels and higher network utilizations.

For a 10 THz bandwidth WDM signal and a network utilization of 90%, it was concluded that the maximum OSNR variation along the signal spectrum is only about 0.7 dB, for the studied C+L band system at optimum launch power. Additionally, by comparing the performances of the asymptotic and GGN models, it was found that, in optimum OSNR conditions and for the full C+L band, the maximum OSNR difference by using the asymptotic GN-model is less or equal than about 0.7 dB compared to the optimum OSNR obtained with the GGN-model, for a 6 dB power transfer. Thus, it is concluded that, at optimum launch power and for applications that do not have high accuracy requirements, the asymptotic GN-model can represent a viable alternative to estimate the NLI in C+L band transmission systems for average power transfers below about 6 dB. For higher launch powers, the power transfer due to the SRS increases, which makes the use of the asymptotic GN-model unfeasible.

5.2. Future work

In this section, the following topics are proposed for future work:

- Develop a coherent version of the asymptotic GN-model including the higher order dispersion in its formulation;

- Study of the impact of the C+L guard band on the NLI power and OSNR estimation;
- Evaluate the OSNR in a multiband network transmission scenario using the more accurate GGN-model proposed in [37] and conclude on the estimation differences to the closed-form GGN-model;
- Compare the OSNR estimation obtained in this work in a more general network scenario with SSFM and experimental results;
- Study routing and wavelength assignment algorithms that are aware of the SRS impact in C+L networks;
- Extend the GGN-model to be applicable beyond the C+L band;
- Apply the GGN-model to elastic optical networks.

References

[1] S. J. Savory, "Digital coherent optical receivers: algorithms and subsystems," *IEEE Journal on Selected Topics in Quantum Electronics*, vol. 16, no. 5, pp. 1164–1179, Sep. 2010.

[2] X. Chen, C. Antonelli, S. Chandrasekhar, G. Raybon, A. Mecozzi, M. Shtaif, and P. Winzer, "Kramers–Kronig receivers for 100-km datacenter interconnects," *Journal of Lightwave Technology*, vol. 36, no. 1, pp. 79–89, Jan. 1, 2018.

[3] N. Eiselt, J. Wei, H. Griesser, A. Dochhan, M. Eiselt, J. Elbers, J. J. V. Olmos, and I. T. Monroy, "First real-time 400G PAM-4 demonstration for inter-data center transmission over 100 km of SSMF at 1550 nm," in *2016 Optical Fiber Communications Conference and Exhibition (OFC)*, Anaheim, CA, USA, Mar. 2016, 1–3, paper W1K.5.

[4] P. J. Winzer, D. T. Neilson, and A. R. Chraplyvy, "Fiber-optic transmission and networking: the previous 20 and the next 20 years," *Optics Express*, vol. 26, no. 18, pp. 24 190–24 239, Sep. 2018.

[5] K. Roberts, M. O'Sullivan, K.-T. Wu, H. Sun, A. Awadalla, D. J. Krause, and C. Laperle, "Performance of dual-polarization QPSK for optical transport systems," *Journal of Lightwave Technology*, vol. 27, no. 16, pp. 3546–3559, Aug. 15, 2009.

[6] G. Gavioli, E. Torrengo, G. Bosco, A. Carena, V. Curri, V. Miot, P. Poggiolini, F. Forghieri, S. J. Savory, L. Molle, and R. Freund, "NRZ-PM-QPSK 16 $\times$ 100 Gb/s transmission over installed fiber with different dispersion maps," *IEEE Photonics Technology Letters*, vol. 22, no. 6, pp. 371–373, Mar. 2010.

[7] A. Carena, V. Curri, G. Bosco, P. Poggiolini, and F. Forghieri, "Modeling of the impact of nonlinear propagation effects in uncompensated optical coherent transmission links," *Journal of Lightwave Technology*, vol. 30, no. 10, pp. 1524–1539, May 15, 2012.

[8] P. Poggiolini, "The GN model of non-linear propagation in uncompensated coherent optical systems," *Journal of Lightwave Technology*, vol. 30, no. 24, pp. 3857–3879, Dec. 15, 2012.

[9] A. Carena, G. Bosco, V. Curri, Y. Jiang, P. Poggiolini, and F. Forghieri, "EGN model of non-linear fiber propagation," *Optics Express*, vol. 22, no. 13, pp. 16 335–16 362, Jun. 2014. arXiv: `arXiv:1205.2193`.

[10] P. Johannisson and E. Agrell, "Modeling of nonlinear signal distortion in fiber-optic networks," *Journal of Lightwave Technology*, vol. 32, no. 23, pp. 4544–4552, Dec. 1, 2014.

[11] P. Poggiolini and Y. Jiang, "Recent advances in the modeling of the impact of nonlinear fiber propagation effects on uncompensated coherent transmission systems," *Journal of Lightwave Technology*, vol. 35, no. 3, pp. 458–480, Feb. 1, 2017.

[12] G. Rizzelli, G. Maier, M. Quagliotti, M. Schiano, and A. Pattavina, "Assessing the scalability of next-generation wavelength switched optical networks," *Journal of Lightwave Technology*, vol. 32, no. 12, pp. 2263–2270, Jun. 15, 2014.

[13] M. Cantono, R. Schmogrow, M. Newland, V. Vusirikala, and T. Hofmeister, "Opportunities and challenges of C+L transmission systems," *Journal of Lightwave Technology*, vol. 38, no. 5, pp. 1050–1060, Mar. 1, 2020.

[14] M. Cantono, D. Pilori, A. Ferrari, C. Catanese, J. Thouras, J. L. Auge, and V. Curri, "On the interplay of nonlinear interference generation with stimulated Raman scattering for QoT Estimation," *Journal of Lightwave Technology*, vol. 36, no. 15, pp. 3131–3141, Aug. 1, 2018.

[15] D. Semrau, R. I. Killey, and P. Bayvel, "The Gaussian noise model in the presence of inter-channel stimulated Raman scattering," *Journal of Lightwave Technology*, vol. 36, no. 14, pp. 3046–3055, Jul. 15, 2018. arXiv: 1801.02460.

[16] D. Semrau, R. I. Killey, and P. Bayvel, "A closed-form approximation of the Gaussian noise model in the presence of inter-channel stimulated Raman scattering," *Journal of Lightwave Technology*, vol. 37, no. 9, pp. 1924–1936, May 1, 2019.

[17] P. Poggiolini, G. Bosco, A. Carena, V. Curri, Y. Jiang, and F. Forghieri, "The GN-model of fiber non-linear propagation and its applications," *Journal of Lightwave Technology*, vol. 32, no. 4, pp. 694–721, Feb. 15, 2014.

[18] S. J. Savory, G. Gavioli, R. I. Killey, and P. Bayvel, "Electronic compensation of chromatic dispersion using a digital coherent receiver," *Optics Express*, vol. 15, no. 5, pp. 2120–2126, Mar. 2007.

[19] M. Cantono, J. L. Auge, and V. Curri, "Modelling the impact of SRS on NLI generation in commercial equipment: an experimental investigation," in *2018 Optical Fiber Communications Conference and Exposition, OFC 2018 - Proceedings*, San Diego, CA, USA, Mar. 2018, paper M1D.2.

[20] A. Ferrari, A. Napoli, J. K. Fischer, N. Costa, A. D'Amico, J. Pedro, W. Forysiak, E. Pincemin, A. Lord, A. Stavdas, J. P. F. Gimenez, G. Roelkens, N. Calabretta, S. Abrate,

B. Sommerkorn-Krombholz, and V. Curri, "Assessment on the achievable throughput of multi-band ITU-T G.652.D fiber transmission systems," *Journal of Lightwave Technology*, vol. 38, no. 16, pp. 4279–4291, Aug. 15, 2020.

[21] P. Poggiolini, G. Bosco, A. Carena, V. Curri, Y. Jiang, and F. Forghieri, "A detailed analytical derivation of the GN model of non-linear interference in coherent optical transmission systems," *posted on arXiv, www.arxiv.org, paper identifier 1209.0394*, Sep. 2012.

[22] A. Carena, G. Bosco, V. Curri, P. Poggiolini, M. Tapia Taiba, and F. Forghieri, "Statistical characterization of PM-QPSK signals after propagation in uncompensated fiber links," *European Conference on Optical Communication, ECOC*, vol. 1-2, no. 1, pp. 7–9, Sep. 2010.

[23] R. Dar, M. Feder, A. Mecozzi, and M. Shtaif, "Properties of nonlinear noise in long, dispersion-uncompensated fiber links," *Optics Express*, vol. 21, no. 22, pp. 25 685–25 699, Nov. 2013. arXiv: 1307.7401.

[24] P. Poggiolini, G. Bosco, A. Carena, V. Curri, Y. Jiang, and F. Forghieri, "A simple and effective closed-form GN model correction formula accounting for signal non-Gaussian distribution," *Journal of Lightwave Technology*, vol. 33, no. 2, pp. 459–473, Jan. 15, 2015.

[25] J. Tang, "The channel capacity of a multispan DWDM system employing dispersive nonlinear optical fibers and an ideal coherent optical receiver," *Journal of Lightwave Technology*, vol. 20, no. 7, pp. 1095–1101, Jul. 2002.

[26] H. Louchet, A. Hodžić, and K. Petermann, "Analytical model for the performance evaluation of DWDM transmission systems," *IEEE Photonics Technology Letters*, vol. 15, no. 9, pp. 1219–1221, Sep. 2003.

[27] G. Bosco, A. Carena, R. Cigliutti, V. Curri, P. Poggiolini, and F. Forghieri, "Performance prediction for WDM PM-QPSK transmission over uncompensated links," *2011 Optical Fiber Communication Conference and Exposition and the National Fiber Optic Engineers Conference, OFC/NFOEC 2011*, pp. 17–19, Mar. 2011.

[28] F. Vacondio, O. Rival, C. Simonneau, E. Grellier, A. Bononi, L. Lorcy, J.-C. Antona, and S. Bigo, "On nonlinear distortions of highly dispersive optical coherent systems," *Optics Express*, vol. 20, no. 2, pp. 1022–1032, Jan. 2012.

[29] S. Tariq and J. C. Palais, "A computer model of non-dispersion-limited stimulated Raman scattering in optical fiber multiple-channel communications," *Journal of Lightwave Technology*, vol. 11, no. 12, pp. 1914–1924, Dec. 1993.

[30] G. P. Agrawal, "Nonlinear fiber optics," in *Nonlinear Science at the Dawn of the 21st Century*, Springer, 2000, pp. 195–211.

[31] D. Semrau, R. Killey, and P. Bayvel, "Achievable rate degradation of ultra-wideband coherent fiber communication systems due to stimulated Raman scattering," *Optics Express*, vol. 25, no. 12, pp. 13 024–13 034, Jun. 2017.

[32] D. Semrau, E. Sillekens, P. Bayvel, and R. I. Killey, "Modeling and mitigation of fiber nonlinearity in wideband optical signal transmission," *IEEE/OSA Journal of Optical Communications and Networking*, vol. 12, no. 6, pp. C68–C76, Jun. 2020.

[33] G. Saavedra, D. Semrau, M. Tan, M. A. Iqbal, D. J. Elson, L. Galdino, P. Harper, R. I. Killey, and P. Bayvel, "Inter-channel stimulated raman scattering and its impact in wideband transmission systems," in *2018 Optical Fiber Communications Conference and Exposition (OFC)*, San Diego, CA, USA, Mar. 2018, 1–3, Th1C.3.

[34] X. Chen and W. Shieh, "Closed-form expressions for nonlinear transmission performance of densely spaced coherent optical OFDM systems," *Optics Express*, vol. 18, no. 18, pp. 19 039–19 054, Aug. 2010.

[35] S. J. Savory, "Approximations for the nonlinear self-Channel interference of channels with rectangular spectra," *IEEE Photonics Technology Letters*, vol. 25, no. 10, pp. 961–964, May 2013.

[36] D. Semrau, E. Sillekens, R. I. Killey, and P. Bayvel, "A modulation format correction formula for the Gaussian noise model in the presence of inter-channel stimulated Raman scattering," *Journal of Lightwave Technology*, vol. 37, no. 19, pp. 5122–5131, Oct. 1, 2019. arXiv: 1903.02506.

[37] D. Semrau, E. Sillekens, R. I. Killey, and P. Bayvel, "The ISRS GN Model, an efficient tool in modeling ultra-wideband transmission in point-to-point and network scenarios," in *2018 European Conference on Optical Communication (ECOC)*, Rome, Italy, Sep. 2018, pp. 1–3.

[38] X. Zhou and C. Xie, *Enabling technologies for high spectral-efficiency coherent optical communication networks*. John Wiley & Sons, 2016.

[39] K. Igarashi, K. Takeshima, T. Tsuritani, H. Takahashi, S. Sumita, I. Morita, Y. Tsuchida, M. Tadakuma, K. Maeda, T. Saito, *et al.*, "110.9-Tbit/s SDM transmission over 6,370 km using a full C-band seven-core EDFA," *Optics Express*, vol. 21, no. 15, pp. 18 053–18 060, Jul. 2013.

[40] H. Zhang, H. G. Batshon, D. G. Foursa, M. Mazurczyk, J.-X. Cai, C. R. Davidson, A. Pilipetskii, G. Mohs, and N. S. Bergano, "30.58 Tb/s transmission over 7,230 km using PDM half 4D-16QAM coded modulation with 6.1 b/s/Hz spectral efficiency," in *2013 Optical Fiber Communication Conference and Exposition and the National Fiber Optic Engineers Conference (OFC/NFOEC)*, Anaheim, CA, USA, Mar. 2013, 1–3, OTu2B.3.

[41] J.-X. Cai, C. R. Davidson, A. Lucero, H. Zhang, D. G. Foursa, O. V. Sinkin, W. W. Patterson, A. N. Pilipetskii, G. Mohs, and N. S. Bergano, "20 Tbit/s transmission over 6860 km with sub-Nyquist channel spacing," *Journal of Lightwave Technology*, vol. 30, no. 4, pp. 651–657, Feb. 15, 2012.

[42] R. Pastorelli, G. Bosco, A. Carena, P. Poggiolini, V. Curri, S. Piciaccia, and F. Forghieri, "Investigation of the dependence of non-linear interference on the number of WDM channels in coherent optical networks," in *2012 38th European Conference and Exhibition on Optical Communications*, Amsterdam, Netherlands, Sep. 2012, pp. 1–3.

[43] A. Carlson and P. B.Crilly, *Communication systems*. McGraw-Hill, 2010.

[44] M. Mazurczyk, J.-X. Cai, H. G. Batshon, Y. Sun, O. V. Sinkin, M. Bolshtyansky, D. G. Foursa, and A. Pilipetskii, "50GBd 64APSK coded modulation transmission over long haul submarine distance with nonlinearity compensation and subcarrier multiplexing," in *2017 Optical Fiber Communications Conference and Exhibition (OFC)*, Los Angeles, CA, USA, Jun. 2017, 1–3, Th4D.5.

[45] D. J. Ives, A. Lord, P. Wright, and S. J. Savory, "Quantifying the impact of non-linear impairments on blocking load in elastic optical networks," in *2014 Optical Fiber Communications Conference and Exposition (OFC)*, San Francisco, CA, USA, Mar. 2014, 1–3, W2A.55.

[46] S. Gringeri, B. Basch, V. Shukla, R. Egorov, and T. J. Xia, "Flexible architectures for optical transport nodes and networks," *IEEE Communications Magazine*, vol. 48, no. 7, pp. 40–50, Jul. 2010.

[47] J. Pedro, "Designing transparent flexible-grid optical networks for maximum spectral efficiency," *IEEE/OSA Journal of Optical Communications and Networking*, vol. 9, no. 4, pp. C35–C44, Apr. 2017.

[48] I. Roberts, J. M. Kahn, J. Harley, and D. W. Boertjes, "Channel power optimization of WDM systems following Gaussian Noise nonlinearity model in presence of stimulated Raman scattering," *Journal of Lightwave Technology*, vol. 35, no. 23, pp. 5237–5249, Dec. 1, 2017.

[49] B. Li, K. J. Larsen, D. Zibar, and I. Tafur Monroy, “Reconfigurable forward error correction decoder for beyond 100 Gbps high speed optical links,” *IEEE Communications Letters*, vol. 19, no. 2, pp. 119–122, Feb. 2015.

APPENDIX A

Derivation of the GGN-model in hyperbolic coordinates

The derivation of the GGN-model in hyperbolic coordinates uses the same the change of integration variables adopted in [8] in order to obtain the GN-model equation (4.7). For $f = 0$, the following change of integration variables can be carried out [8]:

$$\begin{cases} \nu_1 = \sqrt{f_1 f_2} \\ \nu_2 = -\frac{1}{2}\ln(\frac{f_2}{f_1}) \end{cases}, \begin{cases} f_1 = \nu_1 e^{\nu_2} \\ f_2 = \nu_1 e^{-\nu_2} \end{cases} \tag{A.1}$$

where the Jacobian is $|2\nu_1|$. For the more general situation for $f \neq 0$, it turns out that the parameters $\rho(f_1, f_2, f)$ and $\chi(f_1, f_2, f)$ now depend on the product $(f_1 - f)\cdot(f_2 - f)$. Therefore, the following change of integration variables can be performed [8]:

$$\begin{cases} \theta_1 = f_1 - f \Leftrightarrow f_1 = \theta_1 + f \\ \theta_2 = f_2 - f \Leftrightarrow f_2 = \theta_2 + f \end{cases} \tag{A.2}$$

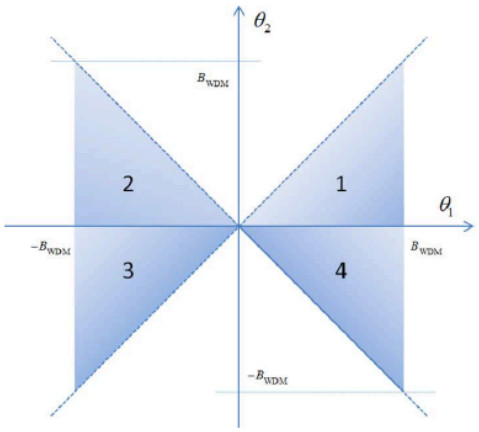

Figure A.1. Integration regions of the four quadrants used to obtain equations (4.7) and (4.10) (figure taken from [8]).

With this change of integration variables, the WDM signal PSD at f_1, f_2 and f_3 is translated [8], and the corresponding integration domain is represented in figure A.1, where the integration region in each of the four quadrants is illustrated in blue (numbered from 1 to 4). Substituting

f_1 and f_2 by the new variables, defined by (A.2), in equation (4.2), the GGN-model integrand function for each quadrant $Q(\theta_1, \theta_2, f)$ can be written as:

$$Q(\theta_1,\theta_2,f) = G_{WDM}(\theta_1+f)G_{WDM}(\theta_2+f)G_{WDM}[\theta_1+\theta_2+f] \cdot \left| \int_0^{L_s} d\zeta \frac{P_{tot}e^{-\alpha\zeta - P_{tot}C_r L_{eff}(\theta_1+\theta_2+f)}}{\int G_{WDM}(x)e^{-P_{tot}C_r L_{eff}x}\,dx} e^{-j4\pi^2\theta_1\theta_2[\beta_2+\pi\beta_3(\theta_1+\theta_2+2f)]\zeta} \right|^2 \quad \text{(A.3)}$$

The GGN-model in hyperbolic coordinates can be obtained by summing the integrand functions of each quadrant, as shown in equation (4.10). For clarity purposes, Q_1, Q_2, Q_3 and Q_4 are defined as the integrand functions of the first, second, third and fourth quadrants, respectively. To determine the integrand function in each quadrant, θ_1 and θ_2 must be replaced in equation (A.3) according to the corresponding quadrant. As the hyperbolic coordinates are always positive, a minus sign must be inserted for negative values of θ_1 and θ_2 accordingly to the quadrant considered. Thus, for each quadrant, θ_1 and θ_2 are given by:

$$\begin{aligned}
Q_1 &\Rightarrow \begin{cases} \theta_1 = \nu_1 e^{\nu_2} \\ \theta_2 = \nu_1 e^{-\nu_2} \\ \theta_1+\theta_2 = 2\nu_1\cosh(\nu_2) \end{cases} \qquad
Q_2 \Rightarrow \begin{cases} \theta_1 = -\nu_1 e^{\nu_2} \\ \theta_2 = \nu_1 e^{-\nu_2} \\ \theta_1+\theta_2 = -2\nu_1\sinh(\nu_2) \end{cases} \\
Q_3 &\Rightarrow \begin{cases} \theta_1 = -\nu_1 e^{\nu_2} \\ \theta_2 = -\nu_1 e^{-\nu_2} \\ \theta_1+\theta_2 = -2\nu_1\cosh(\nu_2) \end{cases} \qquad
Q_4 \Rightarrow \begin{cases} \theta_1 = \nu_1 e^{\nu_2} \\ \theta_2 = -\nu_1 e^{-\nu_2} \\ \theta_1+\theta_2 = 2\nu_1\sinh(\nu_2) \end{cases}
\end{aligned} \quad \text{(A.4)}$$

By substituting θ_1 and θ_2 given by equation (A.4) in equation (A.3), Q_1, Q_2, Q_3 and Q_4 are, respectively, given by:

$$Q_1(\nu_1,\nu_2,f) = G_{WDM}(\nu_1 e^{\nu_2}+f)G_{WDM}(\nu_1 e^{-\nu_2}+f)G_{WDM}[2\nu_1\cosh(\nu_2)+f] \cdot \left| \int_0^{L_s} d\zeta \frac{P_{tot}e^{-\alpha\zeta - P_{tot}C_r L_{eff}[2\nu_1\cosh(\nu_2)+f]}}{\int G_{WDM}(x)e^{-P_{tot}C_r L_{eff}x}\,dx} e^{-j4\pi^2\nu_1^2[\beta_2+\pi\beta_3(2\nu_1\cosh(\nu_2)+2f)]\zeta} \right|^2 \quad \text{(A.5)}$$

$$Q_2(\nu_1,\nu_2,f) = G_{WDM}(-\nu_1 e^{\nu_2}+f)G_{WDM}(\nu_1 e^{-\nu_2}+f)G_{WDM}[-2\nu_1\sinh(\nu_2)+f] \cdot \left| \int_0^{L_s} d\zeta \frac{P_{tot} e^{-\alpha\zeta - P_{tot}C_r L_{eff}[-2\nu_1\sinh(\nu_2)+f]}}{\int G_{WDM}(x) e^{-P_{tot}C_r L_{eff}x}\, dx} e^{j4\pi^2\nu_1^2[\beta_2+\pi\beta_3(-2\nu_1\sinh(\nu_2)+2f)]\zeta} \right|^2 \quad \text{(A.6)}$$

$$Q_3(\nu_1,\nu_2,f) = G_{WDM}(-\nu_1 e^{\nu_2}+f)G_{WDM}(-\nu_1 e^{-\nu_2}+f)G_{WDM}[-2\nu_1\cosh(\nu_2)+f] \cdot \left| \int_0^{L_s} d\zeta \frac{P_{tot} e^{-\alpha\zeta - P_{tot}C_r L_{eff}[-2\nu_1\cosh(\nu_2)+f]}}{\int G_{WDM}(x) e^{-P_{tot}C_r L_{eff}x}\, dx} e^{-j4\pi^2\nu_1^2[\beta_2+\pi\beta_3(-2\nu_1\cosh(\nu_2)+2f)]\zeta} \right|^2 \quad \text{(A.7)}$$

$$Q_4(\nu_1,\nu_2,f) = G_{WDM}(\nu_1 e^{\nu_2}+f)G_{WDM}(-\nu_1 e^{-\nu_2}+f)G_{WDM}[2\nu_1\sinh(\nu_2)+f] \cdot \left| \int_0^{L_s} d\zeta \frac{P_{tot} e^{-\alpha\zeta - P_{tot}C_r L_{eff}[2\nu_1\sinh(\nu_2)+f]}}{\int G_{WDM}(x) e^{-P_{tot}C_r L_{eff}x}\, dx} e^{j4\pi^2\nu_1^2[\beta_2+\pi\beta_3(2\nu_1\sinh(\nu_2)+2f)]\zeta} \right|^2 \quad \text{(A.8)}$$

Finally, summing the integrand function of each quadrant yields equation (4.10) as the reference formula for the GGN-model in hyperbolic coordinates.

As can be seen, in contrast to the GN-model, the change of integration variables in the GGN-model does not allow to remove the FWM efficiency parameter from the inner integral, which now takes into account the signal power profile of the frequencies of the WDM signal. For speeding up the numerical integration, the integration range can be reduced without much loss of accuracy, as shown in figure (4.6).

APPENDIX B

Article submission

Journal of Lightwave Technology

Performance Analysis of Multiband Networks using the Generalized Gaussian Noise Model

Journal:	*Journal of Lightwave Technology*
Manuscript ID	JLT-29386-2021
Manuscript Type:	Multi-Band Optical Networks 2022
Date Submitted by the Author:	30-Nov-2021
Complete List of Authors:	Venda, Pedro; ISCTE-Instituto Universitário de Lisboa, Department of Information Science and Technology Rebola, João; ISCTE-Instituto Universitario de Lisboa, Department of Information Science and Technology Cancela, Luís; ISCTE-Instituto Universitario de Lisboa, Department of Information Science and Technology
Key Words:	Gaussian noise, multiband transmission, nonlinear interference, optical networks, stimulated Raman scattering
Category:	Systems, subsystems and networks for fiber optics communications

Performance Analysis of Multiband Networks using the Generalized Gaussian Noise Model

Pedro Venda, João Rebola, and Luís Cancela

***Abstract*—In a network scenario, wavelength division-multiplexing (WDM) channels are added and dropped, leading to dynamic traffic variations in the fiber spans. In this work, the impact of these dynamic traffic variations on the predictions of nonlinear interference (NLI) and optical signal-to-noise ratio (OSNR) when varying several parameters of a C+L band mesh optical network is examined using the recently proposed generalized Gaussian noise (GGN) model. For the optimum channel launch power and increasing the network traffic variation, the power transfer between the outer channels can increase up to 5.1 dB due to stimulated Raman scattering (SRS). We show that, due to the dynamic traffic behavior, the normalized NLI power can oscillate up to 2 dB in the highest frequency channels due to NLI variations when the tested channels have unequal spacing along the spectrum. A comparison of the GGN model predictions with the Gaussian noise (GN) model that does not take into account the SRS is also performed. In all results obtained, the maximum difference between the OSNR predictions of GN (without SRS) and GGN models closed forms approximations is below 0.7 dB at optimum OSNR and maximum C+L band occupancy. For channel launch powers higher than the optimum, the OSNR differences increase up to 3 dB.**

***Index Terms*—Gaussian noise, multiband transmission, nonlinear interference, optical networks, stimulated Raman scattering.**

I. Introduction

THE Gaussian-noise (GN) model is an efficient and widely adopted tool to estimate the nonlinear interference (NLI) due to Kerr nonlinearity, simplifying current wavelength-division multiplexing (WDM) systems design and analysis [1], [2]. Recently, the generalized Gaussian-noise (GGN) model has been proposed for assessing the performance of multiband C+L transmission in WDM optical systems, where the interaction between NLI and stimulated Raman scattering (SRS) must be accurately characterized [3]–[5].

For C-band transmission, various GN-model closed-form approximations have been proposed over the years [1], [6]–[10]. Recently, GGN-model closed formulas have been derived for transmission systems operating beyond the C-band [5], [11]. For optical networking, both GN and GGN models closed forms allow fast and reliable analysis of the network physical layer impairments, enabling the development and implementation of more rigorous real time network optimization tools [1], [5], [12].

In reconfigurable optical add/drop multiplexer (ROADM) based networks, the WDM channels can be added, dropped or expressed [13], leading to dynamic traffic variations in the fiber spans. Thus, the number of WDM channels transmitted in a given span of a given lightpath varies constantly, meaning that the WDM signal bandwidth does not always fully covers the span maximum capacity, and consequently, the full network capacity.

Several works have studied the NLI interaction with SRS in multiband optical networks. The provisioning and the maximum achievable throughput of multiband transmission using the GGN-model to estimate network performance were addressed in [14], [15]. Routing and spectrum assignment algorithms aware of the SRS impact in multiband networks have been investigated in [16]–[19]. Network performance studies using the GGN-model have been presented in [20], [21]. In [20], the capacity gain of reducing the link margin is studied in a dynamic scenario considering the C+L band and a blocking probability of 10%, which can be considered too high for network normal operation [14], [22], whereas in [21], a comparison between a worst-case with full C+L band occupancy and a dynamic traffic case characterized by the same 10% blocking probability is performed. In [5], a preliminary study of the effect of the dynamic traffic variations on NLI predictions using a closed-form GGN-model was performed for validation purposes, without assessing its impact on the optical signal-to-noise (OSNR).

In this work, a finer analysis, than the ones performed in previously published works, of several WDM system parameters, such as dynamic traffic variations, number of channels under test, launch power, channel spacing, C+L band occupancy and channels distribution along the WDM spectrum, is carried out in order to assess their impact on SRS, NLI power and OSNR, using the closed-form GGN-model introduced in [5]. Additionally, the performance of this model is also compared with the closed-form GN-model proposed in [9] valid only for C-band network transmission, which to the best of our knowledge has not been done yet.

This paper is organized as follows. In section II, the main definitions and assumptions of the optical network simulator are presented and explained. In section III, the impact of the network utilization on NLI and OSNR estimation is quantified. Then, the comparison between the two closed-form GN models regarding the network performance estimation is performed. Section IV presents the conclusions.

II. Network Simulator

In this section, the network simulator definitions and assumptions considered in this work are presented and explained.

The two lightpaths studied in this work, taken from the British Telecommunications network topology [5], [23], are

J. Rebola and L. Cancela are with Instituto de Telecomunicações, 1049-001, Lisboa, Portugal, and all authors are with Iscte - Instituto Universitário de Lisboa, 1649-026, Lisboa, Portugal (corresponding author: pdsva@iscte-iul.pt).

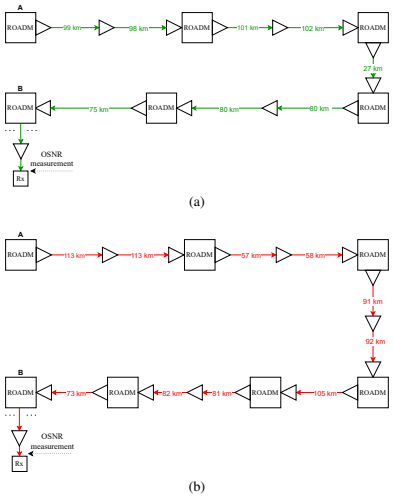

Fig. 1. Two lightpaths examples taken from the British Telecommunications topology United Kingdom core network [5], [23]. Throughout this work, the lightpaths in (a) and (b) are referred to as green and red lightpaths, respectively.

illustrated in Fig. 1. The ROADMs architecture considered is the route-and-select with maximum losses of 18 dB [24]. The filtering effects and crosstalk due to ROADM components imperfections [25] are not taken into account in our work. The post-amplifiers are designed to perfectly compensate the ROADM losses. The inline and pre-amplifiers compensate perfectly the previous fiber losses. All optical amplifiers considered in the lightpaths are erbium doped fiber amplifiers (EDFAs) with dynamic gain equalization. Thus, the EDFAs also compensate the power transfer in each span due to the SRS [26].

For the analysis of the lightpaths of Fig. 1, the WDM channels are classified in two categories: channels under test (CUTs) and add/drop channels. The CUTs correspond to the WDM channels that are transmitted/expressed along the complete lightpath, i.e., from the first node to the last node without any add/drop occurring in those wavelengths. The add/drop channels are the wavelengths that can be added or dropped in any ROADM of the considered lightpath.

We introduce the two following definitions: *network utilization* and *C+L band occupancy*. For a given span of a lightpath, the ratio between the number of channels transmitted in the j-th span and the total number of channels is defined as network utilization, which is denoted as $\epsilon_{\text{span},j}$. For the entire lightpath, the network utilization $\epsilon_{\text{network}}$ is defined as the average of the network utilizations of all spans, written as

$$\epsilon_{\text{network}} = \frac{1}{N_s}\sum_{j=1}^{N_s}\epsilon_{\text{span},j} = \frac{1}{N_s}\sum_{j=1}^{N_s}\frac{N_{ch,j}}{N_{ch}} \tag{1}$$

where $N_{ch,j}$ is the number of channels transmitted in the j-th span, N_s is the number of spans in the lightpath and N_{ch} is the total number of WDM channels considered. The C+L band occupancy $\epsilon_{\text{occupancy}}$ is defined as

$$\epsilon_{\text{occupancy}} = \frac{\Delta f N_{ch}}{B_{\text{C+L-band}}} \tag{2}$$

where $B_{\text{C+L-band}}$ is the total C+L optical transmission bandwidth, assumed as 11.5 THz [15], corresponding to 100% C+L band occupancy, and Δf is the channel spacing.

In each ROADM, the add/drop channels are added or dropped randomly considering a uniform distribution. The number of add/drop channels depends on the required $\epsilon_{\text{network}}$. The launch power of the added channels has a random offset of $\pm 1\,\text{dB}$ in relation to the launch power of the CUTs. For a more realistic approach, the added channels always maintain the same power until they are dropped, i.e., for a given lightpath, the power of a channel only changes if it is added to the optical network more than one time. This last assumption differs from the optical transmission scenario considered in [5], where the add/drop channels that have not been dropped may not maintain the power they had in the previous span. The launch powers of the CUTs are maintained along the complete lightpath.

All NLI contributions along an optical link composed by several fiber spans sum coherently or incoherently along the signal propagation until the receiver [6]. By changing the coherence factor, that represents how the NLI accumulates along the link, it is possible to calculate the normalized NLI power assuming that the self-channel interference contribution accumulates coherently or incoherently using the GGN-model formula proposed in [5]. If omitted, the GGN-model results presented in this work consider a coherent accumulation of the self-channel interference contribution, which is the most rigorous assumption [5].

The network simulator used in this work has been successfully validated according to the results shown in Fig. 8 of [5].

III. Results and Discussion

In this section, firstly, the aim is to analyze how several network parameters, with a special emphasis on the network utilization $\epsilon_{\text{network}}$, impact the normalized NLI power η_{NLI} and OSNR estimation using the GGN-model. Then, the GGN-model suitable for C+L band and the GN-model suitable for the C-band only are compared in what concerns the OSNR prediction.

A. Impact of Network Utilization, Number of Channels under Test and their spectrum distribution on NLI Prediction

One of the consequences of the dynamic variations of the add/drop channels in network spans is the oscillatory behavior in the NLI prediction, each time a given lightpath has a given network utilization [5]. In order to obtain stabilized NLI predictions over the entire WDM spectrum, 200 simulations are performed. By simulation, we mean one calculation of the normalized NLI power η_{NLI} [5, Eq. (5)] with a given network

TABLE I
SYSTEM PARAMETERS FOR SECTION III-A

System parameters	
Number of channels (N_{ch})	251
Channel spacing Δf [GHz]	40
Symbol rate (R_s) [GBaud])	40
Channel bandwidth (B_m [GHz])	40
Roll-off (β)	0.01
Loss coefficient (α) [dB/km]	0.2
Dispersion (β_2) [ps/nm/km]	17
Dispersion slope (S_r) [ps/nm^2/km]	0.067
NLI coefficient (γ) [W^{-1}.km^{-1}]	1.2
Raman gain slope (C_r) [W^{-1}km^{-1}THz^{-1}]	0.028

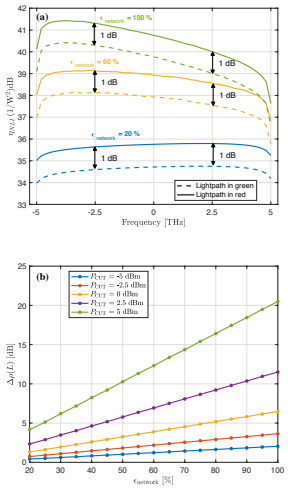

Fig. 2. In (a), the variation of the average η_{NLI} with the signal frequency is depicted, for $P_{CUT} = 0$ dBm and network utilizations of 20%, 60% and 100%. In (b), the power transfer $\Delta\rho(L)$ is represented as function of the network utilization, for the red lightpath. The number of CUTs is 20% of the number of WDM channels and the C+L band occupancy is 87%.

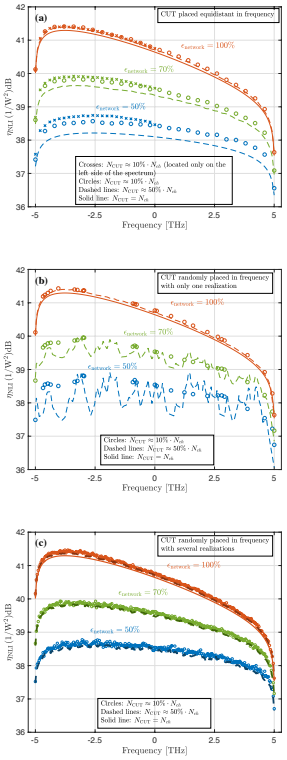

Fig. 3. Average η_{NLI} of the CUTs as a function of frequency, for $\epsilon_{\text{occupancy}} = 87\%$, several number of channels under test and network utilizations. In (a), the CUTs are placed equidistant in frequency. In (b), the CUTs are randomly positioned along the WDM spectrum only once for each network utilization. In (c), the selection of the CUTs is performed randomly along the 200 simulations. The red lightpath is considered.

utilization. Table I shows the system parameters considered for this study.

In Fig. 2(a), the CUTs average normalized NLI power η_{NLI} is represented as a function of WDM channels frequency, for the network utilizations: 20%, 60% and 100%. In Fig. 2(b) , the power transfer between the outer channels $\Delta\rho(L)$, as defined in [3], is depicted as a function of the network utilization, for several CUTs launch powers. The power transfer $\Delta\rho(L)$ is obtained by averaging the power transfers of all spans of the lightpaths. The number of CUTs considered, $N_{CUT} = 51$, is approximately 20% of the total number of WDM channels.

The average η_{NLI} exhibits a stable behavior after 200 simulations for the three network utilizations considered, as can be seen in Fig. 2(a). As the network utilization increases, the number of transmitted WDM channels grows, thus increasing the NLI magnitude and the tilt of its variation across the WDM signal. Due to the additional spans, the red lightpath is more impacted by the NLI than the green lightpath, with a constant 1 dB difference for the entire signal bandwidth.

In Fig. 2(b), the η_{NLI} increase with the network utilization is explained through the higher power transfer $\Delta\rho(L)$ between outer channels as $\epsilon_{\text{network}}$ grows. This figure also shows that $\Delta\rho(L)$ varies more sharply as the CUTs launch power P_{CUT} increases due to the highest impact of SRS. For $P_{\text{CUT}} = 5$ dBm, there is a power transfer increase of about 16.4 dB from $\epsilon_{\text{network}} = 20\%$ to $\epsilon_{\text{network}} = 100\%$, whereas for $P_{\text{CUT}} = 0$ dBm, the power transfer increases only about

5.1 dB.

Fig. 3 shows the normalized NLI power η_{NLI} as a function of the WDM signal frequency, for $N_{CUT} = 10\%N_{ch}$, $N_{CUT} = 50\%N_{ch}$ and $N_{CUT} = 100\%N_{ch}$ and for network utilizations of 50%, 70% and 100%, for the red lightpath. The average value of η_{NLI} is obtained after 200 simulations of dynamic traffic. As in the previous study, in Fig. 3(a), the CUTs are placed equidistant in frequency over the entire WDM signal bandwidth. The crosses represent the results when there are 10% of the CUTs located only on the left side of the spectrum. In Fig. 3(b), only one specific random positioning of the CUTs is shown, corresponding to an unequal spacing of the CUTs. In Fig. 3(c), for each network utilization, the CUTs are randomly chosen, being different from simulation to simulation. The launch power of the CUTs is 0 dBm.

Fig. 3(a) shows that as the number of CUTs is reduced, there is an increase of η_{NLI} across the entire WDM signal bandwidth and this increase is more pronounced for low network utilizations. For $\epsilon_{\text{network}} = 50\%$, the normalized NLI power difference is about 0.3 dB between the cases of $N_{\text{CUT}} = 10\%N_{ch}$ and $50\%N_{ch}$. For $\epsilon_{\text{network}} = 70\%$ and 100%, this difference is below 0.2 dB and is negligible for $N_{\text{CUT}} = N_{ch}$. The NLI is higher when the 10% of CUTs are only on the left side of the spectrum, due to the enhanced interference between channels (called as cross-channel interference), as the CUTs are closer in frequency.

In Fig 3(b), with an unequal CUTs spacing (channels randomly positioned along the spectrum), the normalized NLI power shows a considerable fluctuating behavior for $\epsilon_{\text{network}} < 100\%$. The highest η_{NLI} oscillation behavior occurs when $N_{\text{CUT}} = 50\% \cdot N_{ch}$ and $\epsilon_{\text{network}} = 50\%$, reaching maximum deviations of about 2 dB in the highest frequency channels. Very negligible oscillations occur when $\epsilon_{\text{network}} = 100\%$, independently of the number of CUTs considered. For $\epsilon_{\text{network}} = 100\%$, $N_{\text{CUT}} = N_{ch}$, there are no add/drop channels and it is insignificant how the CUTs are spaced in frequency.

Fig. 3(c) shows that, by generating the CUTs randomly along the signal spectrum in each simulation, there are more CUTs spread over the entire WDM spectrum, leading to a more stable η_{NLI}. For each network utilization, the influence of the number of CUTs on the η_{NLI} is very small, when compared to Figs. 3(a) and 3(b).

B. Network utilization impact on OSNR

In the following, the impact of the network utilization on the OSNR estimation using the GGN-model is evaluated. Conclusions are drawn about the optimal OSNR scenario and the network conditions leading up to it. The system parameters are presented in Table II.

In Fig. 4, the OSNR is depicted as a function of the power transfer between the outer channels, for $\epsilon_{\text{occupancy}} = 87\%$, $\epsilon_{\text{network}} = 90\%$ and for the channels allocated in the frequencies: -5 THz, -2.5 THz, 0 THz, 2.5 THz and 5 THz. To increase the power transfer $\Delta\rho(L)$, the launch power of the CUTs is increased.

The OSNR starts to grow with the increase of the power transfer, reaching the maximum between $\Delta\rho(L) \approx 3.5$ dB and 6 dB, for both lightpaths. After reaching the maximum value, the OSNR decreases more smoothly for all signal frequencies, practically with a linear behavior. As the channel power increases, for lower power transfers, the OSNR increases, since the amplifiers noise is the dominant contribution to the performance degradation. When the NLI starts to have a significant contribution to the performance degradation, the OSNR variation is smoothed and reaches the maximum value. After this maximum, the NLI becomes dominant and starts to degrade the system performance, leading to the decreasing OSNR observed in Fig. 4.

For the center channel, the CUTs launch power of approximately 0 dBm leads to the power transfer that allows obtaining the maximum OSNR, for $\epsilon_{\text{network}} > 90\%$. For this optimum power, i.e., when the OSNR maximum is reached in Fig. 4, the maximum OSNR variation between the five WDM channels is only about 0.7 dB.

The OSNR as a function of the CUTs frequencies is shown in Figs. 5(a) and 5(b), for $\epsilon_{\text{occupancy}} = 87\%$ and $\epsilon_{\text{network}} = 30\%$, $\epsilon_{\text{network}} = 50\%$, $\epsilon_{\text{network}} = 70\%$ and $\epsilon_{\text{network}} = 90\%$, for the CUTs launch power, respectively, of 0 dBm and 5 dBm. In Fig. 5(a), the power transfers of the green and red

TABLE II
SYSTEM PARAMETERS FOR SECTION III-B

System parameters	
Number of channels (N_{ch})	201
Number of channels under test (N_{CUT})	41
Channel spacing Δf [GHz]	50
Symbol rate (R_s) [GBaud])	32
Channel bandwidth (B_m [GHz])	32
Roll-off (β)	0
Loss coefficient (α) [dB/km]	0.22
Dispersion (β_2) [ps/nm/km]	16.7
Dispersion slope (S_r) [ps/nm^2/km]	0.067
NLI coefficient (γ) [W^{-1}.km^{-1}]	1.3
Raman gain slope (C_r) [W^{-1}km^{-1}THz^{-1}]	0.028
Noise figure (F_n) [dB]	5

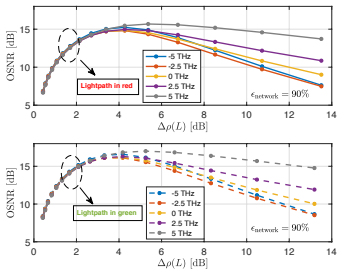

Fig. 4. OSNR as a function of the power transfer between the outer channels $\Delta\rho(L)$, for $\epsilon_{\text{occupancy}} = 87\%$, $N_{CUT} = 20\% \cdot N_{ch}$ and the red and green lightpaths.

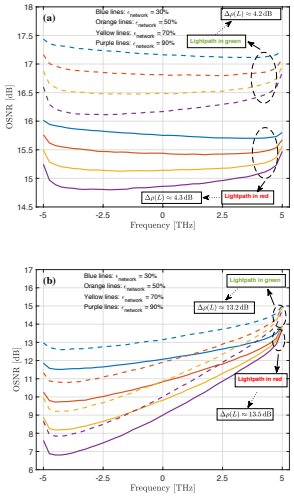

Fig. 5. OSNR as a function of the frequency, for $\epsilon_{\text{occupancy}} = 87\%$, $N_{CUT} = 20\% \cdot N_{ch}$ and network utilizations of 30%, 50%, 70% and 90%. The lightpaths used are illustrated in Fig. 1.

lightpaths achieve, respectively, about 4.2 dB and 4.3 dB and, in Fig. 5(b), about 13.2 dB and 13.5 dB. Notice that, according to Fig. 4, for $\epsilon_{\text{network}} = 90\%$, a power transfer of about 4 dB corresponds to a OSNR very close to the maximum and a power transfer of about 13 dB leads to the lowest OSNR.

In general, Fig. 5 shows that the OSNR decreases as the network utilization grows. This is a consequence of the increase of the NLI power with the network utilization, as shown in Fig. 2(a). Also as an effect of the increase of the NLI power, it can be seen that as the network utilization increases, the OSNR variation tends to tilt, with the higher frequency components of the WDM signal performing better than the lower frequency components. However, the order of magnitude of the OSNR discrepancies between the outer channels found between Figs. 5(a) and 5(b) is considerably different. Due to the high power transfer used in Fig. 5(b), the NLI tilt is much more sharper, which means that the lowest frequency channels are much more impacted by NLI. For instance, in Fig. 5(a), there is an OSNR difference of only about 0.5 dB between the outer channels for $\epsilon_{\text{network}} = 90\%$, whereas in Fig. 5(b), this difference rises to about 6 dB.

C. GN models comparison

In the following, the OSNR obtained using the GGN-model is compared with the OSNR given by the GN-model designed only for the C-band [9, Eq. (16)]. We will refer to this model as the asymptotic GN-model and to the coherent and incoherent variants of the GGN-model as the coherent GGN-model and

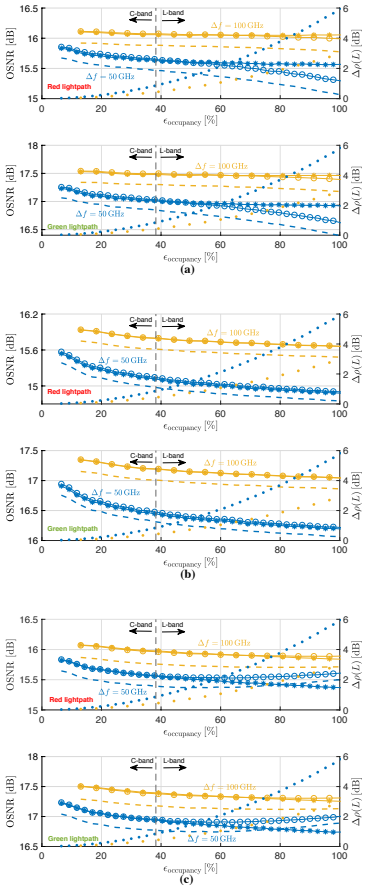

Fig. 6. The OSNR is shown as a function of the C+L band occupancy, for the center channel in (b) and the lowest and highest WDM channels in (a) and (c), respectively. The network utilization is 95% and $N_{CUT} = 20\% \cdot N_{ch}$. Circles: closed GGN-model (incoherent). Dashed lines: closed GGN-model (coherent). Asterisks: asymptotic GN-model. Points: $\Delta\rho(L)$.

incoherent GGN-model, respectively. In previous studies, a 10 THz bandwidth WDM signal has been considered, which corresponds to $\epsilon_{\text{occupancy}} \approx 87\%$. In this section, the variation of the OSNR with the C+L band occupancy is analyzed. The network utilization considered is about 95%.

The OSNR and power transfer $\Delta\rho(L)$ as a function of the C+L band occupancy are shown in Fig. 6a for the lowest frequency channel, in Fig. 6b for the center channel and in Fig. 6c for the highest frequency channel. The CUTs power

is 0 dBm. For the C+L band WDM system studied, this power leads to approximately the maximum OSNR along the several WDM channels for the network utilization considered, as shown in the previous subsection. The lowest, center and highest frequency channels are always assumed to be CUTs. Using an uniform distribution, the remaining CUTs are chosen randomly until $N_{CUT} = 20\%N_{ch}$. Two channels spacings are considered: 50 GHz (blue lines) and 100 GHz (yellow lines). The division that marks the end of the C-band and the beginning of the L-band is highlighted by dashed black vertical lines. With the exception of the number of channels and channel spacing, which are variables, the system parameters can be found in Table II.

For the center channel and the two channel spacings, the OSNR predictions using the asymptotic GN-model show a very good agreement with the ones obtained with the incoherent GGN-model for the entire C+L band. Due to higher NLI predictions, the coherent GGN-model provides lower OSNRs in the center channel, with a 0.2 dB maximum difference in relation to the other GN models.

For $\Delta f = 50\,\text{GHz}$ and $\epsilon_{\text{occupancy}} > 70\%$, the asymptotic GN-model gives higher and lower OSNR results than the incoherent GGN-model for the lowest and highest WDM frequencies, respectively. The maximum OSNR difference of 0.3 dB between these two models is reached when the C+L band is completely full and the average power transfer is approximately 6 dB. The maximum OSNR discrepancy between the asymptotic GN-model and the coherent GGN-model is only about 0.5 dB and is reached for $\Delta f = 50\,\text{GHz}$ and $\epsilon_{\text{occupancy}} = 100\%$. These higher OSNR discrepancies for $\Delta f = 50\,\text{GHz}$ are due to the higher $\Delta\rho(L)$. The OSNR differences between the GN models are approximately the same for both lightpaths considered.

It should be noted that among the GN models covered, the coherent GGN-model is the one that provides η_{NLI} results closest to the SSFM [5], and therefore, it is the more accurate model to estimate the OSNR.

In Fig. 7, the OSNR is depicted as a function of the CUTs frequencies, for (a) $P_{CUT} = -3\,\text{dBm}$, (b) $P_{CUT} = 0\,\text{dBm}$ and (c) $P_{CUT} = 3\,\text{dBm}$, for $\epsilon_{\text{occupancy}} = 100\%$, $\epsilon_{\text{network}} = 95\%$. The OSNR obtained with the GGN models considers a null dispersion slope. In contrast to the closed-form GGN-model, the asymptotic GN-model does not take into account the influence of the dispersion slope on the NLI prediction. Therefore, the aim of this study is also to analyze the impact of this parameter on the OSNR differences between the asymptotic GN-model and the GGN models. Only the red lightpath is considered. The remaining system parameters are the same as the ones considered in Fig. 6.

In Fig. 7(a), since there is no considerable SRS power transfer between the outer channels for launch powers below 0 dBm, the difference between the OSNR of the outer channels is below 0.3 dB for all the GN-models considered. For the optimum launch power of 0 dBm, Fig. 7(b), the maximum discrepancy between the asymptotic GN-model and incoherent and coherent GGN models increases to about 0.4 dB and 0.7 dB, respectively. In Fig. 7(c), the considered CUTs power surpasses the optimal power of 0 dBm, and due to SRS, a much sharper tilt in the OSNR can be observed in the GGN-model results. The maximum average power transfer rises, respectively, from about 6 dB to 11.9 dB, for the 50 GHz channel spacing, and from 3 dB to 5.9 dB for the 100 GHz spacing, in relation to the 0 dBm launch power. Consequently, the maximum OSNR difference increases to about 3 dB compared to the coherent GGN-model and increases to about 2.4 dB compared to the incoherent GGN-model.

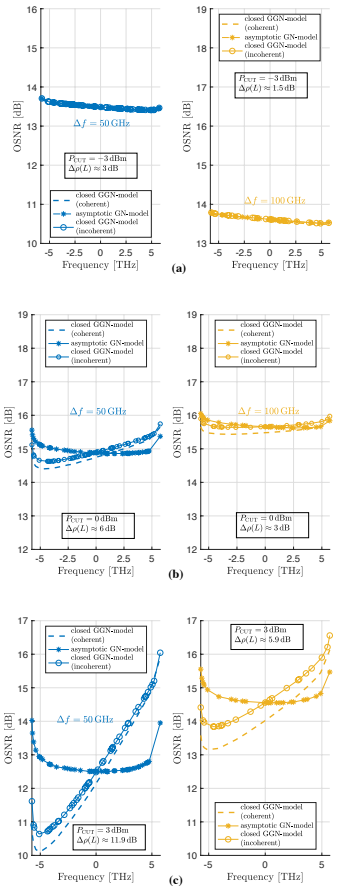

Fig. 7. OSNR as a function of CUTs frequencies, for $\epsilon_{\text{occupancy}} = 100\%$, $\epsilon_{\text{network}} = 95\%$, $N_{CUT} = 20\% \cdot N_{ch}$, $S_r = 0\,\text{ps/nm}^2\text{/km}$ and the launch powers of (a) -3 dBm, (b) 0 dBm and (c) 3 dBm. Channel spacings $\Delta f = 50\,\text{GHz}$ and $\Delta f = 100\,\text{GHz}$ are used. Circles: closed GGN-model (incoherent). Dashed lines: closed GGN-model (coherent). Asterisks: asymptotic GN-model. Points: $\Delta\rho(L)$.

As a main conclusion, the results presented in this subsection show that the asymptotic GN-model can provide reasonably accurate OSNR predictions in C+L band optical networks at optimum launch power, but can lead to differences in the OSNR of up to 3 dB if this condition is not fulfill.

IV. Conclusion

In this work, we studied the impact of the network utilization and several other network parameters on the NLI and OSNR estimation using the GGN-model. It was concluded that a variation in the network utilization from 20% to 100% leads to a power transfer increase of about 5.1 dB and 16.4 dB for, respectively, the launch powers of 0 dBm and 5 dBm. With unequal CUTs spacing along the spectrum, we show that, due to the dynamic traffic behavior, the normalized NLI power can oscillate 2 dB along the WDM channels spectrum due to NLI variations.

Additionally, comparing the performances of the asymptotic and GGN models in optimum OSNR conditions and for the full C+L band occupancy, the maximum OSNR difference using the asymptotic GN-model is only 0.7 dB compared to the optimum OSNR obtained with the GGN-model. Hence, we have shown that, at optimum launch power and for applications that do not have high accuracy requirements, the asymptotic GN-model can represent a viable alternative to estimate the NLI in C+L band transmissions systems for average power transfers below 6 dB. However, for higher power transfers, the OSNR discrepancies can increase up to 3 dB, and therefore, the use of the asymptotic GN-model is not recommended.

Acknowledgment

This work was supported under the project of Instituto de Telecomunicações UIDB/50008/2020.

References

[1] P. Poggiolini and Y. Jiang, "Recent advances in the modeling of the impact of nonlinear fiber propagation effects on uncompensated coherent transmission systems," *J. Lightw. Technol.*, vol. 35, no. 3, pp. 458–480, Feb. 2017.

[2] A. Ferrari *et al.*, "GNPy: an open source application for physical layer aware open optical networks," *J. Opt. Commun. Netw.*, vol. 12, no. 6, pp. C31–C40, Jun. 2020.

[3] D. Semrau, R. I. Killey, and P. Bayvel, "The Gaussian noise model in the presence of inter-channel stimulated Raman scattering," *J. Lightw. Technol.*, vol. 36, no. 14, pp. 3046–3055, Jul. 2018. arXiv: 1801.02460.

[4] M. Cantono, J. L. Auge, and V. Curri, "Modelling the impact of SRS on NLI generation in commercial equipment: an experimental investigation," in *Proc. Opt. Fiber Commun. Conf. Expo.*, San Diego, CA, Mar. 2018.

[5] D. Semrau, R. I. Killey, and P. Bayvel, "A closed-form approximation of the gaussian noise model in the presence of inter-channel stimulated raman scattering," *J. Lightw. Technol.*, vol. 37, no. 9, pp. 1924–1936, May 2019.

[6] P. Poggiolini, "The GN model of non-linear propagation in uncompensated coherent optical systems," *J. Lightw. Technol.*, vol. 30, no. 24, pp. 3857–3879, Dec. 2012.

[7] X. Chen and W. Shieh, "Closed-form expressions for nonlinear transmission performance of densely spaced coherent optical OFDM systems," *Opt. Express*, vol. 18, no. 18, pp. 19 039–19 054, Aug. 2010.

[8] S. J. Savory, "Approximations for the nonlinear self-Channel interference of channels with rectangular spectra," *IEEE Photon. Technol. Lett.*, vol. 25, no. 10, pp. 961–964, May 2013.

[9] P. Johannisson and E. Agrell, "Modeling of nonlinear signal distortion in fiber-optic networks," *J. Lightw. Technol.*, vol. 32, no. 23, pp. 4544–4552, Dec. 2014.

[10] P. Poggiolini, G. Bosco, A. Carena, V. Curri, Y. Jiang, and F. Forghieri, "A simple and effective closed-form GN model correction formula accounting for signal non-Gaussian distribution," *J. Lightw. Technol.*, vol. 33, no. 2, pp. 459–473, Jan. 2015.

[11] D. Semrau, R. Killey, and P. Bayvel, "Achievable rate degradation of ultra-wideband coherent fiber communication systems due to stimulated raman scattering," *Opt. Express*, vol. 25, no. 12, pp. 13 024–13 034, Jun. 2017.

[12] V. Anagnostopoulos, C. T. Politi, C. Matrakidis, and A. Stavdas, "Physical layer impairment aware wavelength routing algorithms based on analytically calculated constraints," *Opt. Commun.*, vol. 270, no. 2, pp. 247–254, Feb. 2007.

[13] S. Gringeri, B. Basch, V. Shukla, R. Egorov, and T. J. Xia, "Flexible architectures for optical transport nodes and networks," *IEEE Commun. Mag.*, vol. 48, no. 7, pp. 40–50, Jul. 2010.

[14] N. Sambo *et al.*, "Provisioning in multi-band optical networks," *J. Lightw. Technol.*, vol. 38, no. 9, pp. 2598–2605, May 2020.

[15] A. Ferrari *et al.*, "Assessment on the achievable throughput of multi-band ITU-T G.652.D fiber transmission systems," *J. Lightw. Technol.*, vol. 38, no. 16, pp. 4279–4291, Aug. 2020.

[16] V. Lopez *et al.*, "Optimized design and challenges for C&L band optical line systems," *J. Lightw. Technol.*, vol. 38, no. 5, pp. 1080–1091, Mar. 2020.

[17] S. Behera, A. Deb, G. Das, and B. Mukherjee, "Impairment aware routing, bit loading, and spectrum allocation in elastic optical networks," *J. Lightw. Technol.*, vol. 37, no. 13, pp. 3009–3020, Jul. 2019.

[18] M. Mehrabi, H. Beyranvand, and M. J. Emadi, "Multi-band elastic optical networks: Inter-channel stimulated raman scattering-aware routing, modulation level and spectrum assignment," *J. Lightw. Technol.*, Jun. 2021.

[19] M. Habibi and H. Beyranvand, "Impairment-aware manycast routing, modulation level, and spectrum assignment in elastic optical networks," *IEEE/OSA J. Opt. Commun. Netw.*, vol. 11, no. 5, pp. 179–189, May 2019.

[20] A. Mitra *et al.*, "Effect of reduced link margins on C+L band elastic optical networks," *J. Opt. Commun. Netw.*, vol. 11, no. 10, pp. C86–C93, Oct. 2019.

[21] A. Mitra *et al.*, "Effect of channel launch power on fill margin in C+L band elastic optical networks," *J. Lightw. Technol.*, vol. 38, no. 5, pp. 1032–1040, Mar. 2020.

[22] B. Correia, R. Sadeghi, E. Virgillito, A. Napoli, N. Costa, J. Pedro, and V. Curri, "Power control strategies and network performance assessment for C+ L+ S multiband optical transport," *J. Opt. Commun. Netw.*, vol. 13, no. 7, pp. 147–157, Jul. 2021.

[23] D. J. Ives, A. Lord, P. Wright, and S. J. Savory, "Quantifying the impact of non-linear impairments on blocking load in elastic optical networks," in *Proc. Opt. Fiber Commun. Conf.*, 2014, pp. 1–3.

[24] J. Pedro, "Designing transparent flexible-grid optical networks for maximum spectral efficiency [invited]," *IEEE/OSA J. Opt. Commun. Netw.*, vol. 9, no. 4, pp. C35–C44, Apr. 2017.

[25] D. Sequeira, L. Cancela, and J. Rebola, "CDC ROADM design tradeoffs due to physical layer impairments in optical networks," *Opt. Fiber Technol.*, vol. 62, p. 102 461, Mar. 2021.

[26] D. Semrau, E. Sillekens, P. Bayvel, and R. I. Killey, "Modeling and mitigation of fiber nonlinearity in wideband optical signal transmission [invited]," *IEEE/OSA J. Opt. Commun. Netw.*, vol. 12, no. 6, pp. C68–C76, Jun. 2020.